Ordered InAs/InP quantum dot arrays at telecom wavelength

Citation for published version (APA):
Sritirawisarn, N. (2010). *Ordered InAs/InP quantum dot arrays at telecom wavelength*. [Phd Thesis 1 (Research TU/e / Graduation TU/e), Applied Physics and Science Education]. Technische Universiteit Eindhoven. https://doi.org/10.6100/IR675375

DOI:
10.6100/IR675375

Document status and date:
Published: 01/01/2010

Document Version:
Publisher’s PDF, also known as Version of Record (includes final page, issue and volume numbers)

Please check the document version of this publication:

- A submitted manuscript is the version of the article upon submission and before peer-review. There can be important differences between the submitted version and the official published version of record. People interested in the research are advised to contact the author for the final version of the publication, or visit the DOI to the publisher's website.
- The final author version and the galley proof are versions of the publication after peer review.
- The final published version features the final layout of the paper including the volume, issue and page numbers.

Link to publication

General rights
Copyright and moral rights for the publications made accessible in the public portal are retained by the authors and/or other copyright owners and it is a condition of accessing publications that users recognise and abide by the legal requirements associated with these rights.

- Users may download and print one copy of any publication from the public portal for the purpose of private study or research.
- You may not further distribute the material or use it for any profit-making activity or commercial gain
- You may freely distribute the URL identifying the publication in the public portal.

If the publication is distributed under the terms of Article 25fa of the Dutch Copyright Act, indicated by the “Taverne” license above, please follow below link for the End User Agreement:

www.tue.nl/taverne

Take down policy
If you believe that this document breaches copyright please contact us at:

openaccess@tue.nl

providing details and we will investigate your claim.

Download date: 04. Oct. 2023

Ordered InAs/InP Quantum Dot Arrays at Telecom Wavelength

PROEFSCHRIFT

ter verkrijging van de graad van doctor aan de
Technische Universiteit Eindhoven, op gezag van de
rector magnificus, prof.dr.ir. C.J. van Duijn, voor een
commissie aangewezen door het College voor
Promoties in het openbaar te verdedigen
op dinsdag 15 juni 2010 om 16.00 uur

door

Nut Sritirawisarn

geboren te Bangkok, Thailand

Dit proefschrift is goedgekeurd door de promotoren:

prof.dr. P.M. Koenraad
en
Prof. W.T. Masselink PhD

Copromotor:
Dr. R. Nötzel

A catalogue record is available from the Eindhoven University of Technology Library

ISBN: 978-90-386-2260-6
NUR: 926

Sritirawisarn, Nut

Ordered InAs/InP Quantum Dot Arrays at Telecom Wavelength / by
Nut Sritirawisarn. – Eindhoven, Technische Universiteit Eindhoven, 2010. –
Proefschrift.

Subject headings: chemical beam epitaxy growth/ III-V semiconductors/ semiconductor quantum dots/ anisotropic strain engineering/ optical properties/ photoluminescence

The work presented in this thesis was carried out in the group Photonics and Semiconductor Nanophysics, Department of Applied Physics, Eindhoven University of Technology.

This research was supported by NanoNed, a national nanotechnology program coordinated by the Dutch Ministry of Economic Affairs.

“Life is semiconductor, always has defects”

CONTENTS

CHAPTER 1

General Introduction to Quantum Dots and Related Nanostructures

ABSTRACT

In this introduction chapter I will briefly review the general aspects concerning the fundamental physics, general background and practical applications of "nanostructures" particularly quantum dots (QDs). QDs are known as "artificial atoms" because of their nanometer-scale dimensions, smaller than the electron's de Broglie wavelength leading to three-dimensional quantum confinement and, hence, discrete energy states of electrons and holes. Within the past two decades after high-quality QDs were experimentally realized they quickly entered the forefront of cutting edge research leading to exciting physics and applications for the next generation of quantum devices.

1.1 Background: Motivation and Historical Developments

The development of semiconductor technology is one of the major successes in the modern science of mankind, not only because it is one of the largest industry sectors in the world with a global sale of over 2.2 trillion dollars in 2009, but also because it has created numerous devices that have literally changed our world. The unique properties of the semiconductor materials rely on their different energy bandgaps and lattice constants, shown in Fig. 1, and the ability to tune the material compositions and emission wavelengths leading to the creation of tailored material properties and applications. For most of III-V semiconductor materials (compounds of group III and V elements in the periodic table such as GaAs, InAs, and InP), it is well known that they have a direct bandgap transition and therefore play the major role in the field of optoelectronics devices.

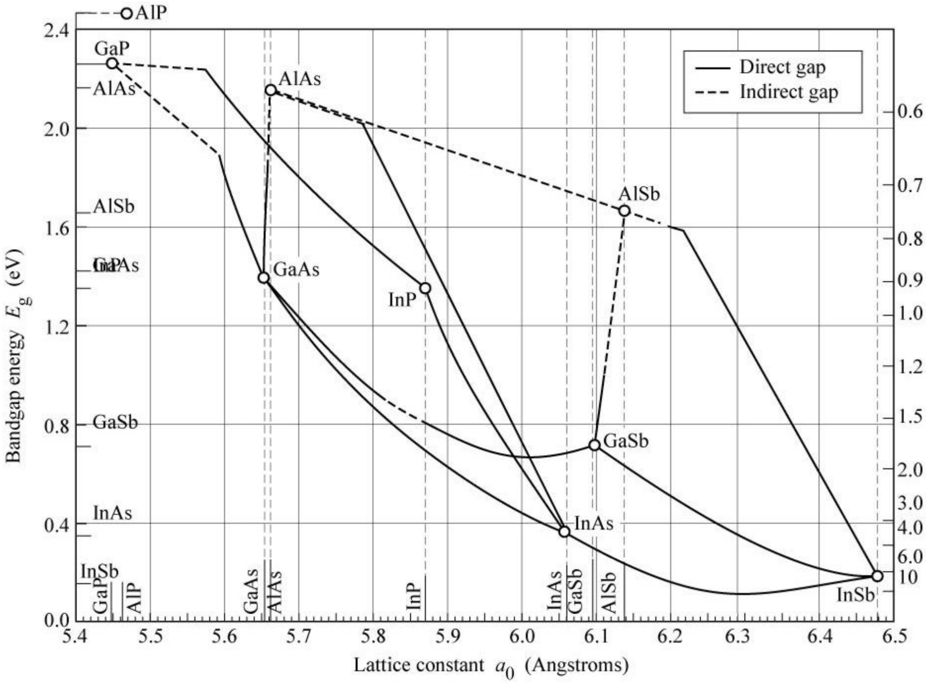

Figure 1 Bandgap energy and lattice constant of various III-V semiconductors at room temperature [1].

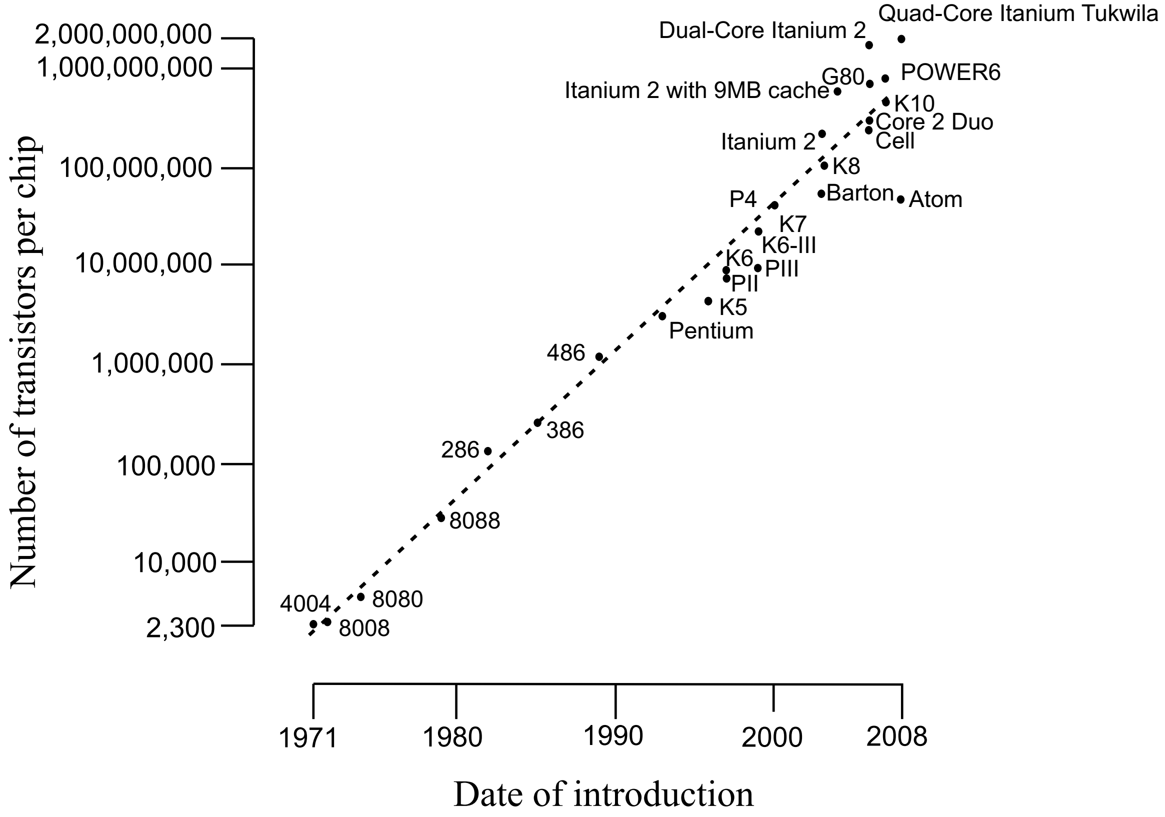

Figure 2 Transistor counts for integrated circuits plotted against their dates of introduction. The curve shows Moore's law - the doubling of transistor counts every two years [2].

For electrical devices, ever since the first metal-semiconductor contact was first discovered by Braun in 1874 [3], there was dramatical improvement in the materials scalability for integrated circuits (IC) as reflected by Moore's Law, which describes the general trend of the number of transistors per microchip which is doubled approximately every two years, shown in Fig 2. However, this trend is predicted to be restricted around 2020s due to the physical limitations of lithographic processes, thus, strong alternative efforts of downsizing of electronic devices and materials to prolong the trend has began.

In 1969, Leo Esaki (1973 Nobel Laureate) and Ray Tsu from IBM, USA, proposed research on "man-made crystals" [4,5] using a semiconductor superlattice (a semiconductor structure comprising several alternating ultra-thin layers of semiconductor materials with different properties). This invention pioneered the research field of engineering new semiconductor materials by exploiting low-dimensional structures, which later triggered a tremendous amount of experimental and fundamental investigations. However, not until the late 1970s sufficiently thin epitaxial layers were produced when the invention of advanced crystal growth techniques such as molecular-beam epitaxy (MBE), allowed the precise control of epitaxial material growth at atomic scale [6]. The emergence of semiconductor quantum wells (QWs), ultra thin two-dimensional semiconductor materials with widths of several nanometers in the 1980s, following the developments of epitaxial growth techniques, illustrated the important benefits that can be obtained through quantum confinement of carriers along one direction in a semiconductor device [7]. Several improvements of QW lasers as compared to the conventional bulk double heterostructure devices were obtained such as an order of magnitude smaller threshold current, significantly improved temperature stability, and narrower gain spectrum [8-10]. Using different materials combinations enabling emission wavelength tuning from 400 to 3000 nm, ultimately lead to commercial products. Based on this success efforts started to further shrink down the materials dimensionalities for investigations of the impact of higher dimensional quantum confinement. In the beginning, the word "multidimensional QWs" was used to describe the materials where the carriers confined in more than one dimension as in QWs. Two-dimensional QWs are materials that have two-dimensional confinement, referred to as quantum wires (QWRs), and, in particular, three-dimensional QWs where the carriers are confined in all three dimensions were later known as quantum dots (QDs). Although QWRs had generated great interests for device improvement the ultimate quantum confinement in QDs is expected to lead to most superior properties. With the size of QDs ranging from nanometers to tens of nanometers, smaller than the de Broglie wavelength of electrons (typically 20 nm in GaAs), quantum confinement takes place in all directions and the energy levels are discrete. Therefore QDs behave as "artificial atoms".

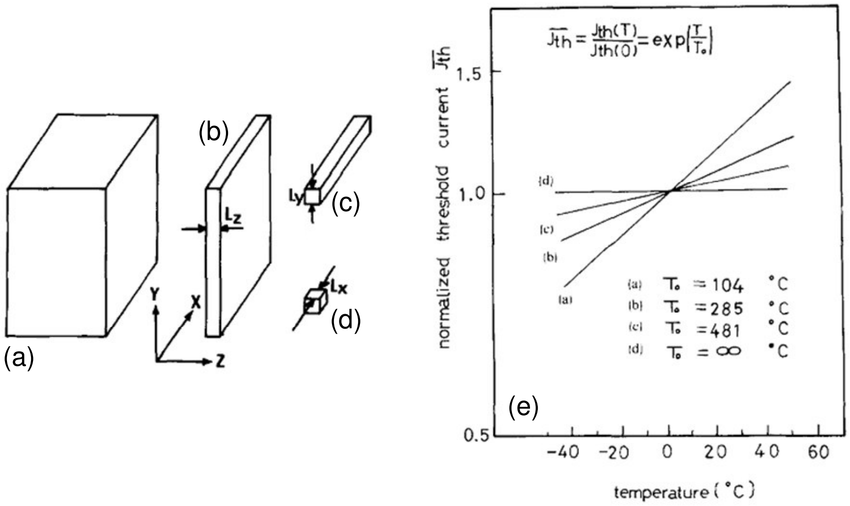

Figure 3 Left-hand side: illustration of various active layers for (a) the conventional laser, and the multidimensional quantum well lasers. (b), (c), and (d) correspond to 1D-, 2D-, and 3D-quantum well structures. Right-hand side: numerical example of threshold current J_{th} calculated for (a) the conventional laser, (b), (c), and (d) correspond to 1-D-, 2D-, and 3D-quantum well structures. Adapted from Y. Arakawa and H. Sakaki [11].

In 1982, Arakawa and Sakaki first proposed the concept of three-dimensionally confined structures for implementation in laser devices [11]. They theoretically predicted superior performance of QD laser devices over QW laser devices in terms of temperature insensitivity, shown in Fig. 3, which was later confirmed by Asada *et al.* showing the theoretical observation of higher gain and lower threshold current density of QD lasers compared to QWR and QW devices [12].

In 1985, the very first self-assembled QDs were, almost accidently, experimentally fabricated by Goldstein *et al.* in a report of three-dimensional island growth of ultra-thin InAs/GaAs strained-layer superlattices [13]. It was not until the early 1990s that the potential of this method for confining carriers in three dimensions was recognized and the last 2 decades have seen the publication of over ten thousand QD papers reflecting the numerous activities in the research field of QDs and they became one of the most important subjects in the field of low-dimensional semiconductor physics.

Today, very active research on self-assembled QDs is ongoing which concerns not only the wide-spectrum of advanced growth techniques for fabrication of nearly-perfect QDs but also the great amount of fundamental physics studies exploring the fascinating nature and properties of QDs, including the effort to implement QDs in devices for higher performances and more functionalities.

1.2 Photonics Integration for Global Telecommunication

In the modern world, data communication and transmission are of prime importance. Technology for the internet has dramatically changed the world in the past decade. Light-wave transmission technology has recently entered the “terabit era” where the need for data flows and bandwidths are enormous and rapidly increasing year by year. The majority of internet data transmission occurs in optical fiber systems which in comparison to electronic copper wires allows for very high-speed and low-loss transmission over much longer distances. Figure 4 shows high-capacity submarine optical-fiber links spanning across the world with the total accumulated end-to-end lengths spanning the globe more than 25,000 times, equal to the distance from earth to sun. Major breakthroughs in modern optical telecommunication date back to the 1970s – 1980s with the invention of double-heterostructure semiconductor laser diodes (Z. I. Alferov [14], 2000 Nobel Laureate) and the invention of optical fibers (C. K. Kao [15], 2009 Nobel Laureate) for long-distance transmission of light waves. For long-haul data transmission, minimum data attenuation is highly desired, although the erbium-doped fiber amplifier (EDFA) [16] and semiconductor optical amplifier (SOA) [17] can be utilized for data signal amplifying. In conventional optical fiber glass, small attenuation is observed near 1.3 µm and the lowest attenuation is observed at 1.55 µm, determined by fundamental physical phenomena in the purified glass, see Fig. 5. In the 1.3-µm wavelength region, the technological devices can be covered by the InAs/GaAs-based system, however, it is difficult to extend the emission wavelength to the 1.55-µm wavelength region in this material system whereas the InAs/InP-based system is more suitable. The details of application and wavelength tuning will be described later in the thesis.

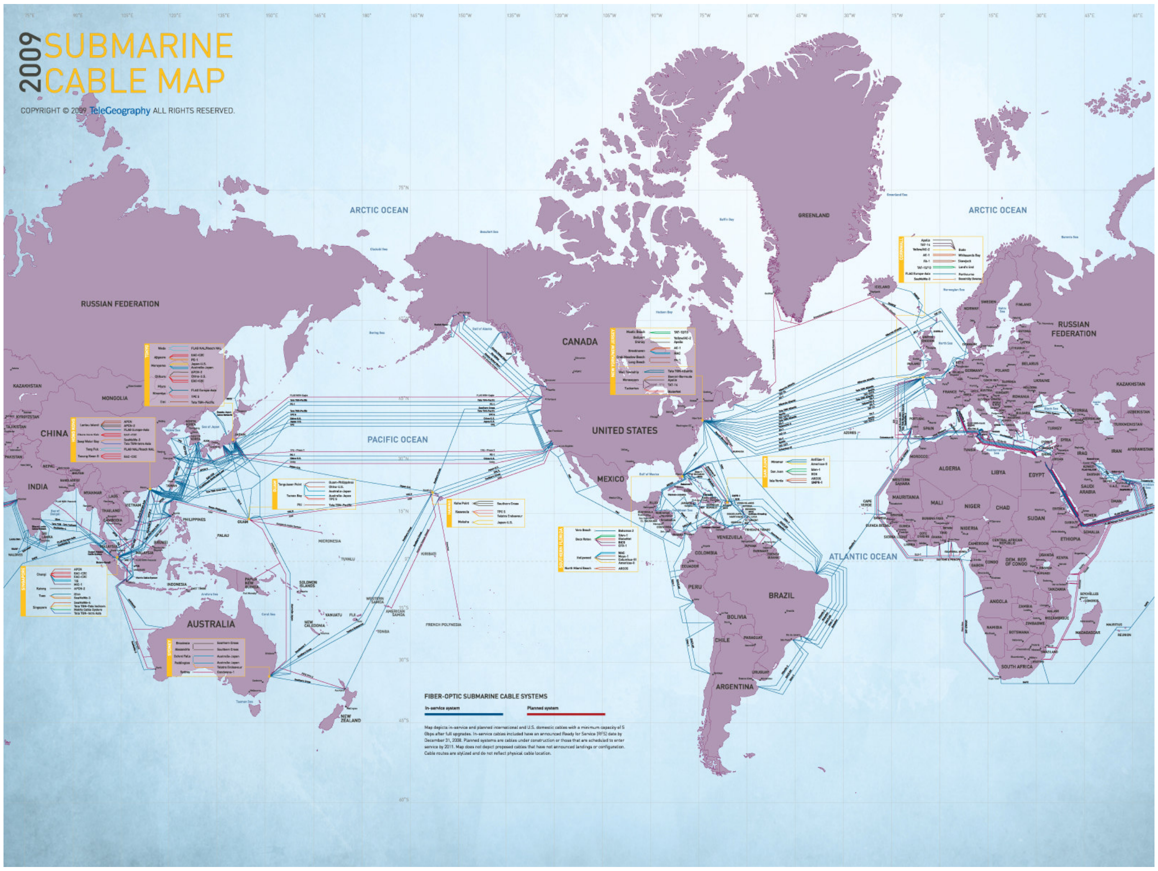

Figure 4 High-capacity submarine optical-fiber links span the globe [18].

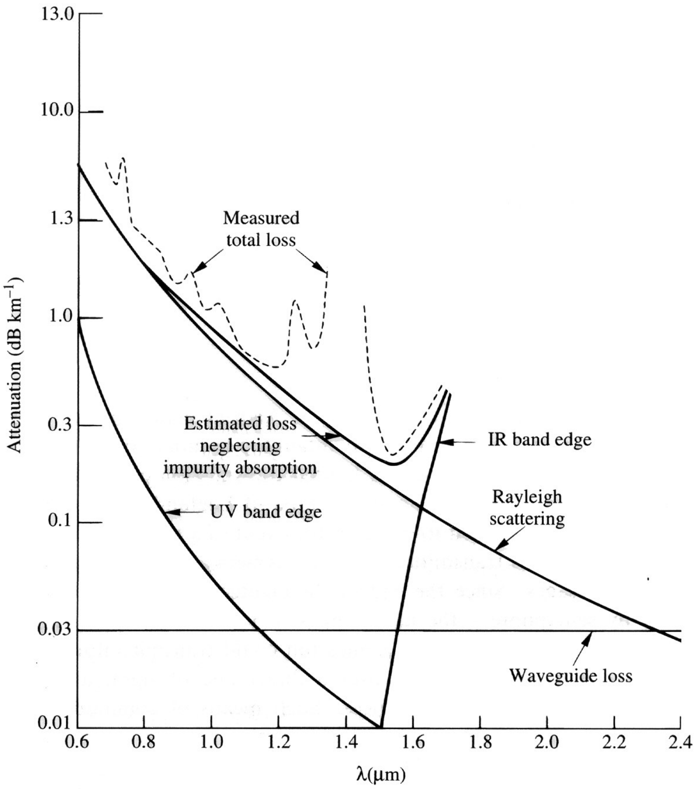

Figure 5 The variation of attenuation with wavelength of a typical modern fiber. Solid lines correspond with various loss mechanisms [19].

1.3 Density of States

The number of electronic states per unit volume and energy is referred as the density of states. In low-dimensional structures where the dimensions are smaller than the de Broglie wavelength, quantization of the energy levels takes place, which restricts the motion of electrons unlike the situation in bulk where electrons are free to move in three dimensions.

Figure 6 shows the conduction band density of states functions for systems with increasing confinement. For bulk systems, the density of states, $g(E)$, is continuous and the $g(E)$ a $E^{1/2}$ relationship is observed. For QWs where electrons are confined in one dimension, $g(E)$ is constant for each subband. For QWRs $g(E)$ is proportional to $E^{-1/2}$ and for QDs three-dimensional confinement is observed and a Dirac δ-function density of states is obtained.

The modification of the density of states due to the materials dimensionality is responsible for many of the improvements in the optical properties of QDs and devices, including higher materials and differential gain of lasers, lower threshold current densities and a smaller temperature sensitivity in their operation, as will be described in Section 1.6.

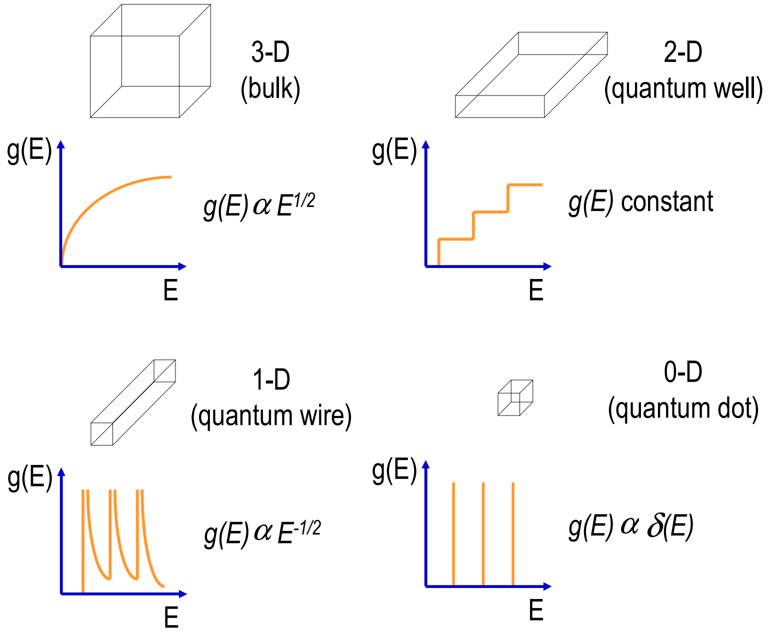

Figure 6 Density of states function *g(E)* in quantum-confined systems [20]

1.4 Epitaxial Methods: MBE, MOVPE, and CBE

The word *epitaxy* is derived from the Greek words *epi* (meaning "on") and *taxis* (meaning "arrangement"). The epitaxial layer and the substrate materials may be the same, giving rise to *homoepitaxy*, otherwise, the word *heteroepitaxy* is used when the epitaxial layer and the substrate materials are different. Mature modern epitaxial growth methods developed in the past few decades allowed for the growth of epitaxial layers with atomic layer perfection. The most commonly growth techniques are molecular-beam epitaxy (MBE) and metal-organic vapor phase epitaxy (MOVPE).

In MBE, the reactants are generated by thermal evaporation from solid, elemental sources (e.g. In, Ga, As, P) inside an ultra-high vacuum (UHV) growth chamber. The temperature of each effusion cell or crucible determines the vapor pressure of the source and thus the material flux towards the heated substrate. Since the pressure during growth is below 10^{-5} Torr, the mean free path is longer than the source inlet to substrate distance (10-40 cm). Hence, the material transport is collision-free and occurs in the form of atomic and molecular beams. This allows abrupt on/off switching by a shutter directly in front of the cell and growth of heterostructures with interfaces that are atomically sharp. Problems in MBE are due to the difficult temperature control of the effusion cells since the change in effusion cells temperature is dramatically altered the beam flux and growth rate. Moreover, the temperature profile of the group III cells change with consumption, thus the regular calibration is required.

MOVPE systems use gaseous (vapor phase) source materials, which are transported by hydrogen carrier gas. Reactor pressures range from 10 Torr (low pressure MOVPE) to 760 Torr (atmospheric pressure MOVPE). Thus, the gas flow is viscous and the chemicals reach the substrate by diffusion through a boundary layer. Decomposition of the group III metal organic compounds [e.g. Trimethylindium (TMIn), Triethylgallium (TEGa), Triethylaluminium (TEAl)] and the group V hydrides [(e.g. arsine (AsH_3), phosphine (PH_3)] occurs by partial pyrolysis in the gas phase and further dissociation on the heated substrate surface. The advantage of MOVPE growth is the flexibility of the vapor sources and the ability to grow mass products which makes this technique very suitable for the industry.

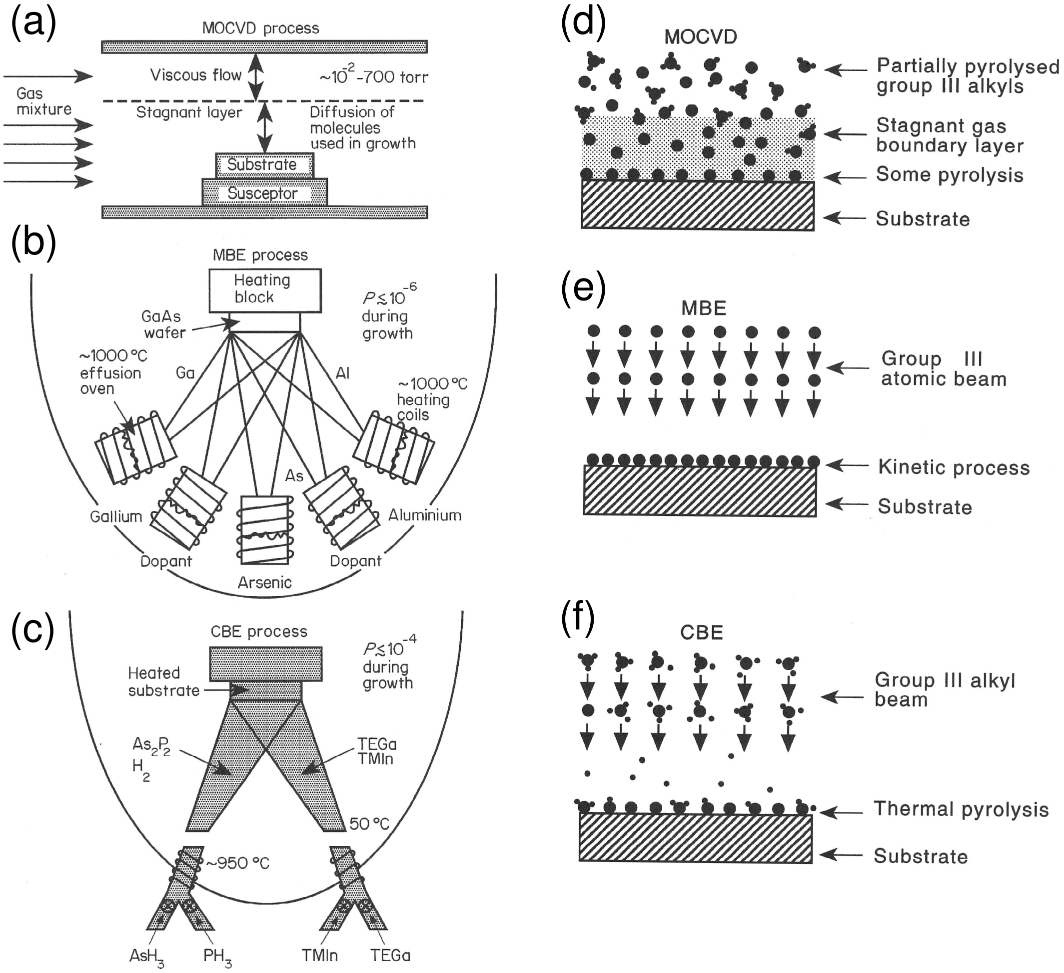

Figure 7 Left-hand side: schematic description of basic processes inside the growth chambers of (a) MOVPE, (b) MBE, and (c) CBE systems. Right-hand side: schematic of the growth kinetics involved in (d) MOVPE, (e) MBE, and (f) CBE system. Adapted from G. J. Davies *et al.* [21].

Chemical-beam epitaxy (CBE) is a newer development in epitaxial technology which combines the beam nature of MBE and the use of all vapor sources as in MOVPE. The beam nature in CBE allows it to prepare semiconductor heterostructures with monolayer abruptness and thickness control as achieved by MBE, while the use of vapor sources provides precise reproducible flux control with instantaneous response.

In CBE, all the sources are introduced into the system via the vapor phase at room temperature in the form of volatile chemicals. For the growth of III-V semiconductors, the group III elements are derived from pyrolysis of metal organic compounds, like in the MOVPE (e.g. TMIn, TEGa, TEAl, or occasionally inorganic compounds), on the heated substrate surface. The group V elements result from the decomposition of hydrides such as AsH_3 and PH_3, using a high-temperature cracker maintained at around 900 ˚C. The cracker decomposes AsH_3 and PH_3 into As_2, P_2, and H_2.

The growth mechanisms are very different in CBE from those of MBE and MOVPE, as depicted in Fig. 7 and 8. In MBE, the atomic group III beams impinge on the heated substrate surface, migrate into the appropriate lattice sites, and deposit epitaxially in the presence of excess group V molecular beams, usually dimmers or tetramers. Since the sticking coefficient of the group III atoms on the substrate surface at typical growth temperatures is practically unity, the growth rate is determined by the arrival rate of the group III atomic beams, no chemical reaction is involved in deriving the group III atoms at the substrate surface as they are generated by thermal evaporation from solid elemental sources.

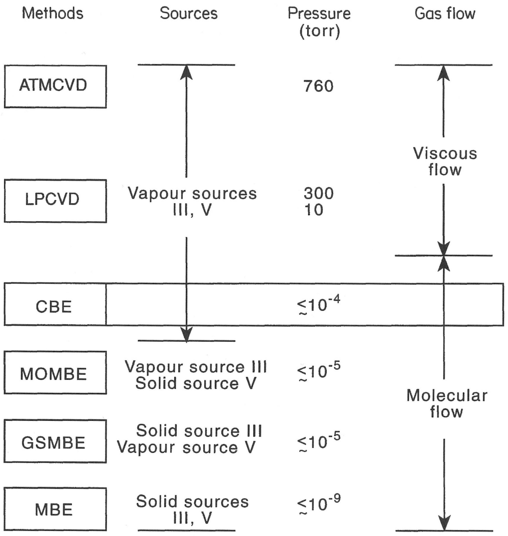

Figure 8 The relationship between various epitaxial techniques. Note that only the CBE combines a beam nature with the use of all vapour sources. Adapted from G. S. Davies *et al.* [21] (ATMCVD: atmospheric pressure chemical vapour deposition, LPCVD: low pressure chemical vapour deposition, MOMBE: metal organic MBE, GSMBE: gas source MBE).

In atmospheric or low-pressure MOVPE, the group III alkyls in the gas stream of H_2 are already partially dissociated. They then diffuse through a stagnant boundary layer above the heated substrate; further dissociation yields the atomic group III elements. These migrate into the appropriate lattice sites and deposit epitaxially by capturing a group V atom, either at the heated substrate surface or in the gas stream. For usual growth temperatures, the growth rate is limited by the diffusion rate of group III alkyls through the boundary layer.

In CBE, the beam of group III alkyls molecules impinges directly on to the heated substrate surface as in MBE. There is no boundary layer in front of the substrate surface, nor are there molecular collisions because of the long mean-free path of the molecules at the pressure of less than 5×10^{-5} Torr. Thus, after a group III alkyl molecule strikes the substrate surface, it can either acquire enough thermal energy from the heated substrate and dissociate all its three alkyl radicals, leaving the elemental group III atom on the surface, or re-evaporate in undissociated or partially dissociated forms. The probability of which process occurs depends on the substrate temperature and arrival rate of the organometallics. Thus, at a high enough substrate temperature, the growth rate is determined by the arrival rate of group III alkyls, while at lower substrate temperatures the growth rate is limited by the surface pyrolysis rate. In all growth processes, the group V material is always supplied in excess.

1.5 Fabrication of Self-Assembled QDs and Related Quantum-Confined Materials

Nanofabrication technologies in general tends to fall into two basic categories distinguished by the approach the nanostructures, in particular QDs, are formed. The *top-down* approach refers to the formation of nanostructures by utilizing lithography techniques which in principle provides the ultimate control of dimensions, and shape. In practice, however, it suffers from the size limitations of lithographic technologies, electronic and optical interface quality, etching defects, and the low throughput of serial lithographic processes. It has been shown that the radiative efficiencies of such quantum dots are not that suitable for device applications [22,23]. Nevertheless, the method has been very successful in producing relatively large (>100 nm diameter) semiconductor QDs [24] and other nanostructures and is ideally very suitable for mass-production industry.

Another approach so-called *bottom-up* technique is the method utilizing the QDs assembling to start from the fundamental building blocks of the crystals, i.e., atoms or molecules. By this technique the self-assembled QDs are defect-free and have highly structural and optical qualities. However, due to the *spontaneous* (also termed *self-assembled*) nucleation process it leads to relatively large size and shape distributions of such grown QDs. Moreover, the nucleation sites of the QDs are not controllable which makes the implementation into device applications difficult to accomplish. Typical bottom-up techniques that are commonly used are epitaxial growth of QDs using the strain driven Stranski-Krastanow (S-K) growth mode, droplet epitaxy technique, and formation of QDs in liquids using colloidal synthesis techniques.

In this section the general principles of self-assembled bottom-up QD fabrication techniques such as S-K growth mode and droplet epitaxy method will be briefly discussed. Apart from a solely bottom-up technique, an intermediate approach so-called *seeded QDs* which involves self formation of nanostructures at nucleation sites introduced by substrate patterning will be discussed. Cleaved edge overgrowth (T-shaped quantum dot) and the quasi-quantum dots generated by fluctuations in quantum wells will be shortly addressed. Finally, the novel technique of quantum dot growth in nanowires and colloidal QD nanocrystals from chemical synthesis are discussed. Apart from those mentioned fabrication techniques, the quantum dots can also be prepared by other methods such as etching or local interdiffusion of conventional quantum wells or quantum wires [25-27] or using electrostatic gates to confine the carriers [28] which is not included in this section.

1.5.1 Stranski-Krastanow (S-K) Growth Mode QDs

The Stranski-Krastanow (S-K) growth mode describes the characteristics of 3-D island growth with a thin 2-D layer beneath when a layer of material with larger lattice constant is epitaxially grown on top of a material with smaller lattice constant. The important term to determine the S-K growth mode is the lattice mismatch between the two epitaxial layers. For instance, the common combination of InAs and GaAs has a lattice mismatch of 7%, whereas InAs/InP system has a lattice mismatch of 3%, Ge/Si system has a lattice mismatch of 4%, or the InSb/GaSb system has a lattice mismatch of 6%, etc. The growth initially progresses with a pseudomorphic growth mode forming a strained 2-D film, the wetting layer. This causes the formation of a compressive strain in the forming layer, as described in Fig. 9. When this strain accumulates in the film and reaches a certain amount at the critical thickness, the growing material matrix experiences a phase transition from a 2-D layer-by-layer growth to a 3-D island growth. Naturally, the critical thickness is determined by the selection of materials on the heteroepitaxial systems.

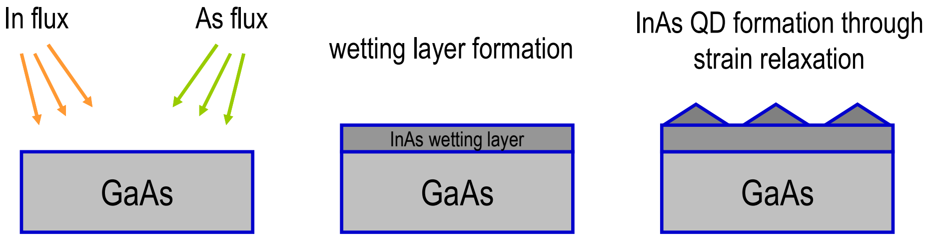

Figure 9 Schematic illustration of InAs quantum dot formation on GaAs substrate in the Stranski-Krastanow growth mode.

Figure 10 (a) shows typical InAs/GaAs (100) quantum dots grown in the S-K growth mode by MBE having a surface density of 5 × 10^{10} cm^{-2}. The cross-sectional transmission electron microscope (XTEM) image of a single dot is shown in Fig. 10 (b). The pyramids have a base diagonal of 20 nm and height of 7 nm. The QD structure properties like size, shape, composition and density can be tuned by changing the growth parameters during growth. The detailed studies are reviewed in many references [20,29-31]. The QDs grown by S-K growth mode are indeed defect-free giving rise to a high quality of structural and optical properties. However, due to the self-assembling process, size fluctuations and randomly distributed nucleation sites are unavoidable.

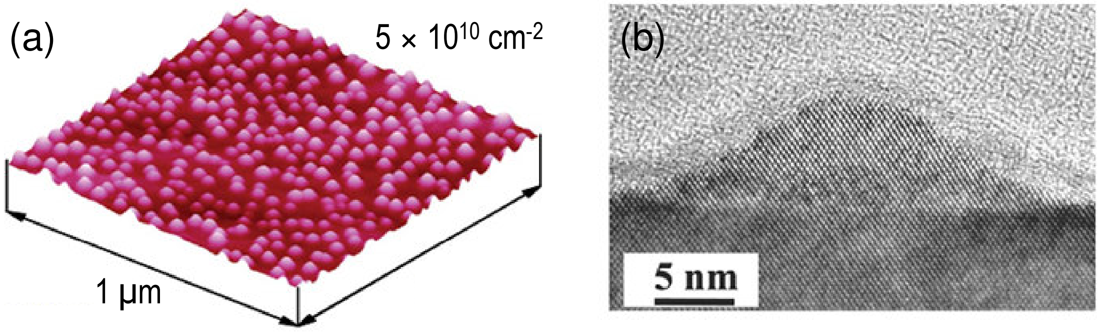

Figure 10 (a) Atomic force microscopy image of an InAs quantum dot layer on GaAs substrate. (b) Cross-sectional transmission spectroscopy image of a single InAs quantum dot grown on GaAs substrate. Adapted from P. Bhattacharya and Z. Mi [32].

1.5.2 Droplet Epitaxy QDs

A novel self-assembling growth method, termed Droplet Epitaxy, for the direct formation of QDs was developed in 1990s by Koguchi *et al.* [33]. Compared with the island formation based on the S-K growth mode, the Droplet Epitaxy is useful for the formation of QDs not only in lattice-mismatched but also in lattice-matched systems such as GaAs/AlGaAs or InSb/CdTe. The process of Droplet Epitaxy in the MBE chamber consists of forming numerous group III element liquid metal droplets such as Ga or

InGa on the substrate surface first by supplying their molecular beams. Droplets form based on the Volmer-Weber growth mode because the binding energy between adatoms is greater than that of the adatoms and the substrate surface atoms. The succeeding exposure of the group III droplets to a group V molecular beam such as As leads to the formation of GaAs or InGaAs III-V semiconductor nanocrystals, shown in Fig. 11. This transition process and interaction between group V and III materials are typically known as "crystallization". Another advantage of the Droplet Epitaxy is the possibility of the fabrication of QD structures without wetting layer by controlling the stoichiometry of the substrate surface just before the deposition of III element droplets.

The Droplet Epitaxy approach offers new opportunities for the fabrication of novel configurations of quantum- and nanostructures, such as 3-D quantum ring structures [34], QD molecules, and other novel configurations of quantum structures [35], [28]–[30]. The self-assembled QDs grown by Droplet Epitaxy are strain-free, nearly pure materials, whereas the S-K QDs often have intermixing and strain-related effects. However the crystalline and optical qualities of the QDs are degraded due to the required low deposition temperatures, therefore, post-growth annealing is essential to restore the crystalline quality.

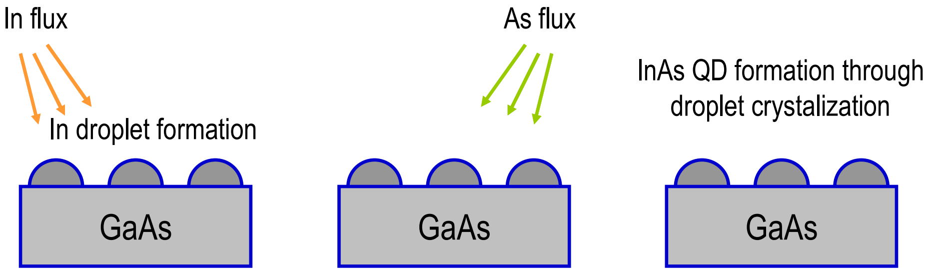

Figure 11 Schematic illustration of InAs quantum dot formation on GaAs substrate by droplet epitaxy method.

1.5.3 Lithographic Pattern Induced (seeded) QDs

By combining the approaches for nanostructure formation of *bottom-up* and *top-down* techniques together with the anisotropic growth rate on different facet profiles, one can produce quantum confined structures such as QDs with well-controlled nucleation sites.

For instance Hartmann *et al.* [36] has demonstrated the fabrication of pyramidal QDs which are depicted schematically in Fig. 12. By this technique, prior to the epitaxial growth, the (111)B GaAs substrates are patterned with arrays of inverted pyramids using wet chemical etching through resist masks prepared by photolithography or electron beam lithography. The preferential chemical etching exposes slowly-etched {111}A crystallographic planes that define the facets of inverted, tetrahedral pyramids. Subsequent growth of a multilayer structure using MOVPE yields a QD heterostructure within each inverted pyramid. In this case, for MOVPE growth on nonplanar (111)B GaAs substrates patterned with inverted tetrahedral pyramids, the side-walls composed of near-{111}A facets have a more efficient rate of metalorganic precursors decomposition than the bottom facets [(111)B for the pyramids]. This yields a higher growth rate on the sidewall facets, which leads to shrinking of the width of the bottom facets.

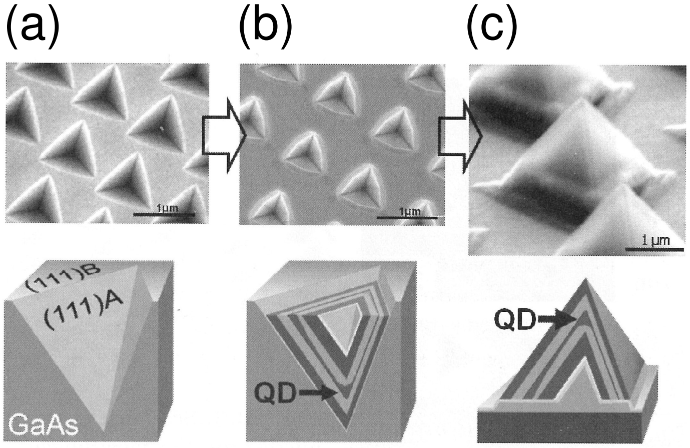

Figure 12 Fabrication steps of pyramidal quantum dots on patterned (111)B substrates: schematic illustration (lower panel) and scanning electron microscope images (upper panel). (a) Substrate patterning with arrays of inverted pyramids. (b) MOVPE growth of the quantum dot heterostructures. (c) Substrate removal and formation of upright pyramidal quantum dot heterostructure. Adapted from E. Kapon [37].

Under typical growth conditions, the growth rate on the GaAs (111)B facet is negligible as compared with that on the {111}A facets until the system reaches a self-limited profile. The equality of growth rates happens when the growth rate on (111)B is the same as the sidewalls growth rate due to capillarity contributions. Once the system has reached a self-limited profile, the growth of an InGaAs layer takes place with a thickening of the bottom profile compared to the sidewall profiles. A lens shaped QD is formed at the bottom of the pyramid due to the combination of growth rate anisotropy and capillarity effects [36-40].

Another example of low dimensional structures formation using growth rate anisotropy on nonplanar substrates was demonstrated by Nötzel *et al.* [41,42]. They showed that 15-20 nm high mesa stripes prepared by wet chemical etching oriented along the [0-11] direction on a (311)A GaAs substrates has anisotropic sidewall growth where one side has a fast-growing sidewall. The growth rate on this sidewall is larger than that on the mesa top or bottom resulting in a convex smooth curved profile surface. The formation of thicker GaAs region along the mesa edge due to the preferential migration of Ga atoms from both sides towards the sidewall leads to the development of a quantum wire-like structure as shown in Fig. 13. The thicker GaAs region causes a lowering of the bandedge energy with subsequent formation of a carrier confinement potential perpendicular to the mesa edge. On the contrary the opposite sidewall and the mesa stripes along [2-3-3] are characterized by a slower growth rate with the consequent development of a concave surface profile.

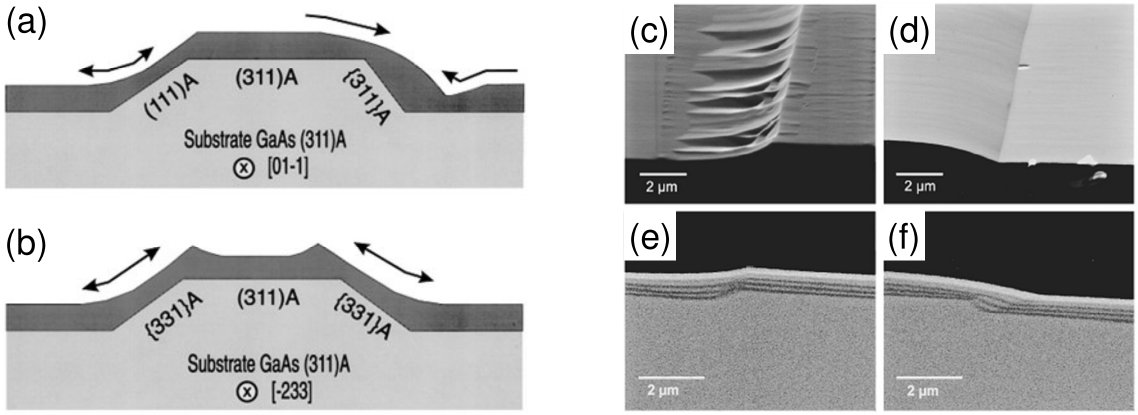

Figure 13 Left-hand side: schematic of the growth mode on patterned GaAs (311)A substrates with mesa stripes oriented along the (a) [01-1] and (b) [-233] directions. The arrows indicate the preferential migration of Ga atoms resulting in the selectivity of the growth across the edges. Right-hand side: Scanning electron microscope images of the edges of the mesa stripe along [01-1] after overgrowth (c) of the slow growing and (d) of the fast growing sidewall. In (e) and (f) the backscattered electron microscope images of the corresponding cross sections are shown. Adapted from R. Nötzel *et al.* [41].

Further fabrication of QD structures was developed on the alternated misalignment of the mesa stripes (zig-zag pattern) from [0-11] on patterned GaAs (311)A [43-45]. The creation of dot-like structures with locally thicker layer thickness, i.e., smaller bandgap energy at the corner of two intersecting mesas which are symmetrically inclined from the [0-11] azimuth leading to wire-like structures with larger bandgap energy was realized as shown in Fig. 14.

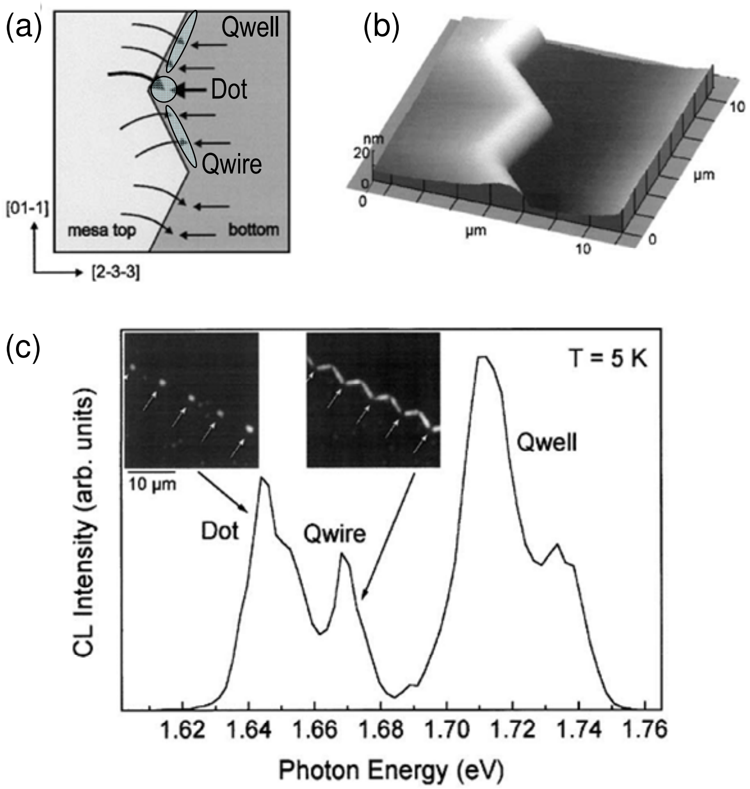

Figure 14 (a) Schematic top view of the quantum wire-dot structure. The zigzag lithographic patterning of the substrates and fast-growing sidewall give rise to the formation of quantum wire along the sidewall and a dot at the corner of two intersecting sidewalls pointing on the mesa top side. The arrows indicate the preferential migration of Ga adatoms. (b) AFM image of 20-nm-high mesa structure after overgrowth. (c) Area-averaged cathodoluminescence (CL) spectrum from the zigzag structure taken at 5 K. The inset shows the CL images detected at the quantum wire and quantum dot peak energy. Adapted from K. H. Ploog and R. Nötzel [45].

1.5.4 Cleaved Edge Overgrowth

According to this approach the QWs and QDs can be fabricated by cleaving the grown heterostructure sample in situ and perform an overgrowth process. As schematically illustrated in Fig. 15, a single QD is fabricated at the intersection of the three QWs, which are grown on three different surfaces. First, a conventional GaAs/AlGaAs QW structure is grown on the GaAs (100) substrate. Then the *in situ* cleaving of the substrate is performed in ultra high vacuum condition. The cleaved cross-sectional edge on either (110) and (-110) is treated as the new surface for growth of the second quantum well. The electron and hole can be confined at the intersection region of the T-junction edge, resulting in a T-shaped QW [46,47]. Another cleave on the new intersection and over growth of a conventional QW on another direction results in additional carrier confinement at the intersection of these three QWs and acts as a QD, T-shaped QD [48]. This technique can be extended to the growth of coupled QDs system by close stacking of the QWs with well-defined separation layer, shape, and composition [49]. Despite the well-positioning by the control of QW thickness and separation layer, the major drawback of this technique is that the QDs have a rather weak confinement potential.

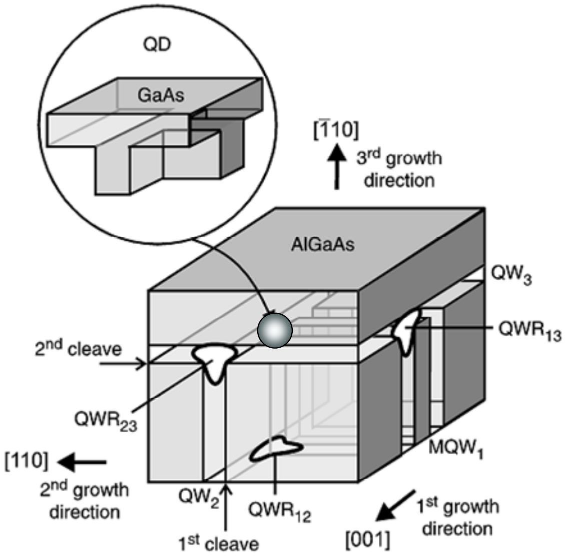

Figure 15 Schematic illustration of the QD structure obtained after three growth steps separated by two *in situ* cleaves. The junction of three QWs and QWRs, at which a QD forms, is shown in the magnified part of the figure. The T-shaped contours are lines of constant probability for electrons confined in the QWRs. Adpated from W. Wegscheider *et al.* [48].

1.5.5 Fluctuations in QWs

Ideally the heterostructure QW grown by sandwiching a layer of semiconductor of smaller bandgap by the material with larger bandgap, has the charge carriers confined along the QW direction. In practice, the interfaces of the heterostructure are not that perfect and it has been reported that interface roughness or fluctuation in the QW thickness can provide additional lateral confinement, shown schematically in Fig. 16. For example, in AlGaAs/GaAs QWs the effect of strain is minimized and the two-dimensional growth mode (Frank-van der Merwe) during the QW formation takes place. Depending on the growth parameters, the interfaces between AlGaAs and GaAs can be atomically smooth in local regions, but in some regions the roughness of the lower and upper interfaces are not the same. The bottom surface is rougher compared to the top one because of the larger diffusivity of Ga compared to Al at the same growth temperature. Such roughness may effectively generate traps for the motion of excitons in regions with sizes comparable to the Bohr radius and acts as a quantum dot [50-52]. Not only the monolayer thickness fluctuations but also the local fluctuations in the material compositions play the role to generate potential wells for charged carriers.

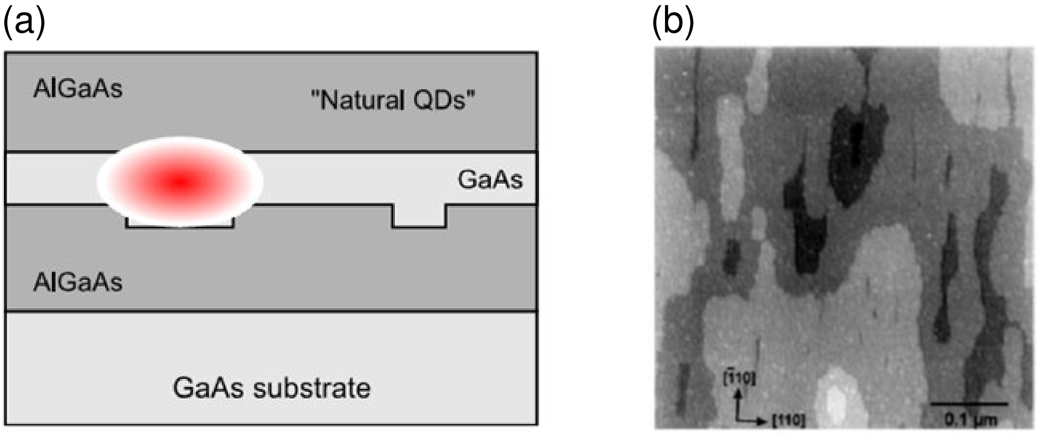

Figure 16 (a) Schematic illustration of excitons confined at thickness fluctuations of thin QW [53]. (b) A representative scanning tunneling microscope image of a GaAs surface which has been kept at growth temperature for several minutes under an As flux before being cooled and measured. The change in grey scale correspond to 1 monolayer-high changes in height [50].

1.5.6 QDs in Nanowires

A novel method to produce nanowires has been developed based on vapor-liquid-solid growth during MOVPE on surfaces covered with metallic nanoparticles, for instance Au, which act as catalysts [54-56]. For the material growth point of view, one can start to deposit Au nanoparticles on the substrate, then, under certain growth conditions the nanowires are created under the Au-alloy clusters, as shown in Fig. 17. The wire diameter depends on the size of the nanoparticles, which can be varied from 10 – 100 nm. In order to create a three-dimensionally confined structure, one can add another confinement by the selective axial versus radial growth of different materials along the wire direction. By properly tuning the precursors supplied during the growth, semiconductor heterostructures such as InAs/GaAs, InAsP/InP can be fabricated along the wire axis to produce QDs. In addition, the growth mechanism leading to core-shell growth can be adjusted by changing the growth parameters leading to many possible structures [57,58].

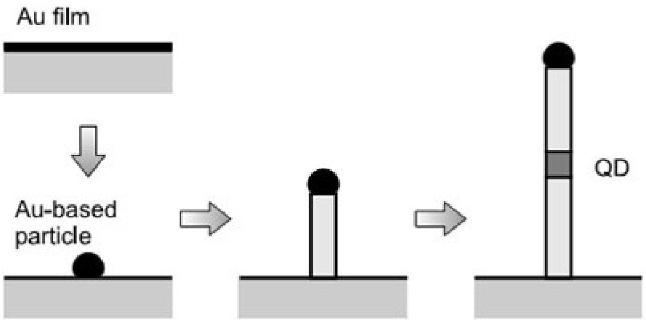

Figure 17 Schematic illustration of quantum dot in a nanowire. (a) Film of Au is deposited on a substrate. (b) By annealing, Au-based nanoclusters are formed. (c) The nanowire grown from Au-alloy cluster during MOVPE via vapour-liquid-solid transition. (d) Quantum dot can be realized by switching the deposited materials, e.g. from GaAs to InAs [53].

1.5.7 Colloidal QDs (nanocrystals)

Another kind of quasi-spherical nanocrystals with monodisperse nanometer size synthesized from chemical solution is called colloidal QD. In general, colloidal semiconductor nanocrystals are synthesized from precursor compounds dissolved in solutions, much like traditional chemical processes. The synthesis of colloidal QDs is based on a three-component system composed of: precursors, organic surfactants, and solvents which are widely discussed by many research groups [59-64]. It was first discovered by the group of L.E. Brus at Bell Labs where they developed the methodologies to produce large amounts of semiconductor QD materials that they also possessed unique optical and electrical properties [65].

The emission wavelength is tuned by changing the nanocrystal size as the bandbap of the material changed. In practice the colloidal nanocrystals are covered by a shell of one or two monolayers of another higher bandgap semiconductor material in order to passivate the unbound electrons on the surface and improve the quantum yield. Such nanocrystals are labeled as core-shell colloidal QD. Typical material types of colloidal nanocrystals are, e.g. CdSe/ZnS [59,60], CdSe/CdS [61], CdTe/ZnS [62], InP/ZnS [63], or PbSe/PbS [64], etc.

The main advantages of such colloidal QDs are the flexibility of the synthesis methods and the ability of mass production. The application to biological systems is also one of the strong points of such quantum dots due to the ability to combine them with molecular linkers or functionalize the shell with biofunctional molecules such as antibodies, antigens, enzymes, growth factor molecules, etc. Moreover, the advantages of using colloidal QDs also span to the area of optoelectronics devices such as solar cells, photodetectors, and light-emitting diodes due to the flexibilities of multi-colour capability of a variety of available QDs and many matrix materials. The drawbacks of this kind of nanocrystal are the stabilization of the emission where the “blinking” can happen when the nanocrystal switches randomly between an "on" fluorescent and an "off" non-fluorescent state which could be explained by the loses charge to a surface-trap state [66,67].

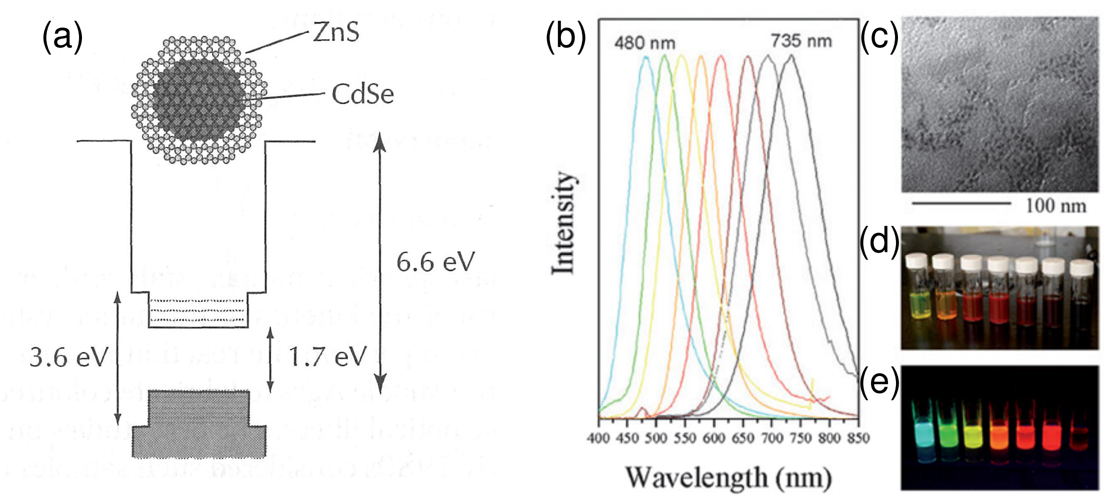

Figure 18 Left-hand side: (a) Schematic of a CdSe/Zns nanocrystals, and the corresponding three-dimensional potential well. The dotted lines symbolize the discrete set of accessible energy levels [68]. Right-hand side: (b) PL spectra of differently sized InP/ZnS core-shell nanocrystals. (c) TEM micrograph of a typical InP/ZnS nanocrystals sample with the mean diameter of 4.5 nm. As-prepared differently sized InP/ZnS nanocrystals exhibit stronf luminescence under (d) room light and (e) UV irradiation. Adapted from S. Xu *et al.* [63].

1.6 Applications of QDs and Challenges

The possible applications of semiconductor QDs have been widely explored in many branches from optic to electronics. Most prominent application of the QDs is in the area of optoelectronics and data telecommunication, as mentioned earlier in Section 1.2. QDs have shown to improve the device characteristics of many optical devices as the results of carrier confinement and delta-function of the density of states, as described in Section 1.3. The majority of research has concentrated on the development of quantum dot lasers [32], for which performance improvements including low and temperature-insensitive threshold current density [11,12], zero linewidth enhancement factor [69,70] and increased modulation speed [71] had been predicted. The emission wavelength of such devices can be tuned into 1.3-1.55 μm compatible with telecommunication wavelengths with the minimum attenuation in optical fibre. Recently the very first QD laser based on the InAs/GaAs system has been commercialized [72]. Figure 19 shows the advancements in the reduction of the threshold current density of bulk, QWs, and QD lasers in recent years showing the superior characteristic over the bulk and QWs counterparts.

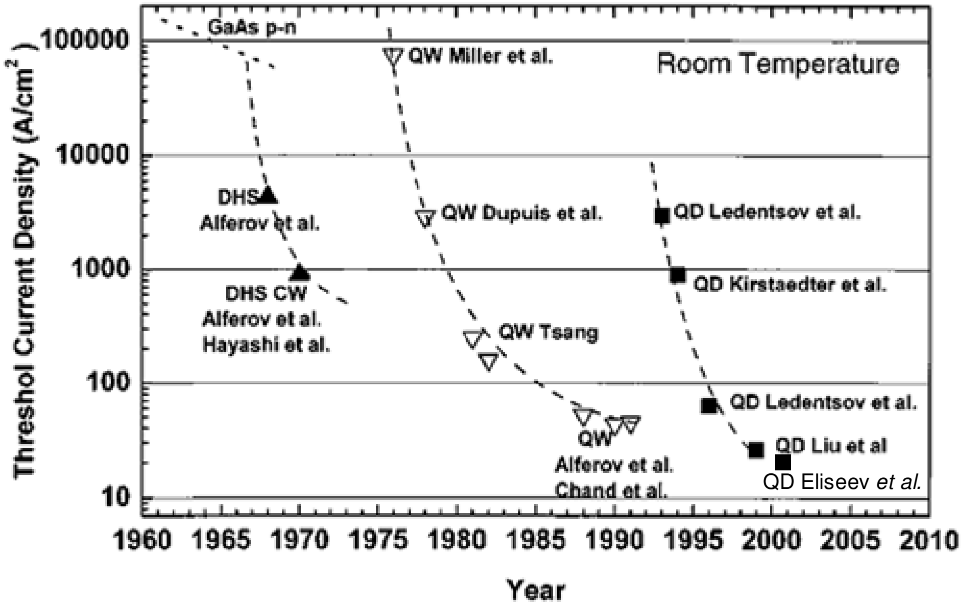

Figure 19 Decrease of the threshold current density of semiconductor heterostructure lasers with different dimensionality of the active layer. Adapted from N. N. Ledentsov *et al.* [73]

It is, however, due to the limitation in the fabrication processes of epitaxial QDs which mostly relied on the spontaneous S-K growth mode that the QDs size fluctuation, material intermixing, and random site distribution are inevitable. For the ideal case, the energy levels of all QDs should be the same. This means that the size, shape, and alloy composition of the QDs need to be close to identical. Then, the inhomogeneous broadening of QD luminescence due to size fluctuations is eliminated, resulting in a real concentration of the electron energy states. For QD laser applications, minimization of the inhomogeneous linewidth is highly desirable, however, some certain types of devices take advantage of the broad inhomogeneous broadening due to the scattered size distribution such as semiconductor optical amplifiers (SOAs) with broad gain spectrum.

For the QD-based SOAs, large bandwidth gain [74], fast gain recovery [75,76], and pattern-effect-free amplification [77,78] is expected and has been demonstrated. The polarization insensitivity has been demonstrated in a quantum dot SOA through close stacking of many dot layers to form columnar dot structure [79,80]. The broad emission and gain that can be obtained from QDs due to the variation in size and composition of the many QDs within the ensemble has also been exploited for high-power, broadband emission from superluminescent light-emitting diodes (SLEDs), which may be used for eye-safe biomedical imaging applications. Output power of several hundred mW have been demonstrated from QD-based SLEDs [81]. The inhomogeneously broadened optical response of a QD ensemble can also be exploited in saturable absorber structures, either as semiconductor saturable absorber mirrors (SESAMs), used to mode lock solid state lasers for ultrashort (fs) pulse generation [82], or as absorber sections integrated into QD lasers for direct modulation [83].

The use of QDs as the basic unit in single photon sources is also an attractive application for metrology [84], quantum key distribution [85] and linear optical quantum computing [86]. Single photon emission has been demonstrated from a variety of sources, including single molecules [87,88], nitrogen vacancies in diamond [89], and from QDs [90,91]. QDs are particularly attractive as single photon sources because they can be incorporated into standard optoelectronic device structures allowing electrical operation of the source and integration into optical fibre communication system. As mentioned earlier, typical growth conditions yield quantum dot ensembles with the density of ~ 10^{10} cm^{-2} (100 μm^{-2}). However, in order to isolate single QD emission in practical device structures a QD density approaching 10^{8} cm^{-2} (1 μm^{-2}) is required. Growth on patterned substrates has also been shown to result in low QD density, by preferential QD nucleation in nanoholes [92] or growth of QDs on pyramidal structures [93]. Alternately, it is possible to significantly reduce the QD density on conventional substrates through accurate control of growth conditions, for example by reduction of the InAs quantum dot growth rate together with further sample treatment such as mesa etching to isolate the single QD emission has also been demonstrated [94].

For a practical single photon sources it is advantageous to place the QDs within a microcavity in order to increase the photon extraction efficiency. Placing the QDs within planar microcavity structure, with a distributed Bragg reflector (DBR) mirror below the QD layer, has been shown to improve the photon collection by a factor of ten [95]. Further modification of the microcavity design by introducing lateral confinement of the optical modes, for example by using micropillars [96], microdisks [97] or photonic crystal cavities [98], can result in significant enhancement of the spontaneous emission into a cavity mode due to the Purcell effect [99]. For instance, the spontaneous emission rate from InAs/GaAs QDs has been enhanced by 5 times when the QDs were incorporated into a micropillar and by 15 times into a microdisk [97].

Furthermore, there has been growing interest in extending the concept of the QD single photon source to realize polarization-entangled photon sources, for quantum information applications including alternative key distribution methods in quantum cryptography [100]. This requires photons from the source to be indistinguishable [101]. By a photon interference experiment, Santori *et al.* have shown that consecutive photons from an InAs/GaAs quantum dot micropillar single photon source matched the requirement [102], and this has been used to generate polarization-entangled photon pairs using post-selected photons from the source utilizing the exciton emission. However, the major obstacle in the realization of entangled photon sources is the fine structure splitting (typically in order of tens µeV for InGaAs/GaAs QDs [103]) arisen from the QD asymmetry [104], often due to elongation in the [0-11] direction, and also from the carrier confinement [105], leading to a large electron-hole wavefunction overlap [106,107]. The fine structure splitting results from a lifting of the degeneracy of the spin-up and spin-down bright exciton states due to the electron-hole exchange interaction.

Exploitation of the spin of carriers in semiconductor devices is currently the focus of considerable research interest. Research concerning spintronics focuses on development of magnetic materials, spin injection into semiconductors and subsequent spin transport, manipulation and detection. The use of spin of individual QDs as information bits in quantum computing (qubits) [108-110] has gained considerable attraction due to the relatively long spin relaxation times of excitons in QDs. Recently, an electron spin lifetime of over 20 ms at low temperature (1 K) was reported from InGaAs/GaAs QDs in a 4 T external magnetic field [111] leading towards many applications such as QD charge and spin memory devices [112]. However, this is an emerging field of research and many aspects of spin dynamics in QDs have yet to be clarified before significant advances towards device applications can be made.

In addition, several other applications of semiconductor QDs including solar cells [113,114], mid-infrared photodetectors [115,116], single electron transistors [117] have been proposed and demonstrated. In conclusion, today the challenges for quantum dot research cover the perfected fabrication control of size, shape, emission wavelength, and lateral positioning of epitaxial QD ensembles with reduction of the QD number to the individual single quantum dot level. This will allow the understanding and exploitation of single/multiple photon emission and the manipulation of spins inside the QDs which is key to future quantum functional devices operating at the single/multiple electron and photon level with controlled interactions.

1.7 Scope of This Thesis

The scope of this thesis concerns the growth and characterization of telecom wavelength one-dimensional and two-dimensional InAs/InP QD arrays on planar and patterned InP (100) and (311)B substrates grown by chemical beam epitaxy (CBE). The topic also covers the demonstration of shape transition between InAs/InP quantum dashes (QDashes) and QDs which is shown to be directly determined by the surface morphology of the lattice-matched InGaAsP buffer layer on InP (100) substrates. The formation of linearly or periodic square lattices of InAs QD arrays by the concept of self-organized anisotropic strain engineering has been demonstrated. The multilayer stacking of linear InAs QD arrays with identical emission wavelength is realized by adjusting the GaAs interlayer thickness beneath the InAs QD layer demonstrating a three-dimensionally self-ordered QD crystal. The structural and optical properties of those InAs QD arrays in this work are characterized mainly by atomic force microscopy and photoluminescence techniques. Further investigation of complex QD arrays fabrication has been carried out by combining the step engineering on artificially patterned substrates with self-organized anisotropic strain engineering. Tuning of the photoluminescence emission wavelength of such QD arrays into 1.55-µm wavelength region through the insertion of an ultrathin GaAs interlayer underneath the QDs satisfies the requirements for incorporation into telecom applications and provides the building block for future quantum functional nanophotonic devices ultimately operating down to the single/multiple electron and photon level.

The overviews of low-dimensional nanostructures, particularly QDs, including the fabrication techniques and applications were briefly introduced in this introduction Chapter. Chapter 2 will mainly discuss the lateral ordering of epitaxial QDs and the concept of self-organized anisotropic strain engineering, which is fundamentally important to the rest of the studies. Chapter 3 presents the experimental results on shape evolution of InAs/InP (100) QDashes and QDs studied by systematic changes of the growth parameters during InAs deposition. As the main message, we identify the surface morphology of the lattice-matched InGaAsP buffer layer as key parameter for the formation of either InAs/InP QDashes or QDs.

In Chapter 4, a systematic study of the development of linear one-dimensional InAs/InP QD arrays is presented. The formation of well-separated and uniform QD arrays is realized based on the self-organized anisotropic strain engineering of an InAs/InGaAsP superlattice template on InP (100) substrates. The dependences of substrate miscut and orientation are essential for the formation of QD arrays. We systematically show the influence of the growth parameters for the formation of the superlattice template to obtain the highest uniform QD arrays. The structural and optical characterizations reveal electronic coupling between the QDs inside the linear arrays with the emission wavelength tuned into the 1.55 µm telecom wavelength region through the insertion of a GaAs interlayer beneath the QD arrays.

Chapter 5 demonstrates the formation of two-dimensional InAs/InP QD arrays utilizing the distinct anisotropic migration on InP (311)B substrates. The InAs QDs are arranged in a periodic square lattice over macroscopic areas. Careful adjustments of the growth conditions during superlattice template formation are demonstrated to yield highly uniform two-dimensional InAs/InP QD arrays with the photoluminescence emission tuned into the telecom wavelength region both at room temperature and at low temperature (4.8 K).

In Chapter 6, the influence of steps on artificially patterned substrates on the formation of InAs/InP QD arrays is shown. The key result is the ability to alter the arrays orientation away from the intrinsic direction which is solely determined by the substrate miscut on InP (100) patterned substrates. This is essential for the formation of complex QD arrays and network required for next generation of quantum devices. In contrast, the facets formed on patterned InP (311)B substrates do not affect the QD arrays orientation on the top and bottom areas on both shallow and deep patterned structures. The lithographic processes and wet chemical etching details along with the pattern evolution are addressed in detail.

Finally, Chapter 7 provides the demonstration of multilayer-stacked linear InAs/InP QD arrays on InP (100) substrates. Identical emission wavelength of the stacked QD arrays in the 1.55-µm region at room temperature is achieved by increasing the thickness of the GaAs interlayer beneath the QDs in successive layers. The sub-monolayer increment of the GaAs interlayer thickness compensates the QD size and wavelength increase during vertical strain correlated stacking. This is the demonstration of a three-dimensionally self-ordered QD crystal with fully controlled structural and optical properties.

Bibliography

[1] http://www.lightemittingdiodes.org.

[2] http://en.wikipedia.org/wiki/Moore's_law.

[3] F. Braun, "Uber die Stromleitung durch Schwefwlmetalle," *Ann Phys. Chem.* **153**, 556 (1874).

[4] L. Esaki and R. Tsu, *IBM Res. Note*, RC-2418 (1696).

[5] L. Esaki and R. Tsu, *IBM J. Res. Devel.* **14**, 61 (1970).

[6] A. Y. Cho, "Film deposition by molecular beam technique," *J. vac. Sci. Technol.* **8**, S31 (1971).

[7] N. Holonyak Jr., R. M. Kolbas, R. D. Dupuis, and P. D. Dapkus, *IEEE J. Quantum Electron.* **QE-16**, 170 (1980).

[8] W. T. Tsang, *Appl. Phys. Lett.* **40**, 217 (1982).

[9] R. Chin, N. Holonyak Jr., B. A. Vojak, K. Hess, R. D. Dupuis, and P. D. Dapkus, *Appl. Phys. Lett.* **36**, 19 (1980).

[10] H. Iwamura, T. Saku, T. Ishibashi, K. Otsuka, and Y. Horikoshi, *Electron. Lett.* **19**, 180 (1983).

[11] Y. Arakawa and H. Sakaki, *Appl. Phys. Lett.* **40** (11), 939 (1982).

[12] M. Asada, Y. Miyamoto, and Y. Suematsu, *IEEE. J. Quantum Electron.* **QE-22** (9), 1915 (1986).

[13] L. Goldstein, F. Glas, J. Y. Marzin, M. N. Charasse, and G. Le Roux, *Appl. Phys. Lett.* **47** (10), 1099 (1985).

[14] Z. Alferov, *IEEE J. Sel. Topic. Quantum Electron.* **6**, 832 (2000).

[15] K. C. Kao and G. A. Hockham, *Proc. IEE* **113**, 1151 (1966).

[16] R. J. Mears and S. R. Baker, *Optical and Quantum Electronics* **24**, 517 (1992).

[17] N. K. Dutta and Q. wang, *Semiconductor Optical Amplifiers*. (World Scientific, London, 2006).

[18] http://www.telegeography.com.

[19] http://www.ece.umd.edu/~davis/optfib.html.

[20] Mohamed Henini, *Handbook of Self Assembled Semiconductor Nanostructures for Novel Devices in Photonics and Electronics*, First ed. (Elsevier, 2008).

[21] G. J. Davies, J. S. Foord, and W. T. Tsang, in *Chemical Beam Epitaxy and Related Techniques*, edited by J. S. Foord, G. J. Davies, and W. T. Tsang (John Wiley & Sons, Chichester, 1997), pp. 1-11.

[22] H. Benisty, C. M. Sotomayor-Torres, and C. Weisbuch, *Phys. Rev. B* **44**, 10945 (1991).

[23] F. E. Prins, G. Lehr, M. Burkard, S. Yu. Nikitin, H. Schweizer, and G. W. Smith, *Jpn. J. Appl. Phys.* **32**, 6228 (1993).

[24] L. P. Kouwenhoven, D. G. Austing, and S. Tarucha, *Rep. Prog. Phys.* **64**, 701 (2001).

[25] G. W. Bryant and G. S. Solomon, *Optics of Quantum Dots and Wires*. (Artech House, London, 2005).

[26] J. Y. Marzin, A. Izrael, L. Birotheau, B. Sermage, N. Roy, R. Azoulay, D. Robein, J. - L. Benchimol, L. Henry, V. Thierry-Mieg, F. R. Ladan, and L. Taylor, *Surf. Sci.* **267**, 253 (1999).

[27] K. Brunner, U. Bockelmann, G. Abstreiter, M. Walther, G. Böhm, G. Tränkle, and G. Weimann, *Phys. Rev. Lett.* **69**, 3216 (1992).

[28] J. P. Bird, *Electron Transport in Quantum Dots*. (Kluwer Academic Publisher, Dordrecht, 2003).

[29] D. Bimberg, M. Grundmann, and N. N. Ledentsov, *Quantum Dot Heterostructures*. (Wiley, Chichester, 1998).

[30] M. Sugawara, *Self-Assembled InGaAs/GaAs Quantum Dots*. (Academic Press, London, 1999).

[31] Zh. M. Wang, *Self-Assembled Quantum Dots*. (Springer, New York, 2008).
[32] P. Bhattacharya and Z. Mi, *Proc. of IEEE* **95**, 1723 (2007).
[33] N. Koguchi and K. Ishige, *Jpn. J. Appl. Phys.* **32** (5A), 2052 (1993).
[34] T. Mano, T. Kuroda, S. Sanguinetti, T. Ochiai, T. Tateno, J. Kim, T. Noda, M. Kawabe, K. Sakoda, G. Kido, and N. Koguchi, *Nano. Lett.* **5**, 425 (2005).
[35] J. H. Lee, Zh. M. Wang, N. W. Strom, Yu. I. Mazur, and G. J. Salamo, *Appl. Phys. Lett.* **89**, 202101 (2006).
[36] A. Hartmann, L. Loubies, F. Reinhardt, and E. Kapon, *Appl. Phys. Lett.* **71**, 1314 (1997).
[37] E. Kapon, in *Lateral Alignment of Epitaxial Quantum Dots*, edited by O. G. Schmidt (Springer, Berlin Heidelberg New York, 2007), p. 591.
[38] E. Pelucchi, M. Baier, Y. Ducommun, S. Watanabe, and E. Kapon, *Phys. Status. Solidi. b* **238**, 233 (2003).
[39] M. H. Baier, S. Watanabe, E. Pelucchi, and E. Kapon, *Appl. Phys. Lett.* **84**, 1943 (2004).
[40] Q. Zhu, K. F. Karlsson, E. Pelucchi, and E. Kapon, *Nano. Lett.* **7**, 2227 (2007).
[41] R. Nötzel, J. Menninger, M. Ramsteiner, A. Ruiz, H.-P. Schönherr, and K. H. Ploog, *Appl. Phys. Lett.* **68**, 1132 (1996).
[42] R. Nötzel, Z. C. Niu, M. Ramsteiner, H.-P. Schönherr, L. Däweritz, and K. H. Ploog, *Nature (London)* **392**, 56 (1998).
[43] J. Fricke, R. Nötzel, U. Jahn, Z. Niu, H.-P. Schönherr, M. Ramsteiner, and K. H. Ploog, *J. Appl. Phys.* **86**, 2896 (1999).
[44] J. Fricke, R. Nötzel, U. Jahn, H.-P. Schönherr, L. Däweritz, and K. H. Ploog, *J. Appl. Phys.* **85**, 3576 (1999).
[45] K. H. Ploog and R. Nötzel, *Physica E* **11**, 78 (2001).
[46] L. Pfeiffer, K. W. West, H. L. Stormer, J. P. Eisenstein, K. W. Baldwin, D. Gershoni, and J. Spector, *Appl. Phys. Lett.* **56**, 1697 (1990).
[47] L. Pfeiffer, H.L. Störmer, K. West, and K.W. Baldwin, *J. Crystal Growth* **111**, 333 (1991).
[48] W. Wegscheider, G. Schedelbeck, G. Abstreiter, M. Rother, and M. Bichler, *Phys. Rev. Lett.* **79**, 1917 (1997).
[49] G. Schedelbeck, W. Wegscheider, M. Bichler, and G. Abstreiter, *Science* **278**, 1792 (1997).
[50] D. Gammon, E. S. Snow, B. V. Shanabrook, D. S. Katzer, and D. Park, *Phys. Rev. Lett.* **76**, 3005 (1996).
[51] K. Brunner, G. Abstreiter, G. Böhm, G. Tränkle, and G. Weimann, *Phys. Rev. Lett.* **73**, 1138 (1994).
[52] A. Zrenner, L. V. Butov, M. Hagn, G. Abstreiter, G. Böhm, and G. Weimann, *Phys. Rev. Lett.* **72**, 3382 (1994).
[53] S. Kiravittaya, A. Rastelli, and O. G. Schmidt, *Rep. Prog. Phys.* **72**, 1 (2009).
[54] K. Hiruma, H. Murakoshi, M. Yazawa, and T. Katsuyama, *J. Crystal Growth* **163**, 226 (1996).
[55] M. S. Gudiksen, L. J. Lauhon, J. Wang, D. C. Smith, and C. M. Lieber, *Nature* **415**, 617 (2002).
[56] M. T. Borgström, V. Zwiller, E. Müller, and A. Imamoglu, *Nano. Lett.* **5**, 1439 (2005).
[57] L. J. Lauhon, M. S. Gudiksen, D. Wang, and C. M. Lieber, *Nature* **420**, 57 (2002).
[58] E. D. Minot, F. Kelkensberg, M. van Kouwen, J. A. van Dam, L. P. Kouwenhoven, V. Zwiller, M. T. Borgström, O. Wunnicke, M. A. Verheijen, and E. P. A. M. Bakkers, *Nano. Lett.* **7**, 367 (2007).
[59] M. A. Hines and P. Guyot-Sionnest, *J. Phys. Chem.* **100**, 468 (1996).
[60] B. O. Dabbousi, J. Rodriguez-Vieji, F. V. Mikulec, J. R. Heine, H. Mattoussi, R. Ober, K. F. Jensen, and M. G. Bawendi, *J. Phys. Chem. B* **101**, 9463 (1997).

[61] X. G. Peng, M. C. Schlamp, A. V. Kadavanich, and A. P. Alivisatos, *J. Am. Chem. Soc.* **119**, 7019 (1997).
[62] J. M. Tsay, M. Pflughoefft, L. A. Bentolila, and S. Weiss, *J. Am. Chem. Soc.* **126**, 1926 (2004).
[63] S. Xu, J. Ziegler, and T. Nann, *J. Mater. Chem.* **18**, 2653 (2008).
[64] M. Brumer, A. Kigel, L. Amirav, A. Sashchiuk, O. Solomesch, N. Tessler, and E. Lifshitz, *Adv. Funct. Mater.* **15**, 1111 (2005).
[65] R. Rossetti, R. Hull, J. M. Gibson, and L. E. Brus, *J. Chem. Phys.* **82**, 552 (1985).
[66] A. L. Efros and M. Rosen, *Phys. Rev. Lett.* **78**, 1110 (1997).
[67] M. Pelton, G. Smith, N. F. Scherer, and R. A. Marcus, *PNAS* **104**, 14249 (2007).
[68] L. Coolen, X. Brokmann, and J. P. Hermier, in *Handbook of Self Assembled Semiconductor Nanostructures for Novel Devices in Photonics and Electronics*, edited by M. Henini (Elsevier, 2008), p. 716.
[69] M. Willatzen, T. Tanaka, Y. Arakawa, and J. Singh, *IEEE. J. Quantum Electron.* **30**, 640 (1994).
[70] T. C. Newell, D. J. Bossert, A. Stintz, B. Fuchs, K. J. Malloy, and L. F. Lester, *IEEE Photon. Technol. Lett.* **11**, 1527 (1999).
[71] A. V. Uskov, Y. Boucher, J. Le Bihan, and J. McInerney, *Appl. Phys. Lett.* **73**, 1499 (1998).
[72] www.qdlaser.com.
[73] N. N. Ledentsov, M. Grundmann, F. Heinrichsdorff, D. Bimberg, V. M. Ustinov, A. E. Zhukov, M. V. Maximov, Zh. I. Alferov, and J. A. Lott, *IEEE J. Sel. Topic. Quantum Electron.* **6**, 439 (2000).
[74] M. Sugawara, N. Hatori, M. Ishida, H. Ebe, Y. Arakawa, T. Akiyama, K. Otsubo, T. Yamamoto, and Y. Nakata, *J. Phys. D: Appl. Phys.* **38**, 2126 (2005).
[75] T. Akiyama, O. Wada, H. Kuwatsuka, T. Simoyama, Y. Nakata, K. Mukai, M. Sugawara, and H. Ishikawa, *Appl. Phys. Lett.* **77**, 1753 (2000).
[76] T. W. Berg, S. Bischoff, L. Magnusdottir, and J. Mørk, *IEEE Photon. Technol. Lett.* **13**, 541 (2001).
[77] M. Sugawara, N. Hatori, T. Akiyama, Y. Nakata, and H. Ishikawa, *Jpn. J. Appl. Phys.* **40**, L488 (2001).
[78] A. V. Uskov, T. W. Berg, and J. Mørk, *IEEE J. Quantum Electron.* **40**, 306 (2004).
[79] T. Kita, O. Wada, H. Ebe, Y. Nakata, and M. Sugawara, *Jpn. J. Appl. Phys.* **41**, L1143 (2002).
[80] S. Anantathanasarn, R. Nötzel, P. J. van Veldhoven, F. W. M. van Otten, T. J. Eijkemans, and J. H. Wolter, *Appl. Phys. Lett.* **88**, 063105 (2006).
[81] Z. Y. Zhang, Z. G. Wang, B. Xu, P. Jin, Z. Z. Sun, and F. Q. Liu, *IEEE Photon. Technol. Lett.* **16**, 27 (2004).
[82] U. Keller, K. J. Weingarten, F. X. Kartner, D. Kopf, B. Braun, I. D. Jung, R. Fluck, C. Honninger, N. Matuschek, and J. Aus der Au, *IEEE J. Sel. Topic. Quantum Electron.* **2**, 435 (1996).
[83] M. G. Thompson, C. Marinelli, K. T. Tan, K. A. Williams, R. V. Penty, I. H. White, I. N. Kaiander, R. L. Sellin, D. Bimberg, D. -J. Kang, M. G. Blamire, F. Visinka, S. Jochum, and S. Hansmann, *Electron. Lett.* **39**, 1121 (2003).
[84] M. Oxborrow and A. G. Sinclair, *Contemp. Phys.* **46**, 173 (2005).
[85] N. Gisin, G. Ribordy, W. Tittel, and H. Zbinden, *Rev. Mod. Phys.* **74**, 145 (2002).
[86] E. Knill, R. Laflamme, and G. J. Milburn, *Nature* **409**, 46 (2001).
[87] Th. Basche, W. E. Moerner, M. Orrit, and H. Talon, *Phys. Rev. Lett.* **69**, 1516 (1992).
[88] B. Lounis and W. E. Moerner, *Nature* **407**, 491 (2000).
[89] C. Kurtsiefer, S. Mayer, P. Zarda, and H. Weinfurter, *Phys. Rev. Lett.* **85**, 290 (2000).
[90] P. Michler, A. Kiraz, C. Becher, W. V. Schoenfeld, P. M. Petroff, L. Zhang, E. Hu, and A. Imamoglu, *Science* **290**, 2282 (2000).

[91] Z. Yuan, B. Kardynal, R. M. Stevenson, A. J. Shields, C. J. Lobo, K. Cooper, N. S. Beattie, D. A. Ritchie, and M. Pepper, *Science* **295**, 102 (2002).
[92] P. Atkinson, S. P. Bremner, D. Anderson, G. A. C. Jones, and D. A. Ritchie, *J. Vac. Sci. Technol. B.* **24**, 1523 (2006).
[93] M. H. Baier, E. Pelucchi, E. Kapon, S. Varoutsis, M. Gallart, I. Robert-Philip, and I. Abram, *Appl. Phys. Lett.* **84**, 648 (2004).
[94] N. I. Cade, H. Gotoh, H. Kamada, H. Nakano, S. Anantathanasarn, and R. Nötzel, *Appl. Phys. Lett.* **89**, 181113 (2006).
[95] A. J. Bennett, D. C. Unitt, P. See, A. J. Shields, P. Atkinson, K. Cooper, and D. A. Ritchie, *Appl. Phys. Lett.* **86**, 181102 (2005).
[96] J. M. Gerard, B. Sermage, B. Gayral, B. Legrand, E. Costard, and V. Thierry-Mieg, *Phys. Rev. Lett.* **81**, 1110 (1998).
[97] J. M. Gerard and B. Gayral, *IEEE J. Lightwave Technol.* **17**, 2089 (1999).
[98] T. D. Happ, I. I. Tartakovskii, V. D. Kulakovskii, J. -P. Reithmaier, M. Kamp, and A. Forchel, *Phys. Rev. B* **66**, 041303 (2002).
[99] E. M. Purcell, *Phys. Rev.* **69**, 681 (1946).
[100] A. K. Ekert, *Phys. Rev. Lett.* **67**, 661 (1991).
[101] C. K. Hong, Z. Y. Ou, and L. Mandel, *Phys. Rev. Lett.* **59**, 2044 (1987).
[102] C. Santori, D. Fattal, J. Vuckovic, G. S. Solomon, and Y. Yamamoto, *Nature* **419**, 594 (2002).
[103] R. J. Young, R. M. Stevenson, A. J. Shields, P. Atkinson, K. Cooper, D. A. Ritchie, K. M. Groom, M. J. Steer, H. Y. Liu, and M. Hopkinson, *Phys. Rev. B* **72**, 113305 (2005).
[104] H. W. van Kesteren, E. C. Cosman, W. A. J. A. van der Poel, and C. T. Foxon, *Phys. Rev. B* **41**, 5283 (1990).
[105] E. Blackwood, M. J. Snelling, R. T. Harley, S. R. Andrews, and C. T. Foxon, *Phys. Rev. B* **50**, 14246 (1994).
[106] M. Bayer, A. Kuther, A. Forchel, A. Gorbunov, V. B. Timofeev, F. Schäfer, J. P. Reithmaier, T. L. Reinecke, and S. N. Walck, *Phys. Rev. Lett.* **82**, 1748 (1999).
[107] D. Gammon, E. S. Snow, B. V. Shanobrook, D. S. Katzer, and D. Park, *Phys. Rev. Lett.* **76**, 3005 (1996).
[108] D. Loss and D. P. DiVincenzo, *Phys. Rev. A.* **57**, 120 (1998).
[109] B. E. Kane, *Nature* **393**, 133 (1998).
[110] V. Cerletti, W. A. Coish, O. Gywat, and D. Loss, *Nanotechnology* **16**, R27 (2005).
[111] M. Kroutvar, Y. Ducommun, Heiss D, M. Bichler, D. Schuh, G. Abstreiter, and J. J. Finley, *Nature* **432**, 81 (2004).
[112] J. Finley, in *Handbook of Self Assembled Semiconductor Nanostructures for Novel Devices in Photonics and Electronics*, edited by M. Henini (Elsavier, 2008), p. 476.
[113] Q. Shao, A. Balandin, A. Fedeseyev, and M. Turowski, *Appl. Phys. Lett.* **91**, 163503 (2007).
[114] S. G. Bailey, S. Hubbard, and R. P. Raffaelle, in *Handbook of Self Assembled Semiconductor Nanostructures for Novel Devices in Photonics and Electronics*, edited by M. Henini (Elsavier, 2008), p. 552.
[115] S. Y. Wang, S. D. Lin, H. W. Wu, and C. P. Lee, *Appl. Phys. Lett.* **78**, 1023 (2001).
[116] A. D. Stiff, S. Krishna, P. Bhattacharya, and S. P. Kennerly, *Appl. Phys. Lett.* **79**, 421 (2001).
[117] K. Yano, T. Ishii, T. Hashimoto, T. Kobayashi, F. Murai, and K. Seki, *IEEE Trans. Electron. Devices* **41**, 1628 (1994).

CHAPTER 2

Lateral Positioning of Epitaxial Quantum Dots

ABSTRACT

An overview of lateral positioning of epitaxial self-assembled quantum dots in a number of approaches is given in detail. The techniques include strained multilayer stacking, pre-patterned substrates, multiatomic steps, cleaved edge overgrowth, and multilayer stacking on high-index substrates. Particularly a new concept enabling lateral ordering of self-organized quantum structures based on anisotropic strain engineering is discussed. The control of lateral QD alignment is the key to next generation quantum functional nano- and optoelectronic devices where quantum mechanical and electromagnetic interactions of single and multiple electrons and photons are well-controlled within the ordered QD networks.

2.1 Introduction

Self-assembled semiconductor quantum dots (QDs) have gained a lot of attraction owing to their unique physical and electronic properties arising from the three-dimensional carrier confinement and have led to applications as already described in detail in the previous chapter. In general to fabricate QDs, the self-assembled Stranski-Krastanow (S-K) growth mode is one of the most exploited techniques for obtaining high quality crystal structure and optical properties. On the other hand, the downside of this growth mode is that material fluctuations and a random QD distribution occur. This leads to an inhomogeneous broadening of the photoluminescence emission, which in some aspects, hinders the advantages of QD based devices. For novel advanced single QD devices, a precise position control of individual quantum dots in arrays is desirable for the integration in photonic cavities [1] or for further processing of the devices. Perfectly ordered QD arrays are also required for the observation of novel physical phenomena such as interference effects [2] and enhancement of excitonic optical nonlinearities [3]. The realization of well-positioned QD arrays, thus, gives rise to interesting physical phenomena which modify the fundamental material properties provided the basis for nanoelectronics/optics in future functional devices utilized for quantum information processing. For instance, coupled QDs array system with dot-to-dot interaction is a very promising candidate for the logical unit in a quantum computer as called "qubit" or quantum bit, which in principle can be realized by the two-level quantum system, e.g., the horizontal or vertical polarization of a photon or the up and down states of an electronic spins [4,5]. Thus, not only size, shape, and emission wavelength control are needed but also well-controlled aligned QDs nucleation is essential.

Several approaches to order self-assembled QDs were proposed and realized. The widely used techniques involved substrate pre-patterning by electron-beam lithography to effectively determine the QD nucleation sites over macroscopic length scale. By this technique, however, the structural and ,in particular, optical properties of the dots are significantly degraded due to defects which usually arise from lithographic and etching imperfections. Other techniques using the fundamental properties of substrate surface modification such as steps, cleaved edge overgrowth, or QD stacking have also been reported.

Recently, the technique of "self-organized anisotropic strain engineering" has been developed and led to a novel method for QD ordering maintaining high structural and optical quality. The concept relies on the self-organized construction of well-defined superlattice templates for QD ordering using local strain recognition. Linear one-dimensional QD arrays and two-dimensional square lattices of QD groups were created based on this technique with excellent photoluminescence emission up to room temperature of the QDs.

In this chapter, a general review of various self-alignment techniques of epitaxial QD growth will be addressed. In section 2.2, the principles of strained multilayer stacking for lateral and vertical QD positioning are summarized. An overview of substrate pre-patterning techniques to achieve the desired lateral positioning is given in section 2.3, together with other methods such as multiatomic steps and cleaved edge overgrowth which will be described in section 2.4. An emphasis on self-organized lateral QD ordering using high-index surfaces is discussed in section 2.5. A detailed description of the recently developed ordering mechanism based on self-organized anisotropic strain engineering, which is fundamentally important to the rest of this thesis, is provided in section 2.6. Finally, the general point of view for QD ordering is summarized in section 2.7.

2.2 Strained Multilayer Stacking

Three-dimensional stacking of self-assembled QDs in multilayers or superlattice structures has turned out to be one of the most effective techniques for controlling the vertical and lateral arrangement of the dots. This has been demonstrated in many references [6-9] showing that the main driving force for such vertically self-organized growth is the strain induced interaction with the buried dots which gives rise to a preferred direction for In atom migration. The pairing probability in vertical dots columns was first realized and explained by Xie *et al.* using a model in which the lowering of strain energy above the buried dots leads to an attraction of mobile surface In adatoms [6]. The local nucleation probability was then assumed to be proportional to the amount of accumulated InAs atoms at the strain minima. For small separation layer thickness which corresponds to deeper energy minima, the deposited atoms within the surface diffusion length are attracted, resulting in a unity dot pairing probability. When the thickness of the separation layer increases, the energy minima become shallower and thus the pairing probability reduces until the minima become too weak to induce a correlated dot nucleation, see Fig. 1.

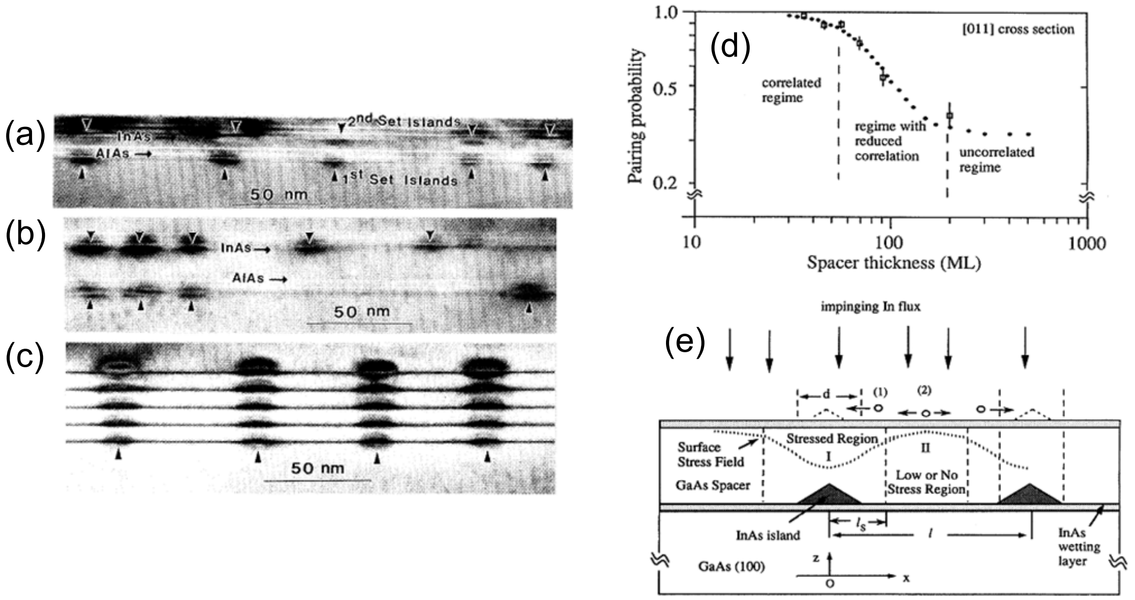

Figure 1 (a)-(c) Cross-sectional transmission electron microscopy images of InAs/GaAs multilayers with GaAs spacer thickness of (a) 46, (b) 92, and (c) 36 ML, where vertically collinearity of the InAs dots is form along the growth direction in (c). (d) Experimentally observed pairing probabilities (open squares) and model fitted data (filled circles) described in [6] as a function of the spacer thickness. (e) A schematic representation showing processes for the In adatom migration on the stressed surface. Adapted from Xie *et al.* [6].

With respect to the lateral ordering, Tersoff *et al.* have shown the improvement in lateral QD ordering in (001) SiGe/Si superlattices compared to single layers in 20 periods superlattices [7,8], shown in Fig. 2 (a) and (b). The improvement in size uniformity and lateral ordering in rows preferentially along <100> is revealed in the two dimensional Fourier transform power spectra shown in the inset. This self-organization occurs through the strain mediation by the Si spacer layers which can be understood by the model which involved strain-induced repulsion between the buried dots and the second nearest surface layer dots. Similar results presented by Solomon *et al.* show the improvement of lateral ordering due to anisotropic strain distribution in the cubic GaAs substrate [9]. Figure 2 (c) and (d) show the cross-sectional scanning tunneling microscopy images of five-fold stacked 2.4 ML InAs dots separated by 10 nm GaAs spacer layers taken by Bruls et al. [10]. The general feature of vertically aligned InAs dot superlattices which results in significant increases of the dot size and broadening of the shape along the vertical dot columns is demonstrated.

The preferential nucleation in multilayer superlattices induces local enhancement of the growth rate, local changes in surface diffusivity, local decreases in the critical wetting layer thickness or energy barrier for island nucleation which directly result in significant changes in dot size [8,11-14], density [7,8,12,15], lateral arrangement [8,9,16], shape [15,17-19], and critical thickness for dot nucleation [14,20,21] observed in many experiments.

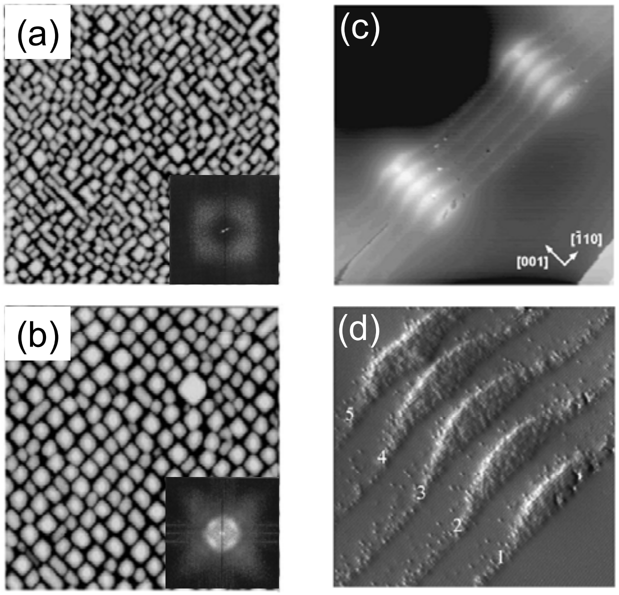

Figure 2 AFM images of surface (a) single layer and (b) 20 period of $Si_{0.25}Ge_{0.75}/Si$ (001) dot superlattice. Adapted from Tersoff *et al.* [7,8]. Cross-sectional scanning tunneling microscopy images of five-stacked of self-assembled 2.4 ML InAs dots separated by 10 nm GaAs spacer layers showing vertically correlation along the growth axis. Adapted from Bruls *et al.* [10]. The scan field is 0.8 × 0.8 μm^2 in (a), 1.25 × 1.25 μm^2 in (b), 150 ×150 nm^2 in (c), and 55 × 55 nm^2 in (d). The height contrast is 5 nm in (a) and 10 nm in (b).

In addition, different interlayer correlations may occur, depending on the details of the interaction mechanisms and growth conditions which mainly relate to elastic lattice deformations around the buried dots due to the dot and substrate lattice mismatch [6,7,11,16], corrugations in surface topography due to incomplete surface planarization [22], and surface segregation or alloy decomposition within the spacer layer [23-25], summarized in Fig. 3, which has been reviewed in Ref. [26] for further reading.

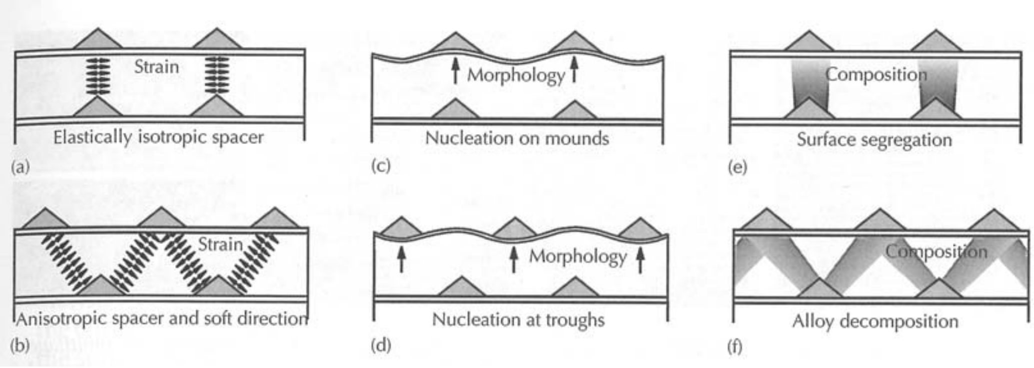

Figure 3 Possible mechanisms for formation of interlayer correlations in self-assembled QD multilayers. Left-hand side: Interlayer correlations caused by the elastic strain fields emerging from subsurface dots and subsequent dot nucleation at the minima of strain on the epilayer surface. Depending on the elastic properties of the spacer layer as well as surface orientation, these minima may be localized (a) above or (b) between the buried dots, which will give rise to either a vertical dot alignment or a staggered dot stacking, respectively. Centre: Interlayer correlation caused by non-planar surface morphologies resulting from incomplete surface planarization during dot overgrowth. Depending on the dominant mechanism of capillary or stress-driven surface mass transport, subsequent dots may nucleate either on top of the mounds (c) or in the troughs in between (d). Right-hand side: Correlated nucleation induced by non-uniformities in the chemical composition of the spacer layer due to (e) surface segregation or (f) alloy decomposition. Adapted from G. Springholz [26].

2.3 Pre-Patterned Substrates

Many attempts to fabricate ordered QDs nucleated on shallow- and deep pre-patterned buffer layers or substrates haven been reported [27-37]. Patterns such as stripes, mesas, trenches, ridges, and holes or other sophisticated structures can be created with a variety of lithographic techniques, e.g. electron-beam lithography, focused ion beam etching [38], or scanning tunneling probe-assisted nanolithography [35]. In general, the kinetics of self-alignment of QDs grown by these technique are governed by the energetically favorable adatom diffusion towards nucleation sites which usually are located at the edges of the mesa patterns or at the bottom of trenches or holes where the thermodynamics and diffusion kinetics of the In atoms are modified during growth by local sub-surface strain fields [39,40]. The extension to vertical QD ordering is generally exploited by using vertical strain coupling of the buried QDs described in section 2.2.

For instance, growth of QD crystals in one-dimensional, two-dimensional, and three-dimensional alignments on patterned GaAs (001) substrates was demonstrated by Kiravittaya *et al.* [41,42]. They prepared the nanometer-scale patterned substrates by standard electron beam lithography and reactive ion etching. The morphology of the QDs grown on a surface patterned with shallow holes was studied as a function of the amount of deposited InAs. They observed that the QDs grown in the patterned holes close to each other formed lateral QD bimolecules for InAs coverages below the commonly observed critical thickness of approximately 1.6 MLs. For increased coverage, the QD bimolecules coalesced to form larger single QDs. The QDs in the holes were then capped with an AlGaAs layer. The buried QD arrays served as a strain template for controlling the site of the QDs in the second layer. By tuning the growth conditions for the second and subsequent layers together with the etched patterns, they achieved one-dimensional, two-dimensional, and three-dimensional QD crystals with a high degree of perfection.

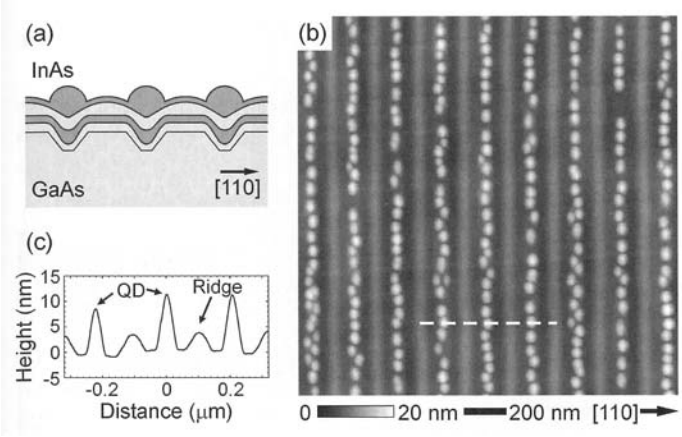

Figure 4 One-dimensional InAs QD crystals on a patterned trench arrays. The pattern periodicity is 210 nm. (a) Schematic of the growth structure. (b) Typical AFM image of the one-dimensional InAs QD crystal. (c) Cross-sectional height profile along the dashed line defined in (b). Adapted from Kiravittaya *et al.* [42].

Figure 4 shows rows of one-dimensional QD crystals aligned along the [1-10] direction as defined by the initially patterned trenches. A 30 MLs GaAs buffer was grown on the patterned trenches. Then, the first InAs QD layer was deposited on the surface and capped with a spacer layer consisting of 8 nm GaAs, 3 nm $Al_{0.5}Ga_{0.5}As$ and 2 nm GaAs. Finally, an InAs layer was again deposited with growth rate of 0.03 ML/s. Self-assembled QDs formed at the bottom of the trenches due to the concave curved surfaces, which lowered the surface chemical potential [43]. Since the trench size was larger than the QD size, some QDs in the rows were slightly misaligned. They observed that the QDs formed in the trenches were partially elongated along the [1-10] direction which might be due to the fact that In atoms preferentially diffused along the trench direction.

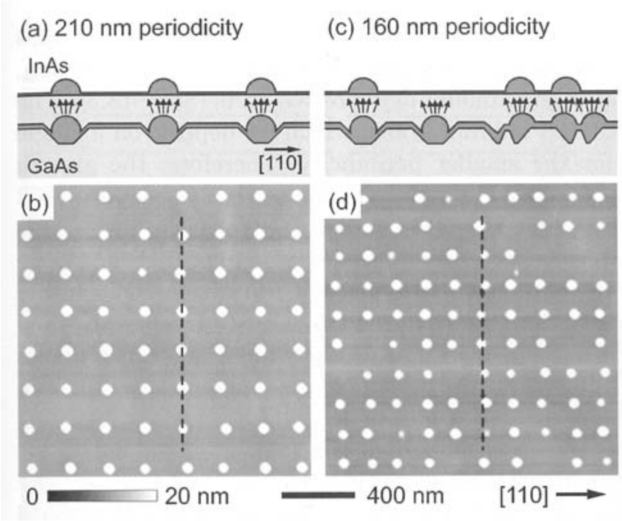

Figure 5 Two-dimensional InAs QD crystal on patterned hole arrays. Pattern periodicities are 210 and 160 nm. For 210 nm periodicity, (a) shows schematic of the growth structure and (b) shows 1.6 × 1.6 μm^2 AFM morphology of surface QDs. For 160 nm periodicity, (c) shows a schematic of the growth structure and (d) shows 1.6 × 1.6 μm^2 AFM morphology of surface QDs. Adapted from S. Kiravittaya *et al.* [42].

Two-dimensional QD crystals grown on hole patterned surfaces with periodicities of 210 nm and 160 nm are shown in Fig. 5. For this sample, 1.5 ML InAs was first deposited followed by a spacer layer consisting of 8 nm GaAs, 4 nm $Al_{0.4}Ga_{0.6}As$ and 3 nm GaAs, and the second InAs QD layer. The QD bimolecule formed along [1-10] for the first layer and the subsequent QDs formed as single QD on all patterned sites. The misalignment of the QD crystals in the 160 nm periodicity substrate was due to the QDs formed in first layer growth as single QDs or QD bimolecules due to the lower average number of Ga and In atoms for the smaller periodicity. Due to the nonoptimized growth on the patterned periodicity of 160 nm, the QDs in the second layer could not occupy all patterned hole sites. Finally the AFM images of the topmost QD layers of the three-dimensional QD crystal grown on the hole patterned surface is shown in Fig. 6. The first QD layer on the patterned holes was capped with a spacer layer consisting of 8 nm GaAs, 4 nm $Al_{0.4}Ga_{0.6}As$ and 3 nm GaAs before the subsequent 1.8 ML InAs QD layer was grown on top. Repetitive growth of the spacer layer and the QD layer resulted in a three-dimensional QD crystal with six InAs QD layers. Ultimately, the three-dimensional QD crystal increases the total volume of active material and allows tuning of the electronic wave functions due to the quantum mechanical coupling across the spacer layers [44]. Based on this approach, it provides a template for future realization of devices based on single QDs, single QD chains or QD crystals.

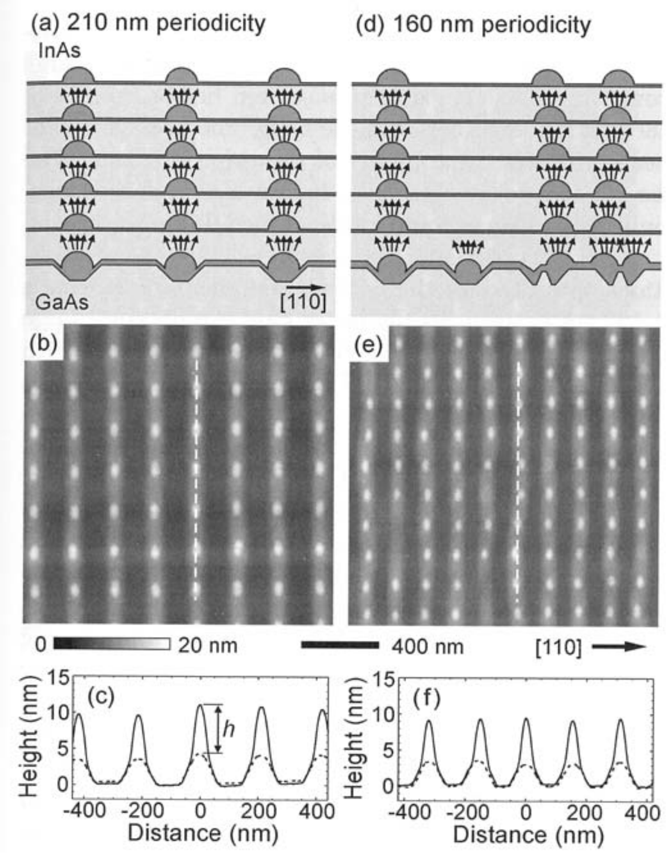

Figure 6 Three-dimensional InAs QD crystal on patterned hole arrays. Pattern periodicities are 210 and 160 nm. For 210 nm periodicity, (a) shows a schematic of the growth structure, (b) shows 1.6 × 1.6 μm^2 AFM image of surface QDs and (c) shows a cross section height profile in (b). For 160 nm periodicity, (d) shows a schematic of the growth structure, (e) shows 1.6 × 1.6 μm^2 AFM image of surface QDs on the sixth layer and (f) shows a cross section height profile in (e). Adapted from S. Kiravittaya *et al.* [42].

2.4 Others Methods

Apart from the techniques mentioned above, other methods have been reported for the fabrication of laterally aligned epitaxial QDs which will be briefly recalled here:

2.4.1 Multiatomic Steps

It has been shown that steps and step bunches may induce preferred sites for island nucleation along the steps, and hence improve the islands spatial ordering and size uniformity [45-51].

Kitamura *et al.* [45] demonstrated the self-alignment of InGaAs QDs by growing the QDs on multiatomic steps by MOVPE. In this technique, first, a GaAs epilayer with multiatomic step (multistep) structures was grown on a vicinal GaAs (001) substrate with 2° misorientation under appropriate growth conditions. Then, the InGaAs QDs were grown selectively on the multistep edges. The schematic illustration of this method is demonstrated in Fig. 7. This growth technique resulted in spontaneously aligned InGaAs QDs without any preprocessing prior to the growth.

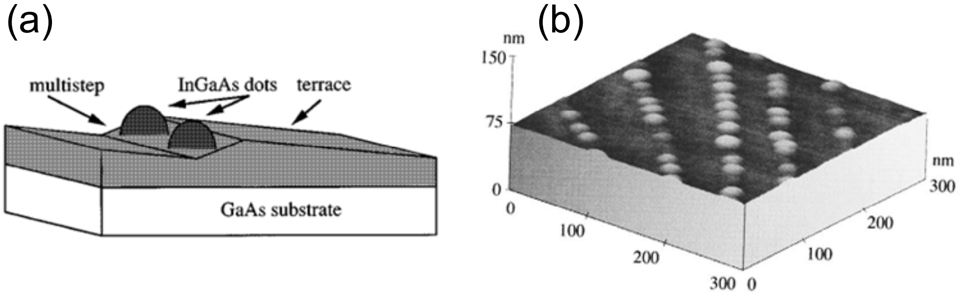

Figure 7 (a) Schematic illustration of InGaAs QDs on the multistep edge of the GaAs epilayer. (b) An AFM image of aligned InGaAs QDs on [010] misoriented surface. The scale is 300 × 300 nm^2. Adapted from Kitamura *et al.* [45].

A very similar approach was carried out by Sakamoto *et al.* [46] who demonstrated arrays of Ge three dimensional islands growth on Si (001) substrates by MBE. Dislocation-free islands, 50 nm in diameter, were aligned along the [0-11] direction on a vicinal Si (001) substrates tilted 4° toward [110]. Surface undulations consisting of (001) and (11x), x = 8-10, facets were self-organized on the Si buffer layer. Ge islands were then preferentially grown on the upper edge of the (001) facets and were arranged in line accordingly, see Fig 8. Nucleation of Ge islands on the surface along atomic-layer step edges and deformation of the near-surface layers on the Si substrate induced by misfit strain were strongly related to the self-alignment of the Ge islands.

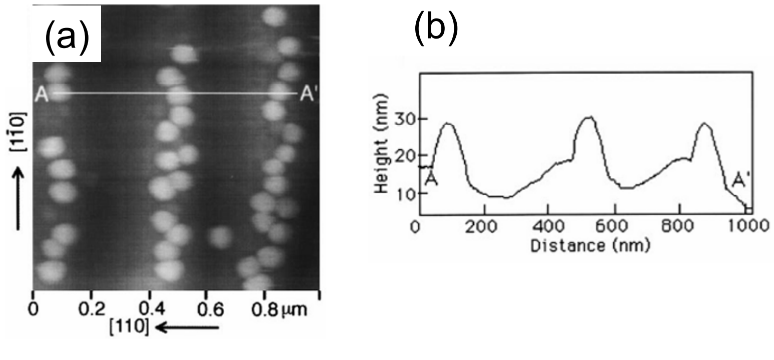

Figure 8 (a) 1 × 1 µm^2 AFM image of 8 ML Ge islands on Si (001) tilted 4° towards [110] aligned to the [1-10] direction. (b) Height profile along the line AA' defined in (a). The substrate surface underneath the islands undulates periodically. Adapted from Sakamoto *et al.* [46].

2.4.2 Cleaved Edge (110) Planes

Another approach that allows the controllable positioning of InAs QDs of well-defined size on (110)-oriented GaAs surfaces was demonstrated by Bauer *et al.* [52]. This concept of QD alignment was based on the method of cleaved edge overgrowth discussed earlier in section 1.5. In general, growth of InAs on the GaAs (110) surface does not lead to dot formation, but rather leads to the relaxation of the lattice mismatch by the formation of misfit dislocations [53]. To overcome this problem they used a new kind of (110)-oriented atomically precise template based on the GaInAlAs material system. It has been reported earlier that InAs islands form on AlAs layers on GaAs (110) substrates [54]. It is well known, that the diffusion of In adatoms on (001) AlAs is much smaller than on (001) GaAs and probably also for (110) AlAs and (110) GaAs [55]. Figure 9 shows the AFM images of InAs islands on AlAs stripes formed by the growth of InAs on GaAs cleavage planes containing thin AlAs layers. They proposed a simple model for the nucleation of InAs on AlAs assuming that the diffusion of In on AlAs was strongly reduced compared to the GaAs regions, which resulted in a net material transport towards the AlAs stripes, leading to an accumulation of InAs on AlAs. Thus, the critical thickness was achieved earlier on AlAs and the nucleation of dots occurred.

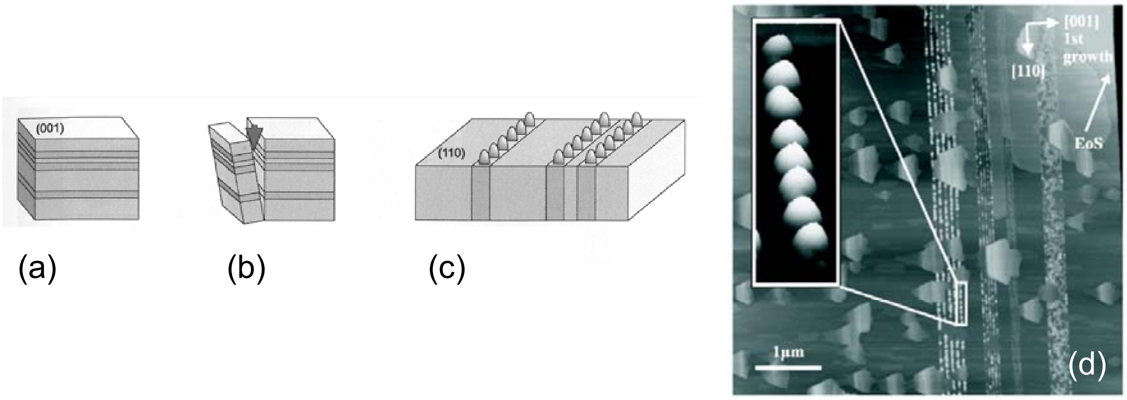

Figure 9 (a)-(c) Schematic of the combination of cleaved edge overgrowth and self-assembly of InAs QDs. (a) Growth of AlAs/GaAs or InGaAs/AlGaAs multilayers on (001) growth axis. (b) The substrate is cleaved in situ in the MBE. (c) Deposition of InAs onto the fresh cleaved (110) surface. Adapted from G. Abstreiter and D. Schuh [56]. The nucleation of InAs on stripes with different strain and composition lead to a one-dimensional alignment of the QDs. (d) AFM image of well-ordered 3.0 ML InAs on AlAs/GaAs multilayers on the cleaved (1-10) surface. The inset shows a close-up of eight perfectly aligned QDs with very similar size and shape. Adapted from J. Bauer [52].

2.5 Self-Organized QD Ordering on High Index Substrates

Nötzel *et al.* presented evidence of the new phenomenon of the direct growth of microstructures by MOVPE on high-index GaAs substrates [57-60]. On GaAs (n11)A substrates one- and zero-dimensional self-faceting due to step bunching occurred, producing wire-like microstructures on GaAs (311)A substrates and dot-like microstructures on GaAs (211)A substrates. The lateral periodicity of self-faceting could be controlled by the layer thickness and growth temperature allowing the width of GaAs/AlGaAs (311)A wire-like heterostructures to be tuned. On GaAs (n11)B substrates, well-ordered QD arrays were formed in a new self-organizing growth mode found in the MOVPE of a sequence of AlGaAs and strained InGaAs QDs buried within AlGaAs microcrystals due to the lateral mass transport, seen in Fig 10.

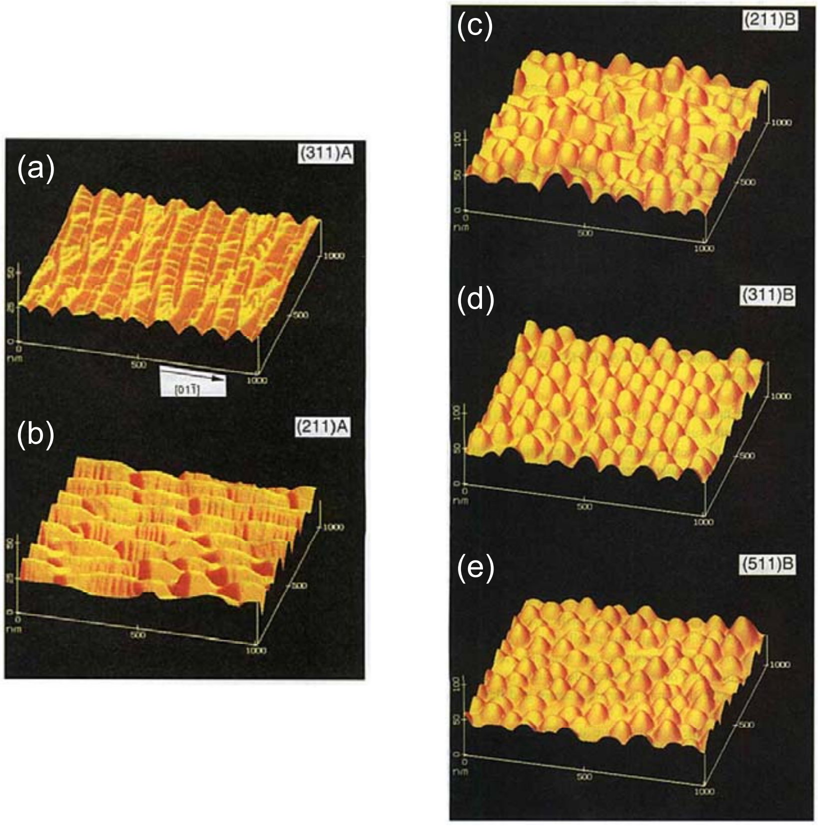

Figure 10 Left-hand side: Three-dimensional AFM images of the 10 nm thick $In_{0.2}Ga_{0.8}As$ layers grown at 800 ˚C over 50 nm thick $Al_{0.5}Ga_{0.5}As$ buffer layers on GaAs (a) (311)A and (b) (211)A substrates. Right-hand side: Three-dimensional AFM images of the AlGaAs microcrystals formed by nominal 3.5 nm thick $In_{0.4}Ga_{0.6}As$ layers grown at 720 ˚C over 100 nm thick $Al_{0.5}Ga_{0.5}As$ buffer layers on GaAs (c) (211)B, (d) (311)B, and (e) (511)B substrates. Adapted from R. Nötzel *et al.* [60].

Ordering of the nanocrystals in this system had been attributed to strain-induced breaking-up of the InGaAs layer together with the appearance of the crystal facets of the AlGaAs nanocrystals selecting distinct directions for surface migration during the formation of the buried InGaAs QD structure. The uniformity in size and shape and the positional alignment of the microcrystals are optimum in the case of the GaAs (311)B substrates, see Fig. 11. This could be connected to its nominal composition of equal units of the singular (100) and (111) planes that might provide the highest degree of anisotropy in the growth process, e.g. for surface migration or atomic arrangement, that was assumed to be an important prerequisite for such ordering phenomena. The size and distance of the disks could be controlled independently by the In composition and the InGaAs layer thickness. For increased In compostion, the size of the nanocrystals was continuously reduced in the mesoscopic size range between several 100 and 10 nm due to smaller InGaAs island size at higher strain. For increased InGaAs layer thickness, the spacing of the AlGaAs nanocrystals and InGaAs disks was decreased, while the average base width and height remained unaffected. Similar structures were also formed on InP (311)B substrates in the InGaAs/AlInAs and InGaAs/InP material systems [61].

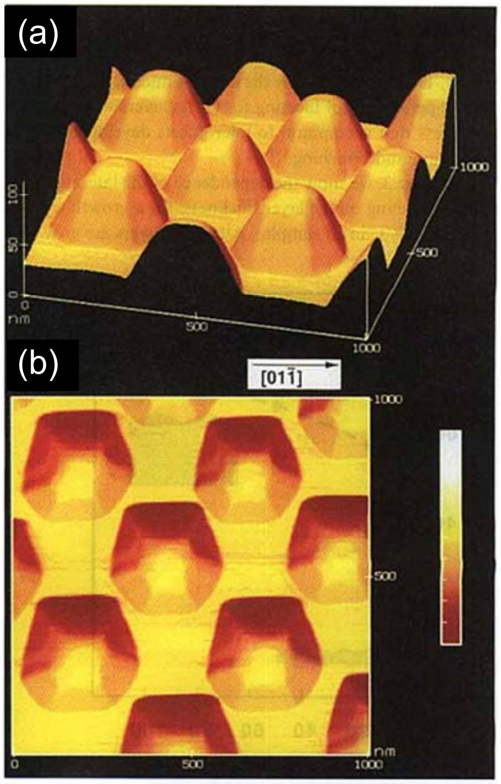

Figure 11 (a) Three-dimensional AFM image. (b) Top view of the AlGaAs microcrystals formed by the nominal 10 nm thick $In_{0.2}Ga_{0.8}As$ layer at 800 ˚C on GaAs (311)B substrates. Adapted from R. Nötzel *et al.* [60].

Similar observations of spontaneous lateral alignment of InGaAs self-assembled QDs on GaAs (311)B through the S-K growth mode by GSMBE was reported by Nishi *et al.* [62]. Later, similar results were reproduced by many groups [63-65] and were related to large anisotropic strain and surface diffusion responsible for such kind of ordering [66-68].

2.6 Self-Organized Anisotropic Strain Engineering

The concept of lateral ordering of epitaxial QDs by self-organized anisotropic strain engineering relies on the creation of well-ordered multilayered superlattice templates which self-organize due to the anisotropic strain inside the given materials. The key features of this technique are the thin capping and post-growth annealing providing material desorption to balance the strain accumulation during stacking and the anisotropic materials transport. The main advantages of this technique are the excellent structural and optical properties of the ordered QDs due to the defect-free self-organized growth mechanism.

2.6.1 One-Dimensional Linear QD Arrays on GaAs (100)

Mano *et al.* [69,70] first demonstrated the formation of linear InGaAs QD arrays on GaAs (100) substrates utilizing the concept of self-organized engineering of anisotropic strain in an InGaAs/GaAs superlattice (SL) template by molecular beam epitaxy. During growth of the InGaAs/GaAs SL at elevated temperatures, elongated InGaAs QDs develop into very uniform and long quantum wire arrays along [0-11] with well-defined lateral periodicity. Utilizing this self-organized InGaAs quantum wire arrays as a template for InAs QD growth by local strain recognition generated by underlying structures, single and multiple InAs QD arrays with 140 nm lateral periodicity were demonstrated. The QD arrays exhibited excellent photoluminescence emission up to room temperature with a linewidth that was not increased compared to that at low temperature. The high structural and optical quality of the ordered QD arrays was assigned to the inherent smoothness of the lateral strain field modulations generated on the SL template surfaces on the nanometer length scale.

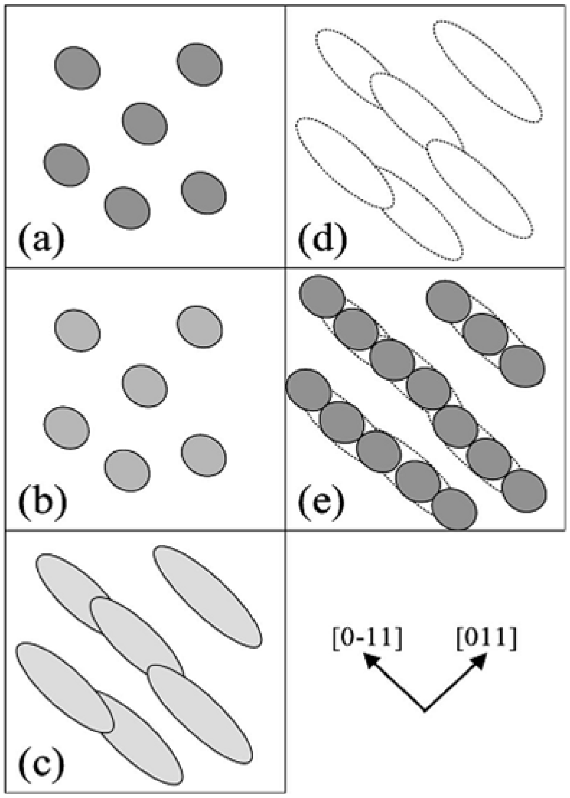

Figure 12 (a)-(e) Schematic illustration of InGaAs quantum wire template formation and QD ordering via self-organized anisotropic strain engineering. (a) Random formation of elongated InGaAs QDs, (b) growth of thin GaAs cap layer, (c) annealing at higher temperature forming QWRs, (d) growth of the GaAs separation layer, and (e) growth of the subsequent InGaAs QD layer [70].

The formation of the uniform SL acting as a template for QD ordering is the key feature of this technique. Figure 12 and the following points summarize the crucial steps for template formation and linear one-dimensional QD ordering on InGaAs/GaAs (100) SL templates.

1. Formation of randomly distributed InGaAs QDs in the S-K growth mode on a GaAs buffer layer.
2. Growth of a thin GaAs capping layer.
3. Annealing at higher temperature. During annealing, the QDs elongate and connect due to preferential anisotropic Ga/In adatom surface migration along [0-11] induced by the (2×4) GaAs surface reconstruction. Simultaneous In desorption allows uniform QD connection due to strain reduction and is balanced by the thin GaAs cap layer. Thus, quantum wires along [0-11] form.
4. Growth of the GaAs separation layer. The thickness is chosen to preserve the lateral strain field modulation from the buried quantum wires at the surface due to vertical strain mediation.

5. Growth of subsequent InGaAs QD layer. The QDs preferentially nucleate above the wire-like nanostructures where the lateral tensile strain field minima reduce the lattice mismatch and induce strain-gradient-driven In adatom surface migration preferentially along [011] towards the minima. Well separated one-dimensional QD arrays along [0-11] form.
6. Repetition of steps (1)-(5) in InGaAs/GaAs SL growth. The length of the quantum wires and QD arrays increases and the lateral ordering improves due to the vertical strain-correlated stacking. Figure 13 shows the AFM images of the InAs QDs grown on the InGaAs/GaAs SL templates with periods from one to 15.

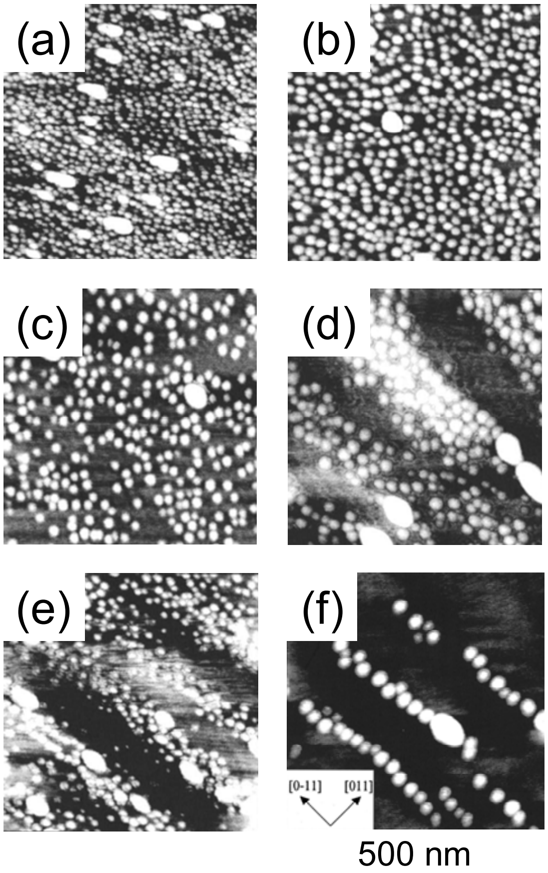

Figure 13 AFM images of the 2.1 ML InAs QDs on (a) GaAs (100) substrates for reference and on the (b) 1, (c) 5, (d) 10, and (e) 15 periods In0.36Ga0.64As 2.6 nm/GaAs 16 nm SL templates. (f) AFM image of the 1.5 ML InAs QD arrays on 15 periods SL template with low growth rate of 0.0007 nm/s. The scan fields are 500 × 500 nm^2 in all images. The height contrast is 7 nm for (a)-(e) and 15 nm for (f). Adapted from T. Mano *et al.* [69].

The relationship of self-organized anisotropic strain engineering with step engineering on shallow mesa-patterned GaAs (100) substrates was established for the realization of advanced, complex QD arrays and networks [71]. Growth on shallow-patterned substrates has been first utilized for the formation of highly uniform sidewall quantum wire and QD arrays on GaAs (311)A [72] as described in the preceding Chapter. On shallow [0-11] and [011] stripe-patterned GaAs (100) substrates the generated type-A and type-B steps differently affect the adatom surface migration processes during SL template formation. While type-A steps along [0-11] have no significant effect on the strain-gradient-driven In adatom migration along [011], type-B steps along [011] strongly suppress the surface-reconstruction-induced Ga/In adatom migration along [0-11] to prevent quantum wire formation and QD ordering, as described in Fig. 14.

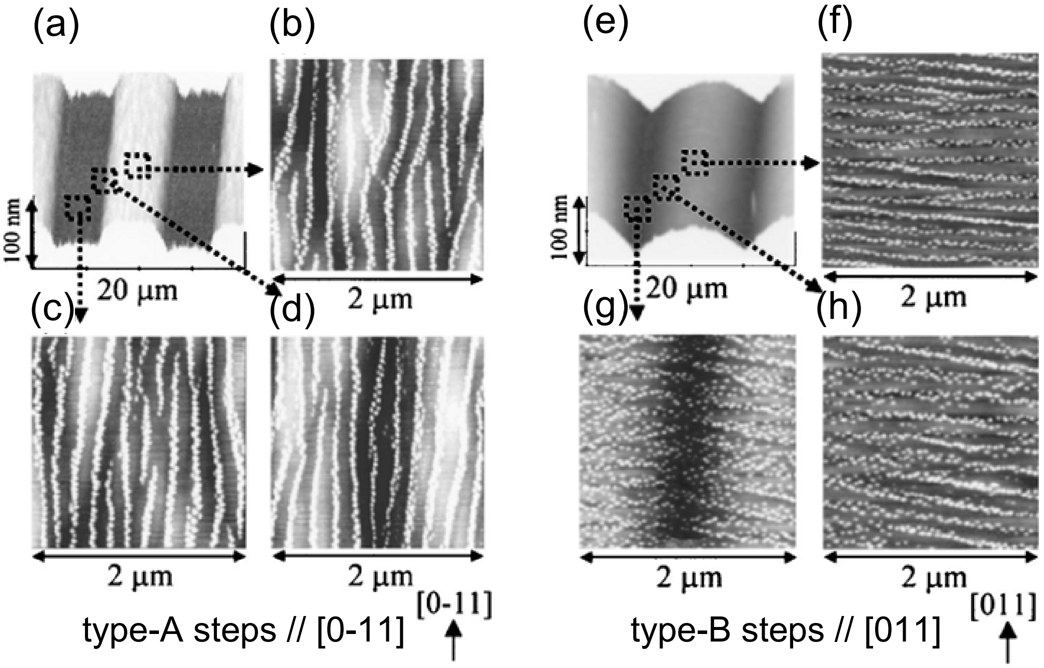

Figure 14 Left-hand side: (a) AFM image of the InGaAs QD arrays on [0-11] stripe-patterned GaAs (100) substrate. (b)-(d) Magnified images of the top, bottom, and slope areas. Right-hand side: (e) AFM image of the InGaAs QD arrays on [011] stripe-patterned GaAs (100) substrate. (f)-(h) Magnified images of the top, bottom, and slope areas. The height contrast is 15 nm for all images. Adapted from T. Mano *et al.* [71].

Further investigations on the formation of ordered QD arrays has been developed on shallow zigzag-patterned substrates with 10 μm wide mesas with 30 nm height and sidewalls alternately rotated by plus and minus 30° off [0-11]. For this shallow mesa height the sidewalls after GaAs buffer layer growth consist of (100) terraces and ML-height type-A and –B steps rather than of facets. The one-dimensional QD arrays on this sidewalls are indeed rotated by plus and minus 16° off [0-11], seen in Fig. 15. The smaller rotation angle of the QD arrays compared to that of the sidewalls indicates that the QD ordering is not directly associated to the formation of QDs along the step-edge direction. In contrast, the QD ordering on the SL template is due to the step-edge induced rotation of the Ga/In adatom migration during annealing in SL template formation while the QD ordering and strain-gradient-driven In adatom migration are solely governed by the strain field and are unaffected by the presence of steps which is evidenced by the comparable lateral periodicity of the QD arrays to that on planar substrates. As demonstrated in Fig. 15, bends of the QD arrays by approximately 32° are formed at the slope intersections, and periodic arrangements of branches are generated at the intersections of the slopes and the planar areas, leading to complex QD arrays and networks which exhibit excellent structural and optical quality.

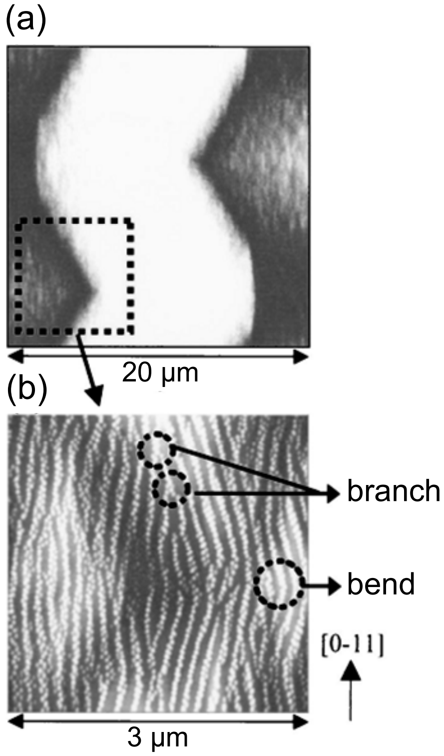

Figure 15 (a) AFM image of the InGaAs QD arrays on zigzag-patterned GaAs (100) substrate. (b) Magnified image of the slope intersections. The height contrast is 40 nm for (a) and 20 nm for (b). Adapted from T. Mano *et al.* [71].

2.6.2 Two-Dimensional Lattice of Ordered QD Molecules on GaAs (311)B

Based on the self-organized anisotropic strain engineering, van Lippen *et al.* [73-75] demonstrated the formation of two-dimensional QD molecules on high-index GaAs (311)B substrates. Figure 16 shows the AFM images of the 3.2-nm-$In_{0.37}Ga_{0.63}As$ layers on the InGaAs/GaAs SL templates with (a) one, (b) five, and (c) ten periods on GaAs (311)B. Each SL period comprises, similar to GaAs (100), InGaAs QDs growth, thin capping, annealing, and growth of a spacer layer. Upon stacking, the nanoscale two-dimensional QD-like InGaAs surface modulation for the first SL period evolves into a distinct mesoscopic mesa-like arrangement when the number of SL period is increased from five to ten. This is attributed to the anisotropic surface migration during annealing, smoothening the mesas to form mesoscopic nodes, and strain correlated stacking, which is governed by preferential InGaAs accumulation on the nodes due to strain-gradient-driven In adatom migration. Finally uniform two-dimensional 0.5 nm InAs QD arrays are formed on top of the 10-period SL template with the thickness of the top spacer layer of 15 nm, shown in Fig. 16 (d).

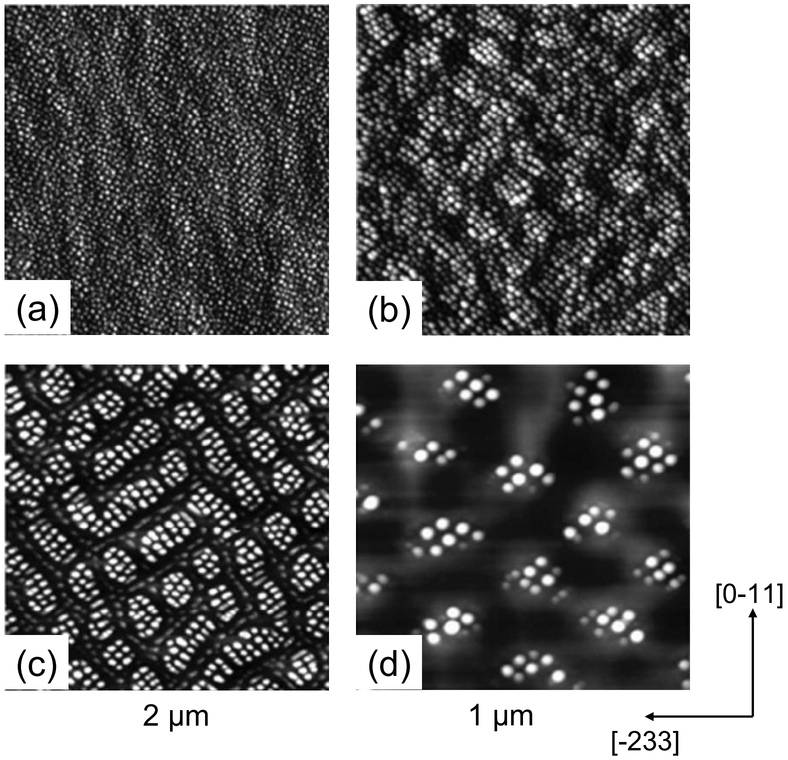

Figure 16 (a)-(c) AFM images of 3.2 nm In0.37Ga0.63As QDs on the (a) 1, (b) 5, and (c) 10 periods In0.37Ga0.63As 3.2 nm/GaAs 6.2 nm SL template. (d) AFM image of 0.5 nm InAs QD molecules grown on the 10-period SL template with 15 nm upper GaAs separation layer. The height contrast is 15 nm for (a)-(c) and 10 nm for (d). Adpated from Lippen *et al.* [73].

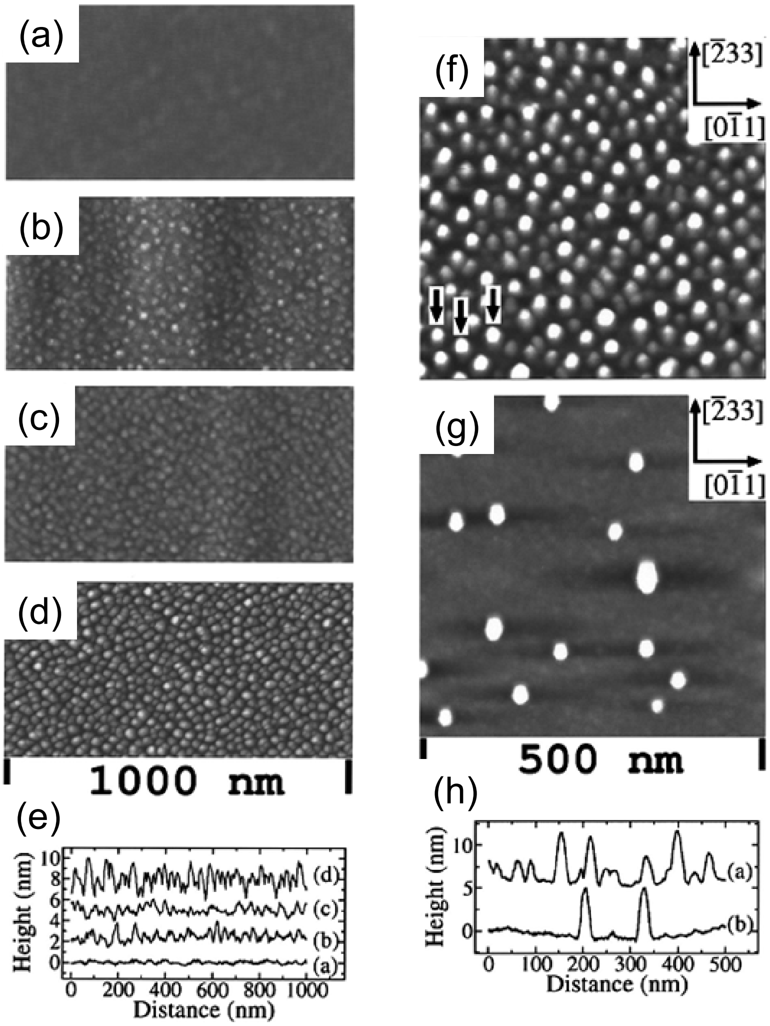

Figure 17 Left-hand side: AFM images of (a) 1.3, (b) 1.5, (c) 1.7, and (d) 2.1 nm thick In$_{0.35}$Ga$_{0.65}$As deposited on GaAs (311)B substrates. (e) The surface profile scans along [0-11] for (a)-(d). Right-hand side: AFM images of the QDs formed at low growth rate by (f) 0.23 nm thick InAs on a 1.4 nm In$_{0.35}$Ga$_{0.65}$As template and (g) by 0.46 nm InAs directly on GaAs (311)B substrates. (h) The surface profile scans along [0-11] for (f) and (g). The height contrast is 5 nm in all images. Adapted from Q. Gong *et al.* [76].

The formation of the nanoscale two-dimensional surface modulations for this In composition (In$_{0.37}$Ga$_{0.63}$As/GaAs for the SL template) is mainly due to strain driven growth instability rather than nucleation of QDs in the S-K mode which occurs for higher In composition. Growth instability is characterized by nucleation-free evolution of surface modulations with the periodicity mainly given by the lattice match. During growth the undulation height continuously increases while its periodicity is kept constant, as demonstrated in Fig. 17. On the contrary, the S-K growth mode involves the formation of a two-dimensional wetting layer followed by random island nucleation, where the island height increases and saturates very abruptly and further growth mainly increases the island density. Growth instability of thin alloy films has been theoretically studied [77] and experimentally verified [78,79] in the epitaxy of strained $Si_{1-x}Ge_x$ on Si (100). Recently growth instability of strained InGaAs producing an undulated surface with nanometer-scale wire-like structures on GaAs (311)A substrates has been reported [80]. QD nucleation then occurs preferentially on top of the wires but is random along their length. On GaAs (311)B, the undulation of the surface morphology is two dimensional, in the form of matrix of closely packed cells [76]. Due to the well defined nature of evolution with constant periodicity, the related two-dimensional strain modulation generates a uniform template for full control of the nucleation of InAs QDs.

When InAs is grown on top of the 10-period SL template following a GaAs spacer layer, well-separated, ordered QDs preferentially form in dense groups or molecules, see Fig. 16 (d), on top of the nodes due to local strain field recognition where the underlying InGaAs accumulation establishes the tensile strain field minima and related strain-gradient-driven In adatom migration for strain-correlated stacking. The QD number, size, and ordering can be controlled by the GaAs spacer layer thickness, InAs amount, and growth temperature.

Single InAs QDs on the SL template nodes are further realized at elevated growth and annealing temperatures of the 10-period SL template and InAs QDs when an additional InAs QD layer is inserted with thicker GaAs top spacer layer. Due to the fact that the InAs QDs in this interlayer solely form on the SL template nodes, the lateral strain field modulation most effectively concentrates after thin GaAs capping and annealing. Together with enhanced In adatom migration length at elevated temperature and QD coalescence, the resulting shrinkage of the effective area of the tensile strain field minima for preferred QD formation produces single InAs QDs in the center of the nodes.

Recently, Selçuk *et al.* [81,82] demonstrated the formation of complex laterally ordered architectures of connected InGaAs QD arrays and isolated InAs QD groups by combining self-organized anisotropic strain engineering with step engineering on shallow- and deep-patterned GaAs (311)B substrates. The combination of strain and step engineering on shallow stripe-patterned substrates transforms the periodic spotlike arrangement of the InGaAs QD arrays and InAs QD groups (on planar substrates) into a zigzag arrangement of periodic stripes which are well ordered over macroscopic areas on zigzag mesa-patterned substrates, shown in Fig 18. For such shallow patterns (30 nm), the surface consists of terraces and monolayer high steps after buffer layer growth rather than of facets which form for deep-etched mesas. Hence, the formation of the zigzag arrangement is attributed to the presence of steps on the non-equivalent mesa sidewalls. In contrast, the formation of slow-growing facets on deep-patterned substrates produces QD-free mesa sidewalls, while InGaAs QD arrays and InAs QD groups form on the GaAs (311)B top and bottom planes with the arrangement modified only close to the sidewalls developing single-QD stripes along the edges of the mesa top depending on the sidewall orientation [81]. Hence, while shallow patterns allow modifications of the QD ordering within large areas, the deep patterns allow local modifications, revealing the complementary nature of both approaches for formation of complex QD arrays.

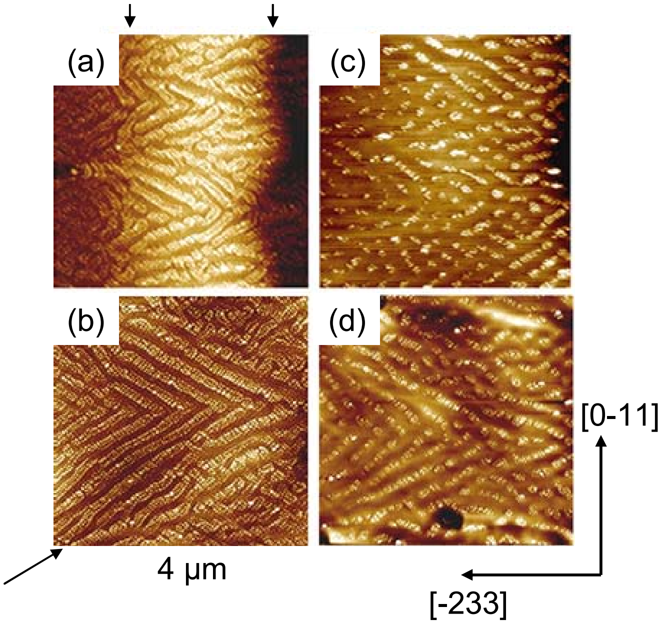

Figure 18 AFM images of the [(a) and (b)] 3.3 nm thick $In_{0.45}Ga_{0.55}As$ QD arrays and [(c) and (d)] 0.6 nm thick InAs QD groups on 3.3 nm $In_{0.45}Ga_{0.55}As$/ 5.5 nm GaAs SL template grown on shallow-patterned GaAs (100) substrates: [(a) and (c)] periodic stripe with 2 µm stripe width and [(b) and (d)] zigzag with acute angle (mesa bottom) of 60˚ pointing toward [2-3-3]. The arrows in (a) and (b) are the guide for the eye along the mesa patterns. The height contrast is 30 nm in all images. Adapted from E. Selçuk *et al.* [81].

2.7 Summary

In conclusion, various techniques for the lateral positioning of epitaxial QDs have been summarized in this chapter. The basic idea of utilizing strained multilayers for lateral and vertical alignment of three-dimensional QD crystals have been described which, however, lead to material fluctuations and unavoidable photoluminescence broadening. Pre-patterning of substrates prior to the QDs growth has effectively proven to align the QDs on the long-range length scales, however, the optical properties of such QDs suffer from imperfections of the lithographic and etching processes. Evidently, this results in low PL efficiency in particular at RT and large PL linewidth broadening of single QD spectroscopy over a few hundreds µeV due to the charge traps at the pattern interface [83,84]. Positioning of QDs by other methods like multiatomic step bunching or cleaved edge overgrowth are not very suited for device processing due to the complexities of the fabrication methods.

A solution for these obstacles is to use the concept of self-organization QD growth and anisotropic strain engineering described in the second half of this chapter. This self-organization of ordered QDs formed on strained SL templates is inherently defect-free and thus provides excellent structural and optical properties. The linear one-dimensional and two-dimensional square lattices of QDs are produced on SL templates on GaAs (100) and (311)B substrates due to asymmetric surface migration. Further combination with step engineering on shallow- and deep-patterned substrates modifies the orientation of the arrays giving more degrees of freedoms to realize complex QD arrays and networks. This, ultimately, will provide the building blocks for future quantum functional devices [85]. The concept of self-organized anisotropic strain engineering of SL templates constitutes the basis of the following chapters presented in this thesis where the general principle will be transferred from the GaAs-based to the InP-based system to access QD emission in the important 1.55-µm telecom wavelength region.

Bibliography

[1] T. F. Krauss, R. M. De La Rue, and S. Brand, *Nature* **383**, 699 (1996).

[2] H. Heidemeyer, U. Denker, C. Müller, and O. G. Schmidt, *Phys. Rev. Lett.* **91**, 196103 (2003).

[3] T. Takagahara, *Surf. Sci.* **267**, 310 (1992).

[4] I. D'Amico and B. W. Lovett, in *Handbook of Self Assembled Semiconductor Nanostructures for Novel Devices in Photonics and Electronics*, edited by M. Henini (Elsevier, 2008), p. 687.

[5] R. Hanson, L. P. Kouwenhoven, J. R. Petta, S. Tarucha, and L. M. K. Vandersypen, *Rev. Mod. Phys.* **79**, 1217 (2007).

[6] Q. Xie, A. Madhukar, P. Chen, and N. P. Kobayashi, *Phys. Rev. Lett.* **75**, 2542 (1995).

[7] J. Tersoff, C. Teichert, and M. G. Lagally, *Phys. Rev. Lett.* **76**, 1675 (1996).

[8] C. Teichert, M. G. Lagally, L. J. Peticolas, J. C. Bean, and J. Tersoff, *Phys. Rev. B* **53**, 16334 (1996).

[9] G. S. Solomon, S. Komarov, and J. S. Harris Jr., *J. Crystal Growth* **201-202**, 1990 (1999).

[10] D. M. Bruls, P. M. Koenraad, H. W. M. Salemink, J. H. Wolter, M. Hopkinson, and M. S. Skolnick, *Appl. Phys. Lett.* **82**, 3758 (2003).

[11] F. Liu, S. E. Davenport, H. M. Evans, and M. G. Lagally, *Phys. Rev. Lett.* **82**, 2528 (1999).

[12] G. S. Solomon, S. Komarov, J. S. Harris, and Y. Yamamoto, *J. Crystal Growth* **175-176**, 707 (1997).

[13] H. Eisele, O. Flebbe, T. Kalka, C. Preinesberger, F. Heinrichsdorff, A. Krost, D. Bimberg, and M. Dähne-Prietsch, *Appl. Phys. Lett.* **75**, 106 (1999).

[14] V. L. Thanh, V. Yam, P. Boucaud, F. Fortuna, C. Ulysse, D. Bouchier, L. Vervoort, and J.-M. Lourtioz, *Phys. Rev. B* **60**, 5851 (1999).

[15] A. Raab, R. T. Lechner, and G. Springholz, *Appl. Phys. Lett.* **80**, 1273 (2002).

[16] G. Springholz, V. Holy, M. Pinczolits, and G. Bauer, *Science* **282**, 734 (1998).

[17] W. Wu, J. R. Tucker, G. S. Solomon, and J. S. Harris Jr., *Appl. Phys. Lett.* **71**, 1083 (1997).

[18] O. Flebbe, H. Eisele, T. Kalka, F. Heinrichsdorff, A. Krost, D. Bimberg, and M. Dähne-Prietsch, *J. Vac. Sci. Technol. B.* **17** (4), 1639 (1999).

[19] D. M. Bruls, J. W. A. M. Vugs, P. M. Koenraad, M. Hopkinson, M. S. Skolnick, F. Long, and S. P. A. Gill, *Appl. Phys. Lett.* **81**, 1708 (2002).

[20] Y. Nakata, Y. Sugimaya, T. Fuatsugi, and N. Yokoyama, *J. Crystal Growth* **175-176**, 713 (1997).

[21] O. G. Schmidt, O. Kienzle, Y. Hao, K. Eberl, and F. Ernst, *Appl. Phys. Lett.* **74**, 1272 (1999).

[22] P. Sutter, E. Mateeva-Sutter, and L. Vescan, *Appl. Phys. Lett.* **78**, 1736 (2001).

[23] Z. Sun, S. F. Yoon, J. Wu, and Z. G. Wang, *J. Appl. Phys.* **91**, 6021 (2004).

[24] J. Brault, M. Gendry, O. Marty, M. Pitaval, J. Olivares, G. Grenet, and G. Hollinger, *Appl. Surface. Sci.* **162-163**, 584 (2000).

[25] C. Priester and G. Grenet, *Phys. Rev. B* **64**, 125312 (2001).

[26] G. Springholz, in *Handbook of Self Assembled Semiconductor Nanostructures for Novel Devices in Photonics and Electronics*, edited by M. Henini (Elsevier, 2008), p. 1.
[27] D. S. L. Mui, D. Leonard, L. A. Coldren, and P. M. Petroff, *Appl. Phys. Lett.* **66**, 1620 (1995).
[28] W. Seifert, N. Carlsson, A. Petersson, L. -E. Wernersson, and L. Samuelson, *Appl. Phys. Lett.* **68**, 1684 (1996).
[29] S. Jepperson, M. S. Miller, D. Hessman, B. Kowalski, I. Maximov, and L. Samuelson, *Appl. Phys. Lett.* **68**, 2228 (1996).
[30] A. Hartmann, L. Loubies, F. Reinhardt, and E. Kapon, *Appl. Phys. Lett.* **71**, 1314 (1997).
[31] T. I. Kamins and R. S. Williams, *Appl. Phys. Lett.* **71**, 1201 (1997).
[32] A. Konkar, A. Madhukar, and P. Chen, *Appl. Phys. Lett.* **72**, 220 (1998).
[33] H. Lee, J. A. Johnson, J. S. Speck, and P. M. Petroff, *J. Vac. Sci. Technol. B* **18**, 2193 (2000).
[34] O. G. Schmidt, N. Y. Jin-Phillipp, C. Lange, U. Denker, K. Eberl, R. Schreiner, H. Gräbeldinger, and H. Schweizer, *Appl. Phys. Lett.* **77**, 4139 (2000).
[35] S. Kohmoto, H. Nakamura, S. Nishikawa, and K. Asakawa, *J. Vac. Sci. Technol. B* **20**, 762 (2002).
[36] Y. Nakamura, O. G. Schmidt, N. Y. Jin-Phillipp, S. Kiravittaya, C. Müller, K. Eberl, H. Gräbeldinger, and H. Schweizer, *J. Crystal Growth* **242**, 339 (2002).
[37] S. C. Lee, A. Stintz, and S. R. J. Brueck, *J. Appl. Phys.* **91**, 3282 (2002).
[38] A. Portavoce, R. Hull, M. C. Reuter, and F. M. Ross, *Phys. Rev. B* **76**, 235301 (2007).
[39] Z. Zhong, A. Halilovic, M. Mühlberger, F. Schäffler, and G. Bauer, *Appl. Phys. Lett.* **82**, 445 (2003).
[40] Z. Zhong, A. Halilovic, M. Mühlberger, F. Schäffler, and G. Bauer, *J. Appl. Phys.* **93**, 6258 (2003).
[41] S. Kiravittaya, H. Heidemeyer, and O. G. Schmidt, *Physica E* **23**, 253 (2004).
[42] S. Kiravittaya, H. Heidemeyer, and O. G. Schmidt, in *Lateral Alignment of Epitaxial Quantum Dots*, edited by O. G. Schmidt (Springer, Berlin Heidelberg New York, 2007), p. 489.
[43] D. J. Srolovitz, *Acta. Metall.* **37**, 621 (1989).
[44] G. Ortner, M. Bayer, A. Larionov, V. B. Timofeev, A. Forchel, Y. B. Lyanda-Geller, T. L. Reinecke, P. Hawrylak, S. Fafard, and Z.Wasilewski, *Phys. Rev. Lett.* **90**, 086404 (2003).
[45] M. Kitamura, M. Nishioka, J. Oshinowo, and Y. Arakawa, *Appl. Phys. Lett.* **66**, 3663 (1995).
[46] K. Sakamoto, H. Matsuhata, M. O. Tanner, D. Wang, and K. L. wang, *Thin Solid Films* **321**, 55 (1998).
[47] D. Martrou, P. Gentile, and N. Magnea, *J. Crystal Growth* **201/202**, 101 (1999).
[48] A. Li, F. Liu, D. Y. Petrovykh, J. -L. Lin, J. Viernow, F. J. Himpsel, and M. G. Lagally, *Phys. Rev. Lett.* **85**, 5380 (2000).
[49] F. Poser, A. Bhattacharya, S. Weeke, and W. Richter, *J. Crystal Growth* **248**, 317 (2003).

[50] A. Sgarlata, P. D. Szkutnik, A. Balzarotti, N. Motta, and F. Rosei, *Appl. Phys. Lett.* **83**, 4002 (2003).

[51] K. Brunner, *Rep. Prog. Phys.* **65**, 27 (2002).

[52] J. Bauer, D. Schuh, E. Uccelli, R. Schulz, A. Kress, F. Hofbauer, J. J. Finley, and G. Abstreiter, *Appl. Phys. Lett.* **85**, 4750 (2004).

[53] J. G. Belk, D. W. Pashley, C. F. McConville, J. L. Sudijono†, B. A. Joyce, and T. S. Jones, *Phys. Rev. B* **56**, 10289 (1997).

[54] D. Wasserman, S. A. Lyon, M. Hadjipanayi, A. Maciel, and J. F. Ryan, *Appl. Phys. Lett.* **83**, 5050 (2003).

[55] P. Ballet, J. B. Smathers, H. Yang, C. L. Workman, and G. J. Salamo, *J. Appl. Phys.* **90**, 481 (2001).

[56] G. Abstreiter and D. Schuh, in *Lateral Alignment of Epitaxial Quantum Dots*, edited by O. G. Schmidt (Springer, Berlin Heidelberg New York, 2007), p. 237.

[57] R. Nötzel, J. Temmyo, and T. Tamamura, *Nature* **369**, 131 (1994).

[58] R. Nötzel, J. Temmyo, and T. Tamamura, *Appl. Phys. Lett.* **64**, 3557 (1994).

[59] R. Nötzel, J. Temmyo, and T. Tamamura, *Appl. Phys. Lett.* **65**, 2854 (1994).

[60] R. Nötzel, T. Fukui, H. Hasegawa, J. Temmyo, A. Kozen, and T. Tamamura, *Chem. Vap. Deposition* **1**, 81 (1995).

[61] Richard Nötzel, Jiro Temmyo, Atsuo Kozen, Toshiaki Tamamura, Takashi Fukui, and Hideki Hasegawa, *Appl. Phys. Lett.* **66**, 2525 (1995).

[62] Kenichi Nishi, Takayoshi Anan, Akiko Gomyo, Shigeru Kohmoto, and Shigeo Sugou, *Appl. Phys. Lett.* **70**, 3579 (1997).

[63] M. Kawabe, Y.J. Chun, S. Nakajima, and K. Akahane, *Jpn. J. Appl. Phys.* **36**, 4078 (1997).

[64] K. Akahane, T. Kawamura, K. Okino, H. Koyama, S. Lan, Y. Okada, and M. Kawabe, *Appl. Phys. Lett.* **73**, 3411 (1998).

[65] Zh. M. Wang, Sh. Seydmohamadi, J. H. Lee, and G. J. Salamo, *Appl. Phys. Lett.* **85**, 5031 (2004).

[66] Kouichi Akahane, Huaizhe Xu, Yoshitaka Okada, and Mitsuo Kawabe, *Physica E* **11**, 94 (2001).

[67] M. Schmidbauer, Sh. Seydmohamadi, D. Grigoriev, Zh.M. Wang, Yu. I. Mazur, P. Schäfer, M. Hanke, R. Köhler, and G. J. Salamo, *Phys. Rev. Lett.* **66**, 066108 (2006).

[68] P. M. Lytvyn, V. V. Strelchuk, O. F. Kolomys, I. V. Prokopenko, M. Ya. Valakh, Yu. I. Mazur, Zh. M. Wang, G. J. Salamo, and M. Hanke, *Appl. Phys. Lett.* **91**, 173118 (2007).

[69] T. Mano, R. Nötzel, G. J. Hamhuis, T. J. Eijkemans, and J. H. Wolter, *Appl. Phys. Lett.* **81**, 1705 (2002).

[70] T. Mano, R. Nötzel, G. J. Hamhuis, T. J. Eijkemans, and J. H. Wolter, *J. Appl. Phys.* **95**, 109 (2004).

[71] T. Mano, R. Nötzel, D. Zhou, G. J. Hamhuis, T. J. Eijkemans, and J. H. Wolter, *J. Appl. Phys.* **97**, 014304 (2005).

[72] R. Nötzel, Z. C. Niu, M. Ramsteiner, H.-P. Schönherr, L. Däweritz, and K. H. Ploog, *Nature (London)* **392**, 56 (1998).

[73] T. v. Lippen, R. Nötzel, G. J. Hamhuis, and J. H. Wolter, *Appl. Phys. Lett.* **85**, 118 (2004).

[74] T. van Lippen, R. Nötzel, G. J. Hamhuis, and J. H. Wolter, *J. Appl. Phys.* **97**, 044301 (2005).
[75] T. van Lippen, R. Nötzel, and J. H. Wolter, *J. Vac. Sci. Technol. B* **23**, 1693 (2005).
[76] Q. Gong, R. Nötzel, G. J. Hamhuis, T. J. Eijkemans, and J. H. Wolter, *Appl. Phys. Lett.* **81**, 3254 (2002).
[77] J. E. Guyer and P. W. Voorhees, *Phys. Rev. Lett.* **74**, 4031 (1995).
[78] R. M. Tromp, F. M. Ross, and M. C. Reuter, *Phys. Rev. Lett.* **84**, 4641 (2000).
[79] P. Sutter and M. G. Lagally, *Phys. Rev. Lett.* **84**, 4637 (2000).
[80] Q. Gong, R. Nötzel, J. H. Wolter, H. -P. Schönherr, and K. H. Ploog, *J. Crystal Growth* **242**, 104 (2002).
[81] E. Selçuk, G. J. Hamhuis, and R. Nötzel, *J. Appl. Phys.* **102**, 094301 (2007).
[82] E. Selçuk, A. Yu. Silov, and R. Nötzel, *Appl. Phys. Lett.* **94**, 263108 (2009).
[83] P. Atkinson, S. Kiravittaya, M. Benyoucef, A. Rastelli, and O. G. Schmidt, *Appl. Phys. Lett.* **93**, 101908 (2008).
[84] C. Schneider, A. Huggenberger, T. Sünner, T. Heindel, M. Strauß, S. Göpfert, P. Weinmann, S. Reitzenstein, L. Worschech, M. Kamp, S. Höfling, and A. Forchel, *Nanotechnology* **20**, 434012 (2009).
[85] R. Nötzel, T. Mano, Q. Gong, and J. H. Wolter, *Proc. of IEEE* **91**, 1893 (2003).

CHAPTER 3

Formation of InAs Quantum Dots and Dashes Induced by the Buffer Layer Surface Morphology

ABSTRACT

The surface morphology of the buffer layer is identified as the key parameter for the formation of InAs quantum dots (QDs) or dashes (QDashes) by chemical beam epitaxy (CBE) on lattice-matched InGaAsP on InP (100) substrates. Growth conditions leading to the formation of QDashes are always accompanied by a rough buffer layer morphology. Although other growth parameters such as higher growth temperature, larger As flux, and compressive buffer layer strain favor the formation of QDs, once, the buffer layer has a rough morphology, QDashes are formed during InAs growth. On smooth buffer layers we always find well-shaped and symmetric QDs. Hence, we conclude that not the growth conditions during InAs deposition, but rather the related surface morphology of the buffer layer determines the formation of QDs or QDashes, which exhibit both high optical quality.[1]

---

[1] These results have been published as: *Surface morphology induced InAs quantum dot or dash formation on InGaAsP/InP (100)*, N. Sritirawisarn, F. W. M. van Otten, T. J. Eijkemans, and R. Nötzel, J. Crystal Growth **305**, 63 (2007).

3.1 Introduction

Self-assembled semiconductor quantum dots (QDs) are potentially important for a wide-range of applications spanning from nanophotonics, nanoelectronics to quantum information processing. As described in previous chapters, owing to their atomic-like discrete energy-states, QD active regions significantly improve the performance like transparency current density, threshold current, and gain of optical devices such as lasers and semiconductor optical amplifiers (SOAs). Being compatible with the global information and communication infrastructure demands device operation in the 1.55-µm wavelength region, which is the minimum absorption window of glass fibers. The InAs/InP materials system ideally covers this wavelength region since InAs/GaAs QDs, which are most widely studied, strongly degrade for emission wavelengths larger than 1.3 µm. Unfortunately, the low (3.2 %) lattice mismatch between InAs and InP and the strong As/P exchange reaction during InAs deposition impose severe difficulties to reproducibly control InAs/InP QD formation and emission wavelength and, moreover, often lead to a wide variety of unwanted nanostructures besides QDs, such as quantum dashes (QDashes) and quantum wires (QWires). QDashes or quantum sticks (QSticks) are elongated QDs with typically a few hundreds of nm length, shallow height, and width comparable to the size of QDs. This type of structure is typically observed in the self-assembled InAs/InP nanostructures system and controversially discussed in the literatures. For applications, the understanding and control of the relevant processes leading to such unwanted nanostructures is essential to guarantee the reproducible formation of InAs/InP QDs with well-defined emission wavelengths.

In this chapter, we identify the significance of the morphology of the buffer layer as a key parameter determining the formation of InAs QDs or QDashes on InGaAsP/InP (100). Growth conditions leading to the formation of QDashes are always accompanied by rough buffer layer morphology. Although by adjusting growth parameters, e.g. higher growth temperature, larger As flux, and compressive layer strain do favor the formation of QDs, once, the buffer layer is rough, QDash formation cannot be avoided. On smooth buffer layers, for the same InAs growth conditions, we reproducibly find well-shaped, symmetric InAs QDs. Hence, not the growth conditions during InAs deposition but rather the related surface morphology of the buffer layer governs the formation of InAs QDs or QDashes, which both exhibiting high optical quality.

The general information on InAs/InP QDash structures for different growth parameters is firstly provided in section 3.2. Section 3.3 discusses the As/P exchange reaction during InAs/InP nanostructure growth. The details of the experiments and characterization techniques are described in section 3.4. In section 3.5, a systematic discussion of the results based on the dependence on the different growth parameters is given. The chapter is summarized in section 3.6.

3.2 InAs/InP Quantum Dashes

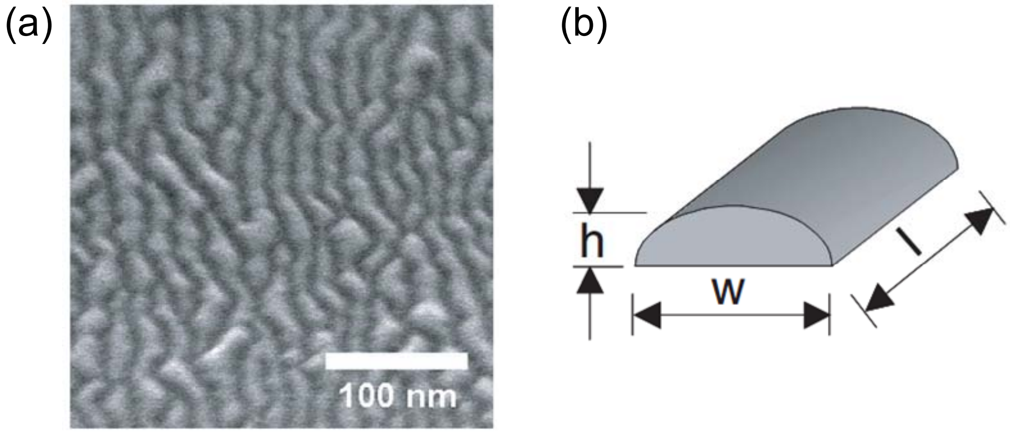

Figure 1 (a) Scanning electron microscope (SEM) image top view of an uncapped InAs QDashes with 5.0 MLs InAs grown on InGaAlAs buffer layer lattice-matched to InP (100) substrate. (b) Schematic illustration with three major geometrical parameters height (h), width (w) and length (l). Adapted from J. P. Reithmaier *et al.* [1].

In general, the QDash material consists of elongated, self-assembled nanostructures treated as quasi-QD structure with similar width and height compared to typical QDs while the length is extended to several 100 nm. For the formation of dash-like islands, Stranski-Krastanow (S-K) grown InAs is deposited on InP (100) with lattice matched buffer layers, like InGaAs, InAlGaAs or InGaAsP. Due to the reduced lattice mismatch between InAs and InP, the island size is slightly larger than for GaAs based QDs. Typical lateral dimensions are 20-30 nm in one direction and 20 to several 100 nm in the other direction, preferentially oriented along [0-11] [1]. The height in the growth direction is of the order of 5 – 10 nm. A close look at the top-view scanning electron microscope (SEM) image in Fig. 1 reveals that the nanostructures resemble a dense assembly of QWRs. However, there are many structural irregularities suggesting the possibility of carrier localizations leading to QD-like behavior. Figure 2 shows the cross-sectional scanning tunneling microscope (X-STM) image of buried InAs QDashes. The structures are clearly elongated along the [-110] direction with average lateral size of 15 nm along the [110] direction and about 60 nm along the [-110] direction. Their height along the growth direction is about 2 nm [2]. The elongation of the QDashes along the [0-11] direction is believed to be related to the InP P-stabilized (2×4) surface reconstruction with missing P dimer rows along [0-11] leading to longer diffusion length along the [0-11] direction [3,4]. It has been further proposed that the dash-like structures are elongated along the [0-11] direction as an effective way to relax the intrinsic strain asymmetry in <110> directions built-in at the InAs/InP interface under group-III element stabilized growth conditions [5]. Theoretical investigations of carrier confinement in InAs QDashes have been performed [6]. Dery et al. demonstrates theoretical gain model of QWR optical amplifier which agrees well to the experimental data extracted from QDash structure suggesting that the InAs/InP QDash material have QWR-like characteristics despite of the strong potential perturbation along elongated dash axis [7].

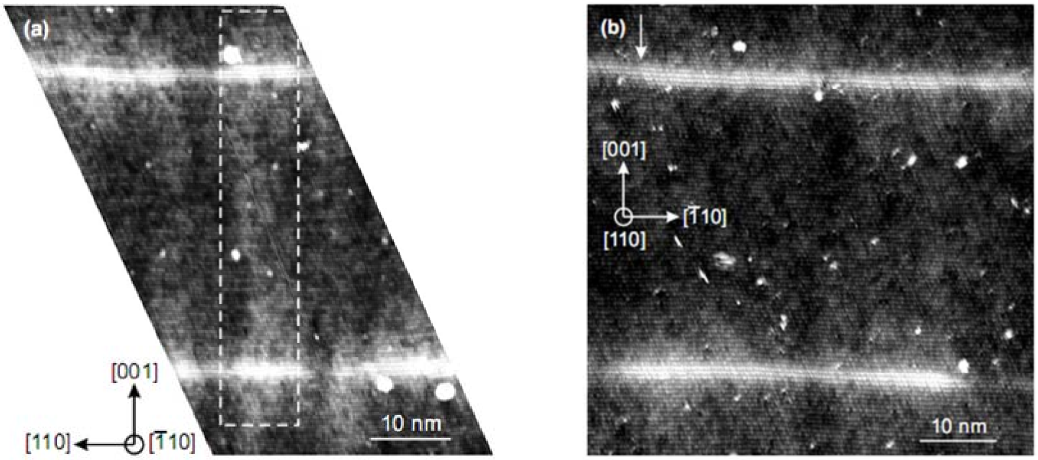

Figure 2 Filled-state cross-sectional scanning tunneling microscope (X-STM) images of two QDash layers at (a) the (-110) surface, taken at -2.7 V, and (b) the (110) surface, taken at -2.6 V [2].

The complexities of InAs nanostructure formations on InP (100) substrates are controversial, in particular QDash (QWR) or QD formation is possible for often similar growth conditions, e.g. growth temperature[8,9], InAs amount [2,10], As flux [11], composition of buffer layer [12], substrate orientation [10,13]. For the same buffer layer material, e.g., on the InP buffer layer one can find the conditions leading to the formation of both QDs and QDashes [4,8,14]. Similar results are also reported for $\mathrm{In_{0.53}Ga_{0.47}As}$ [15,16], $\mathrm{In_{0.48}Al_{0.52}As}$ ternary [8,17,18], and $\mathrm{In_{0.53}Ga_{0.23}Al_{0.24}As}$ quaternary buffer layers lattice-matched to the InP substrate [1,19]. From literature studies there are some efforts to control the formation and switching between QDs and QDashes due to changes of the InAs coverage, growth temperature, As flux, and influence of step edges or substrate miscut, however, it is still not yet conclusive.

Despite the fact that the QDash geometry is far from an ideal dot shape, most of the advantages expected for quasi-zero-dimensional structures can be preserved and high device performances can be obtained owing to a high dash density. Applications such as QDash lasers [20] and QDash SOAs [1] have been proposed and demonstrated showing good material characteristics.

3.3 As/P Exchange Reaction in InAs/InP QD Growth

Despite the fact of low mismatch (3.2 %) between the InAs and InP materials, it is generally well-known that the difficulties to control the self-assembly of InAs/InP QDs partly arise due to the complexity of the dot formation mechanism associated with the chemical reactions at the surface. For typical growth conditions, the P atoms on the InP surface are easily exchanged by As atoms (As/P exchange reaction, shown in Fig. 3), deteriorating the interface quality of heterostructures [21-23], when the InP surface is exposed to an As ambient. It has been shown that the As/P exchange reaction might be enhanced at high temperature and high As flux rate [24-27]. Moreover, the As/P exchange reaction at the InP surface alone was used for the formation of InAs dots [28]. In the case of InAs/InP self-assembled QDs, the local variation in the strain field around the dots may make the As/P exchange reaction even more complicated, significantly altering the kinetic processes of the self-assembled QD formation. It has been shown that the production of excess InAs (more amount of InAs that provided from the sources) is due to to the As/P exchange reaction [27,29] shifting the emission wavelength of QDs to beyond 1.6 µm at room temperature (RT) [30].

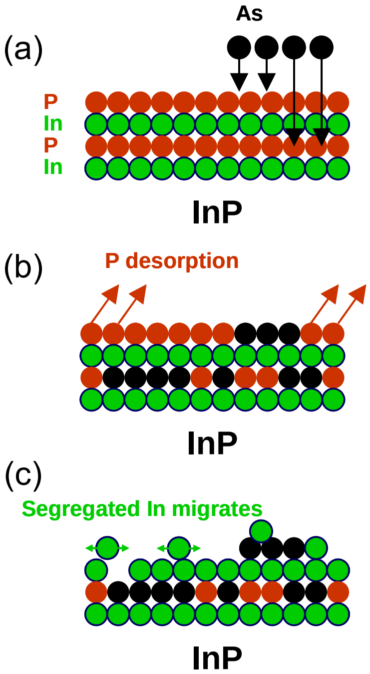

Figure 3 Schematic illustration of the As/P exchange reaction during (a) InP surface exposed to As flux, As and P substitution occurs, (b) P desorption, and (c) segregation of In adatoms floating on the surface.

Apart from the PL redshift, the As/P exchange reaction is the main reason for rough interfaces, nonuniform layers, and PL broadening for InAs/InP QDs [21,27,31,32]. Attempts to control the QD emission wavelength by thin capping and annealing usually resulted in enhanced size fluctuations producing multiple peaks in PL measurements [33]. A further improvement in geometry control was achieved by a double cap layer technique [34], which allows a reduction of the dot height and an emission wavelength of 1.5 µm was achieved. PL emission and lasing at 1.55 µm were achieved with quasi-one-dimensional InAs/InP QDashes instead of zero-dimensional QDs grown by MBE, which, however, behave more like QWRs with relatively weak lateral carrier confinement [35].

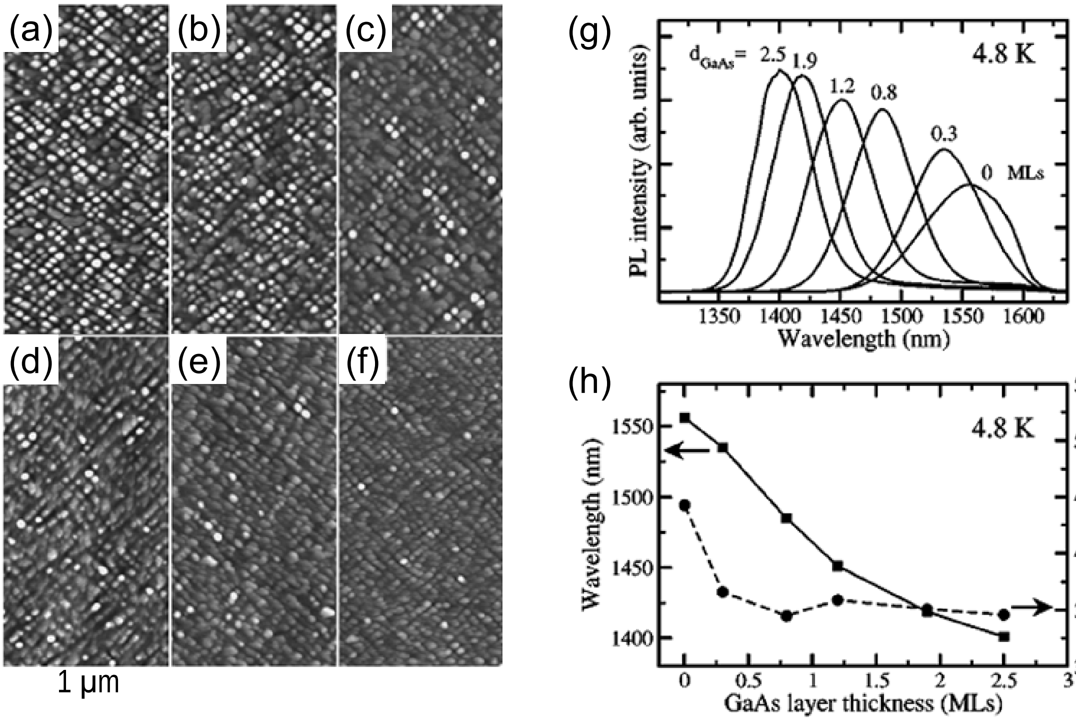

Figure 4 Left-hand side: AFM images of the InAs QDs on lattice-matched InGaAsP with thin GaAs interlayers between the InAs QD layer and InGaAsP buffer. The GaAs layer thickness is (a) 0.0, (b) 0.3, (c) 0.8, (d) 1.2, (e) 1.9, and (f) 2.5 MLs. The height contrast is 10 nm for (a)-(c) and 5 nm for (d)-(f). Right-hand side: (g) PL spectra at 4.8 K of the corresponded InAs QDs on lattice-matched InGaAsP with thin GaAs interlayers with different thicknesses. (b) The dependence of the PL peak wavelength and linewidth on the GaAs layer thickness. Adapted from Q. Gong *et al.* [36].

Recently, Gong et al. [36] proposed and demonstrated a method to reproducibly tune the emission wavelength of InAs/InP QDs grown by CBE in the 1.55-µm wavelength region by the insertion of an ultrathin (zero to 2.0 MLs) GaAs interlayer between the InAs QDs and the InGaAsP layer underneath. As a function of thickness, the GaAs interlayer effectively suppresses the As/P exchange reaction, which continuously reduces the QD height to tune the emission wavelength from above 1.6 µm to below 1.55 µm at RT [36]. The AFM images of 3.2 MLs InAs QD layers grown on top of 100 nm InGaAsP lattice-matched to InP (100) substrates and the corresponding PL spectra are shown in Fig. 4 for different GaAs interlayer thickness. This can be understood from the chemical bond strength differences between As and P to group-III elements. In-As bonds (with bond strength of 48.0 kcal/mol) are slightly more stable than In-P bonds (47.3 kcal/mol) [37], favoring the replacement of In-P by In-As bonds, i.e., the substitution of P by As atoms on InP. On the contrary, the Ga-P bond (54.9 kcal/mol) and Ga-As bond (50.1 kcal/mol) are more stable than the In-As and In-P bonds, thus suppressing As/P exchange for GaAs terminated surfaces. Moreover, the GaAs layer consumes the free segregated In adatoms floating on the surface, thereby reducing the amount of In migrating toward the apex of the InAs islands. An ultrathin GaP interlayer was also demonstrated for suppressing the As/P exchange reaction during InAs/InP QD formation [38], and similar experiments with inserted GaAs interlayers were performed by MOVPE [39]. Recently, cross-sectional scanning tunneling microscope (X-STM) measurements revealed the significance of the GaAs interlayers leading to a planar QD growth surface and decrease of QD composition intermixing, producing almost pure InAs QDs [40].

The wavelength tuning by the insertion of ultrathin GaAs interlayers beneath the InAs QD layers will serve as a basis technique used for the wavelength tuning into the 1.55 µm telecom wavelength region for InAs/InP QD arrays studied in this thesis.

3.4 Experimental Details

The samples were grown by chemical beam epitaxy (CBE) using pressure controlled Trimethylindium (TMI), Triethylgallium (TEG), AsH_3 and PH_3 as precursors. The AsH_3 and PH_3 gases were thermally decomposed in a high-temperature injector at 900 ˚C. The InP (100) substrates, mis-oriented by 2˚ toward (110) were mounted by In on the Mo blocks. The grown structures consist of 200-nm InP buffer, 100-nm lattice-matched $In_{1-x}Ga_xAs_yP_{1-y}$ ($x = 0.26$, $y = 0.53$) with band gap at 1.25 µm (Q1.25), which is our standard waveguide core material in InP-based optoelectronic devices, and finally 4.0 monolayers (ML) InAs for nanostructure formation followed by 10 s annealing under As flux before cooling down. For the lattice-matched InGaAsP layers the PH_3 pressure was kept constant at 1.8 Torr while the AsH_3 pressure was adjusted according to the growth temperature. The growth rate of InAs was 0.47 ML/s and the growth temperature was between 500 and 515 ˚C, determined by an infared pyrometer.

The samples were characterized by tapping-mode atomic force microscopy (AFM) in ambient conditions. The inner crystalline structure was analyzed by high-resolution X-ray diffraction (XRD). For photoluminescence

(PL) measurements the InAs nanostructures were covered by 100 nm Q1.25 InGaAsP. A Nd:YAG (yttrium aluminum garnet) laser (532 nm) with excitation power density of 256 mW/cm^2 served as excitation source. The samples were mounted in a He-flow cryostat for low-temperature (4.8 K) measurements. The PL was dispersed by a single monochromator and detected by a cooled InGaAs linear photodiode array.

3.5 Results and Discussion

3.5.1 Growth Temperature

Figure 5 (a) shows the AFM image of the lattice-matched Q1.25 InGaAsP buffer layer grown at 500 ˚C, and Fig. 1 (b) that of the InAs layer on top grown at the same temperature. The AsH_3 pressure of 1.2 Torr is kept the same for growth of the lattice-matched buffer and InAs layer. The buffer layer surface exhibits a pronounced asymmetric corrugation with grooves oriented along [0-11], which is the direction of long diffusion length of adatoms under these growth conditions [3]. InAs QDashes are formed on this buffer layer, elongated along the same direction.

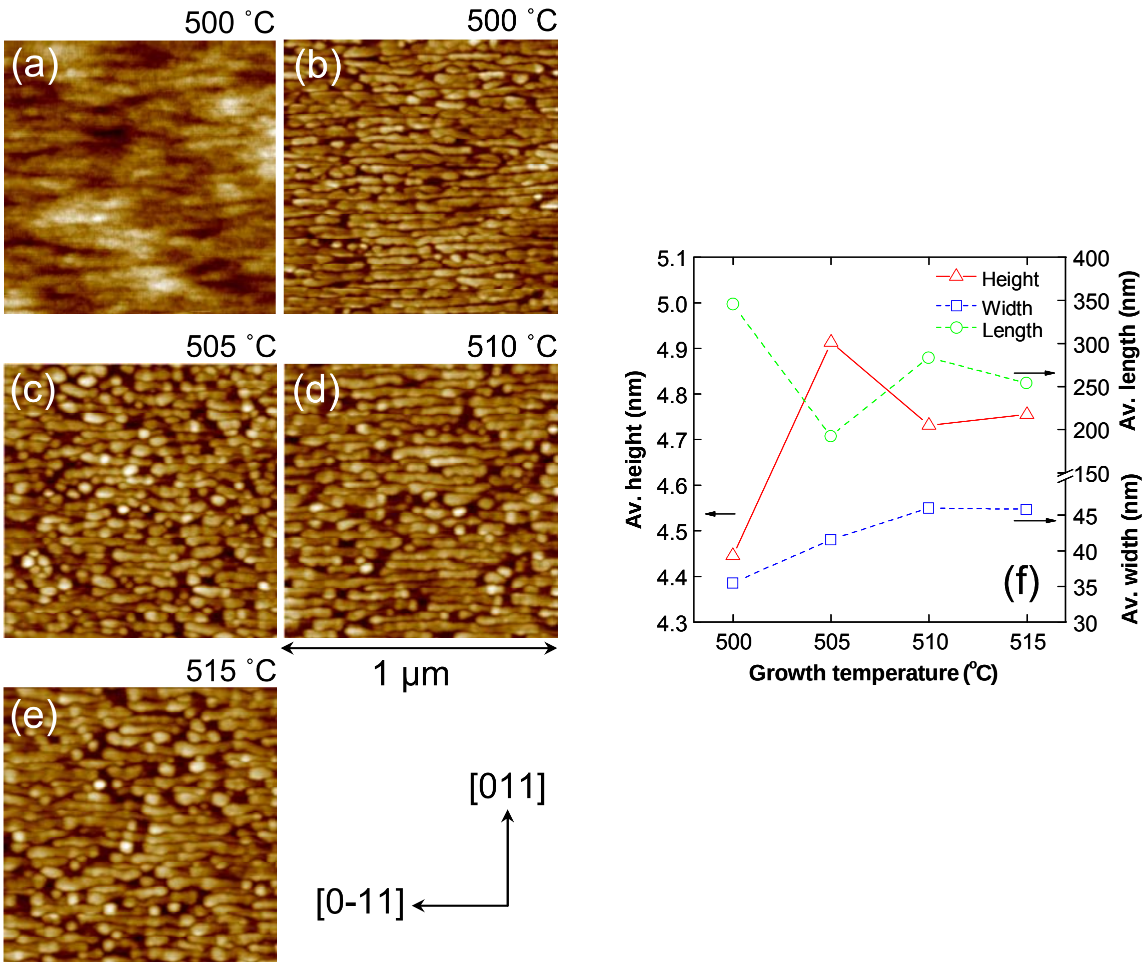

Figure 5 (a) AFM image of lattice-matched InGaAsP buffer layer grown at 500 ˚C. (b-e) AFM images of uncapped 4.0 ML InAs grown on InGaAsP buffer layers at temperatures of (b) 500, (c) 505, (d) 510, and (e) 515 ˚C. The scan field is 1.0 × 1.0 μm^2 and the height contrast is (a) 5 nm and (b-e) 10 nm. (f) Average height, width, and length of InAs nanostructures as function of the InAs growth temperature.

When the temperature is increased for InAs growth (ramped up within 2 min with the buffer layer surface exposed to As and P flux), the formation of QDs is initiated, as shown in Fig. 5 (c-e) for the InAs layers grown at (c) 505, (d) 510, and (e) 515 ˚C. This is in agreement with reports of a more homogeneous surface diffusion of adatoms at higher temperature breaking up the QDashes into QDs [9]. The QDs begin to form at 505 ˚C, above which no further significant change of the surface morphology occurs. This is reflected by the average height, width, and length of the InAs nanostructures plotted in Fig. 1 (f) as a function of the InAs growth temperature. Between 500 and 505 ˚C, the average height strongly increases and the length considerably reduces. For higher InAs growth temperatures the average height and length slightly vary while the average width remains between 35 and 45 nm. However, in the whole temperature range QDashes are dominating.

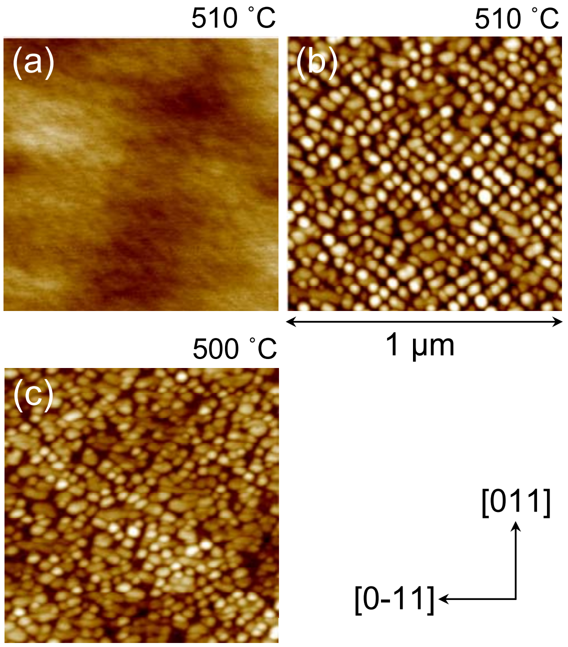

Figure 6 (a) AFM image of lattice-matched InGaAsP buffer layer grown at 510 ˚C. (b,c) AFM images of uncapped 4.0 ML InAs grown on InGaAsP buffer layers at temperatures of (b) 510, and (c) 500 ˚C. The scan field is 1.0 × 1.0 µm^2 and the height contrast is (a) 5 nm and (b,c) 10 nm.

On the other hand, when both the buffer and InAs layer are grown at 510 ˚C, the surface of the buffer layer is smooth and InAs QDs are formed, as shown in the AFM images in Fig. 6 (a) and (b). The AsH_3 pressure of 1.3 Torr is kept the same for growth of the lattice-matched buffer and InAs layer. The QDs with a density of 4×10^{10} cm^{-2} are round-shaped with an average height of 8 nm and diameter of 50 nm. In addition, when the buffer layer is grown at 510 ˚C and is, hence, smooth and the InAs layer is grown at 500 ˚C, also QDs form, as shown in Fig. 2 (c), unlike on the rough buffer layer grown at 500 ˚C where QDashes form [see Fig. 1 (b)]. The QDs are less uniform compared to those grown at 510 ˚C which is attributed to the reduced In adatom migration length at lower temperature.

These are clear indications that the formation of InAs QDs or QDashes is induced by the buffer layer morphology which, in particular in CBE, is very sensitive to the growth temperature [41,42], discussed in Chapter 1, and less by the InAs growth conditions themselves. Once, the buffer layer is rough, QDashes are formed while for the same InAs growth temperature on a smooth buffer layer QDs develop. This is understood by the asymmetric surface corrugation of the rough buffer layers enhancing the asymmetric surface diffusion of In adatoms and the asymmetric strain distribution/relaxation (commonly discussed as origin for QDash formation) to promote the evolution of InAs QDashes along the grooves. On the other hand, round-shaped QDs are reproducibly formed on smooth surfaces where the In adatom migration and strain distribution/relaxation are more symmetric.

Investigations of other growth parameters such as As flux and buffer layer strain and composition discussed in the following paragraphs underline this behavior. Moreover, the orientation of the QDashes along [0-11] excludes their origin to be related to steps on vicinal surfaces [10,13] which are oriented along [001] for the present miscut.

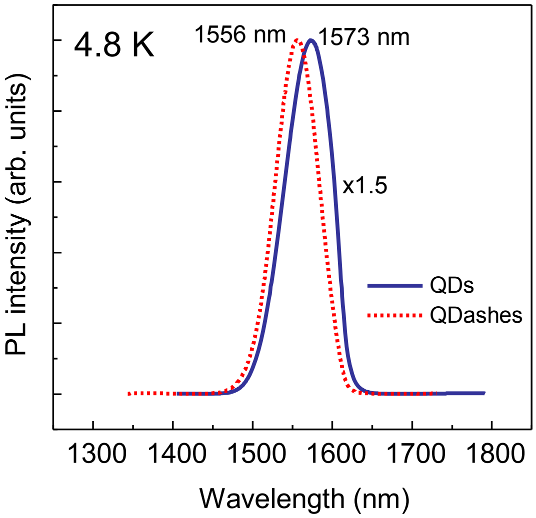

Figure 7 PL spectra taken at 4.8 K of capped 3.2 ML InAs QDs (solid line) and QDashes (dashed line) embedded in lattice-matched InGaAsP grown at 510 and 500 ˚C.

The low-temperature (4.8 K) PL spectra of the InAs QDs (InGaAsP and InAs grown at 510 ˚C with AsH_3 pressure of 1.3 Torr) and QDashes (InGaAsP and InAs grown at 500 ˚C with AsH_3 pressure of 1.2 Torr) are depicted in Fig. 7. Both the QDs and QDashes exhibit comparable PL efficiency. Hence, despite of the rough buffer layer morphology, QDashes with comparable optical quality as that of the QDs are formed. Therefore, with respect to morphology and optical quality the QDashes discussed here are not distinguished from those discussed previously in the literature where the buffer layer morphology was not considered. The PL peak of the QDashes (at 1556 nm) is shifted by 17 nm to shorter wavelength with respect to that of the QDs (at 1573 nm). This is in line with the smaller average height of the QDashes, which makes it easier to reach the 1.55 µm wavelength region at room temperature with QDashes than with QDs [20] – but QDashes behave more like QWires [7].

Considering, however, the height of the QDashes measured by AFM, a larger blue-shift of the PL of the QDashes with respect to that of the QDs is expected. This is attributed to the fact that the QDashes are formed on the rough buffer layer. Growth on rough surfaces commonly results in a red-shift of the PL of nanostructures due to enhancement of the formation of locally thicker and thinner regions. If the height of the surface corrugation of the buffer layer of 1 – 4 nm is added to the height of the QDashes measured by AFM the total height of the QDashes (though probably overestimated in this way) becomes comparable to that of the QDs. Moreover, the QDashes structure comprises cross sectional fluctuation which can be potentially introduce some QD-like effects due to carriers localization.

3.5.2 As Flux

Figure 8 (a-c) shows the AFM images of the InAs layers grown at 500 ˚C on the (rough) buffer layers grown at 500 ˚C for AsH_3 pressures during InAs growth of (a) 0.8, (b) 1.2 (reference pressure used for lattice-matched InGaAsP (at 500 ˚C) and InAs growth in Fig. 5), and (c) 1.75 Torr. Evidently, QD formation is favored with increasing height for higher As flux due to enhanced As/P exchange, which is indicated by the increasing average height, shown in Fig. 8 (d). However, round-shaped QDs cannot develop on the rough buffer layer, as revealed by the average width and length plotted in Fig. 8 (d).

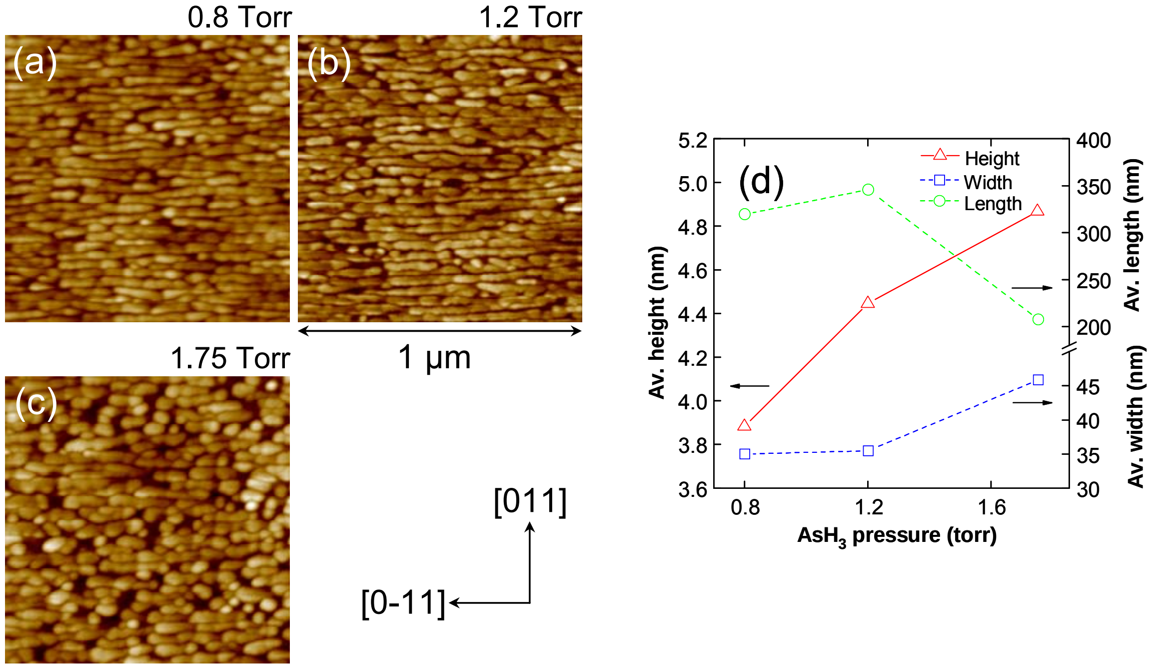

Figure 8 AFM images of uncapped 4.0 ML InAs grown at 500 ˚C on (rough) lattice-matched InGaAsP buffer layers with AsH_3 pressure of (a) 0.8, (b) 1.2, and (c) 1.75 Torr. The scan field is 1.0 × 1.0 μm^2 and the height contrast is 10 nm. (d) Average height, width, and length of the InAs nanostructures as function of the AsH_3 pressure.

The dependence of the InAs surface morphology on the AsH_3 pressure for InAs deposited at 510 ˚C on the (smooth) buffer layer grown at 510 ˚C is shown in Fig. 9 (a-c) for (a) 0.8, (b) 1.3 (reference pressure used for lattice-matched InGaAsP (at 510 ˚C) and InAs growth in Fig. 6), and (c) 1.75 Torr. The lowest As flux results in the formation of QDashes while for higher As flux, QDs are formed whose height increases with the As flux, as shown in Fig. 9 (e), again due to enhanced As/P exchange. This behavior, which we have observed earlier also for the growth by metalorganic vapor phase epitaxy (MOVPE) [39] has been recently attributed to the As flux dependent surface energy, favoring either QDs or QDashes [11]. Inspecting, however, the InGaAsP buffer layer surface after short exposure to the low As flux (the AsH_3 pressure is decreased to 0.8 Torr for 5 sec without changing the PH_3 pressure before the sample is cooled down) reveals pronounced asymmetric roughness, shown in Fig. 9 (d). This is attributed to a destabilization of the originally smooth InGaAsP surface for low As flux. Hence, the formation of QDashes for low As flux is again attributed to the surface morphology of the buffer layer which quickly roughens during the time necessary to stabilize the As flux.

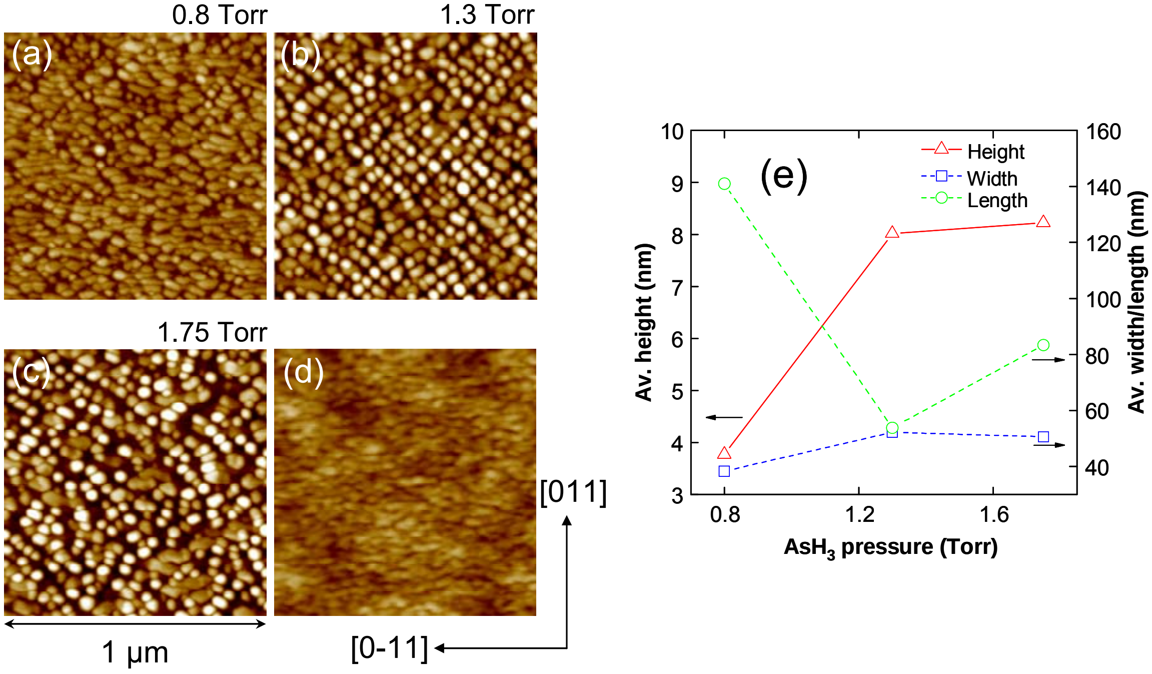

Figure 9 (a-c) AFM images of uncapped 4.0 ML InAs grown at 510 ˚C on (smooth) lattice-matched InGaAsP buffer layers with AsH_3 pressure of (a) 0.8, (b) 1.3, and (c) 1.75 Torr. (d) AFM image of lattice-matched InGaAsP buffer layer grown at 510 ˚C and 5 s exposed to low As flux (AsH_3 pressure of 0.8 Torr). The scan field is 1.0 × 1.0 μm^2 and the height contrast is (a-c) 10 nm and (d) 5 nm. (e) Average height, width, and length of the InAs nanostructures as function of the AsH_3 pressure.

The differences between the morphology of the buffer layer in Fig. 5 (a) and 9 (d) is that the lateral extension of the elongated grooves in Fig. 5 (a) (average length of 442 nm) is longer than that in Fig. 9 (d) (average length of 145 nm). Therefore, when InAs is deposited on the buffer layer in Fig. 5 (a) the QDashes extend to several hundred nm through the dimension of the grooves, while the extension of the QDashes on the buffer layer in Fig. 9 (d) is limited to about 100-200 nm. The lateral extension of the grooves of the buffer layer in Fig. 5 (a) (grown at 500 ˚C) is likely longer since the asymmetric roughness develops during growth while the shorter lateral extension of the grooves of the buffer layer in Fig. 9 (b) is attributed to the fact that the buffer layer is originally smooth (growth at 510 ˚C) and the roughness is only induced by the low As flux after growth.

3.5.3 Strain and Composition of InGaAsP Buffer Layer

The influence of strain and composition of the InGaAsP buffer layer on the morphology of the InAs layer is revealed in Fig. 10 (a-e). Growth of the buffer layer is performed at 500 ˚C and that of the InAs layer at 510 ˚C under high AsH_3 pressure of 1.75 Torr, conditions which promote QD formation on the rough buffer layers. The lattice mismatch of the buffer layers is adjusted by the PH_3 pressure during growth and indicated by the angular separation of the XRD peak of the buffer layer with respect to that of the substrate, recorded in the vicinity of the symmetric (004) reflection (negative for compressive strain and positive for tensile strain). The reference lattice-matched sample is shown in Fig. 10 (c).

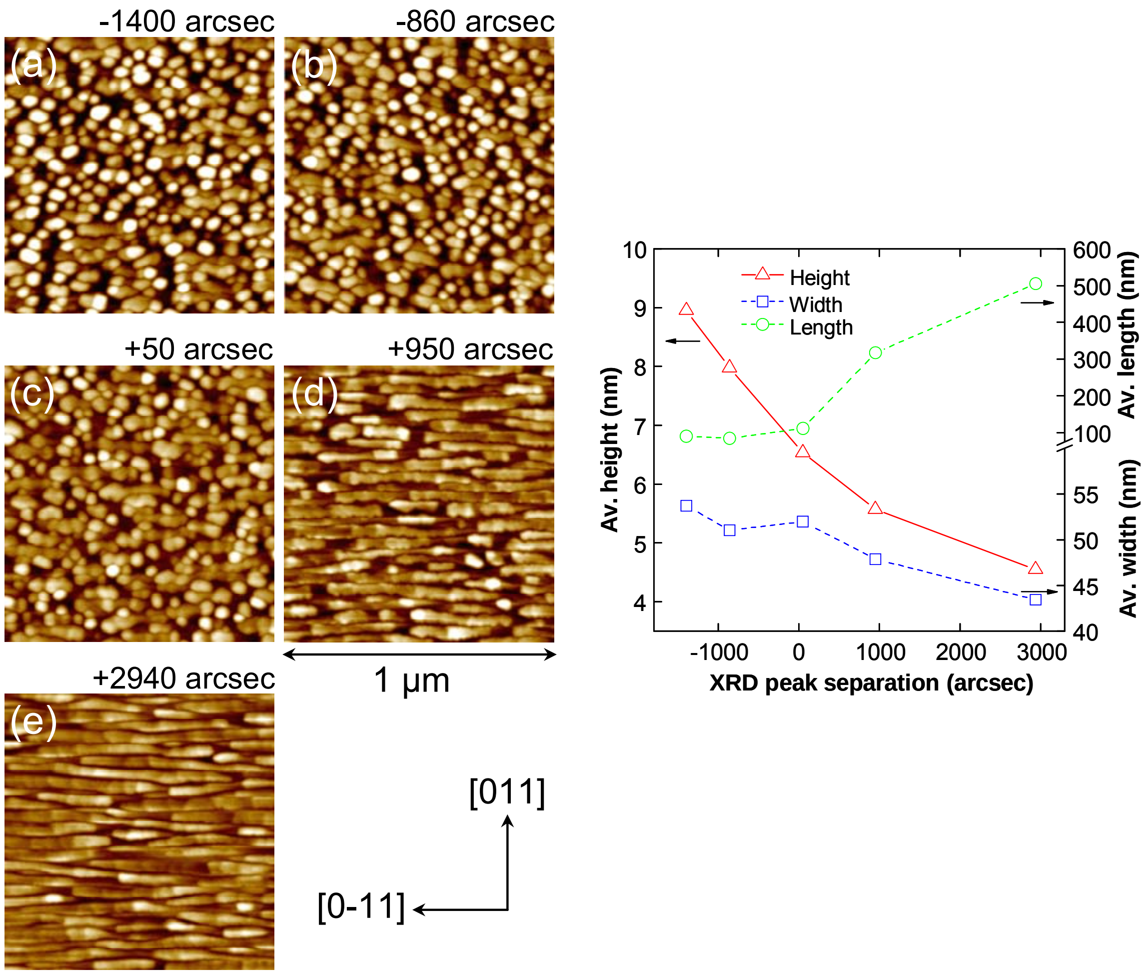

Figure 10 (a)-(e) AFM images of 4.0 ML InAs grown at 510 ˚C on InGaAsP buffer layers grown at 500 ˚C with lattice mismatch determined by XRD (angular separation recorded in the vicinity of the symmetric (004) reflection) of (a) -1400, (b) -860, (c) +50, (d) +950, and (e) +2940 arcsec. The scan field is 1.0 × 1.0 μm^2 and the height contrast is 10 nm. (f) Average height, width, and length of the InAs nanostructures as function of the lattice mismatch.

The formation of QDs is promoted for compressive buffer layer strain, however, QDashes are still dominant in contrast to the growth on smooth buffer layers grown at 510 ˚C [see for example Fig. 9 (c)]. Long QDashes are formed for tensile strain, which is again reflected by an increasing average length and decreasing average height as a function of lattice mismatch, shown in Fig. 10 (f). This behavior is attributed to compressively strained buffer layers being InAs rich favoring the formation of the (compressively strained) InAs QDs.

However, care should be taken with the most highly compressively and tensile strained buffer layers which are partially relaxed. Hence, the development of the InAs nanostructures in Fig. 10 (a) and 10 (e) might partially originate from the differences of the in-plane lattice constants of the relaxed buffer layers, which have been determined from asymmetric XRD scans in the vicinity of the (224) reflection. The in-plane lattice constant of the highly compressively strained buffer layer [Fig. 10 (a)] is 5.952 Å corresponding to a misfit of 1.42 % and the in-plane lattice constant of the highly tensile strained buffer layer [Fig. 10 (e)] is 5.704 Å corresponding to a misfit of – 2.81 %. The other buffer layers [Fig. 10 (b-d)] are fully strained.

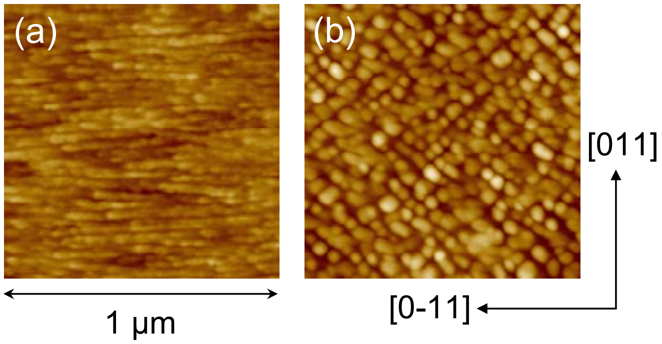

Figure 11 (a), (b) AFM images of 3.2 ML InAs on 1 ML GaAs interlayer on lattice-matched InGaAsP buffer layer grown all at (a) 500 and (b) 510 ˚C. The scan field is 1.0 × 1.0 μm^2 and the height contrast is 10 nm.

Finally, the formation of QDs or QDashes is not influenced by the presence of a GaAs interlayer underneath the InAs layer, which allows control of the InAs nanostructure height and emission wavelength [36,39]. For (rough) buffer layers grown at 500 ˚C, QDashes form in the presence of the 1 ML GaAs interlayer while on (smooth) buffer layers grown at 510 ˚C, QDs are developed, as shown in Fig. 11 (a) and (b). This underlines the crucial influence of the buffer layer morphology on the formation of QDs or QDashes dominating any influence of buffer layer strain and composition or other growth parameters such as growth temperature and As flux, discussed in the previous paragraphs.

3.6 Summary

In summary, we have identified the significance of the morphology of the InGaAsP buffer layer on the formation of either InAs QDs or QDashes on InP (100) substrates. Growth conditions leading to the formation of QDashes are always accompanied by a rough buffer layer morphology. Although other growth parameters such as higher growth temperature, larger As flux, and compressive buffer layer strain favor the formation of QDs, once, the buffer layer is rough, formation of QDashes dominates. On smooth buffer layers, for the same InAs growth conditions, we reproducibly find well-shaped, symmetric InAs QDs. Hence we conclude, that not the growth conditions during InAs deposition but rather the related surface morphology of the buffer layer governs the formation of InAs QDs or QDashes, which exhibit comparable optical quality.

Bibliography

[1] J. P. Reithmaier, A. Somers, S. Deubert, R. Schwertberger, W. Kaiser, A. Forchel, M. Calligaro, P. Resneau, O. Parillaud, S. Bansropun, M. Krakowski, R. Alizon, D. Hadass, A. Bilenca, H. Dery, V. Mikhelashvili, G. Eisenstein, M. Gioannini, I. Montrosset, T. W. Berg, M. van der Poel, J. Mørk, and B. Tromborg, *J. Phys. D: Appl. Phys.* **38**, 2088 (2005).

[2] A. Lenz, F. Genz, H. Eisele, L. Ivanova, R. Timm, D. Franke, H. Künzel, U. W. Pohl, and M. Dähne, *Appl. Phys. Lett.* **95**, 203105 (2009).

[3] Q. Guo, M. E. Pemble, and E. M. Willliams, *Surf. Sci.* **433**, 410 (1999).

[4] H. J. Parry, M. J. Ashwin, and T. S. Jones, *J. Appl. Phys.* **100**, 114305 (2006).

[5] J. M. Garcia, L. Gonzalez, M. U. Gonzalez, J. P. Silveira, Y. Gonzalez, and F. Briones, *J. Crystal Growth* **227-228**, 975 (2001).

[6] P. Miska, J. Even, C. Platz, B. Salem, T. Benyattou, C. Bru-Chevalier, G. Guillot, G. Bremond, Kh. Moumanis, F. H. Julien, O. Marty, C. Monat, and M. Gendry, *J. Appl. Phys.* **95**, 1074 (2004).

[7] H. Dery, E. Benisty, A. Epstein, R. Alizon, V. Mikhelashvili, G. Eisenstein, R. Schwertberger, D. Gold, J. P. Reithmaier, and A. Forchel, *J. Appl. Phys.* **95**, 6103 (2004).

[8] C. Walther, W. Hoerstel, H. Niehus, J. Erxmeyer, and W. T. Masselink, *J. Crystal Growth* **209**, 572 (2000).

[9] Z. H. Zhang, G. W. Pickrell, K. L. Chang, H. C. Lin, K. C. Hsieh, and K. Y. Cheng, *Appl. Phys. Lett.* **82**, 4555 (2003).

[10] A. Stintz, T. J. Rotter, and K. J. Malloy, *J. Crystal Growth* **255**, 266 (2003).

[11] G. Saint-Girons, A. Michon, I. Sagnes, G. Beaudoin, and G. Patriarche, *Phys. Rev. B* **74**, 245305 (2006).

[12] J. Brualt, M. Gendry, G. Grenet, G. Hollinger, Y. Desieres, and T. Benyattou, *Appl. Phys. Lett.* **73**, 2932 (1998).

[13] O. Bierwagen and W. T. Masselink, *Appl. Phys. Lett.* **86**, 113110 (2005).

[14] S. Barik, H. H. Tan, and C. Jagadish, *Nanotechnology* **17**, 1867 (2006).

[15] Z. H. Zhang and K. Y. Cheng, *Appl. Phys. Lett.* **83**, 3183 (2003).

[16] J. Brault, M. Gendry, G. Grenet, G. Hollinger, Y. Desieres, and T. Benyattou, *Appl. Phys. Lett.* **73**, 2932 (1998).

[17] S. Fafard, Z. Wasilewski, J. McCaffrey, S. Raymond, and S. Charbonneau, *Appl. Phys. Lett.* **68**, 991 (1995).

[18] H. Li, T. Daniels-Race, and M.-A. Hasan, *Appl. Phys. Lett.* **80**, 1367 (2002).

[19] X. B. Zhang, J. H. Ryou, and R. D. Dupuis, *Appl. Phys. Lett.* **89**, 191104 (2006).

[20] R. H. Wang, A. Stintz, P. M. Varangis, T. C. Newell, H. Li, K. J. Malloy, and L. F. Lester, *IEEE Photon. Technol. Lett.* **13**, 767 (2001).

[21] R. P. Schneider Jr. and B. W. Wessels, *Appl. Phys. Lett.* **57**, 1998 (1990).

[22] G. Hollinger, D. Gallet, M. Gendry, C. Santinelli, and P. Vikorovitch, *J. Vac. Sci. Technol. B* **8**, 832 (1990).

[23] M. R. Bruni, N. Gambacorti, S. Kaciulis, G. Mattogno, M. G. Simeone, L. G. Quagliano, N. Tomassini, and B. Jusserand, *J. Crystal Growth* **150**, 123 (1995).

[24] Y. Kobayashi and N. Kobayashi, *Jpn. J. Appl. Phys.* **31**, 3988 (1992).

[25] Z. Sobiesierski, D. I. Westwood, P. J. Parbrook, K. B. Ozanyan, M. Hopkinson, and C. R. Whitehouse, *Appl. Phys. Lett.* **70**, 1423 (1997).

[26] Y. Kobayashi and N. Kobayashi, *J. Crystal Growth* **145**, 17 (1994).

[27] S. Yoon, Y. Moon, T. -W. Lee, E. Yoon, and Y. D. Kim, *Appl. Phys. Lett.* **74**, 2029 (1999).

[28] B. Wang, F. Zhao, Y. Peng, Z. Jin, Y. Li, and S. Liu, *Appl. Phys. Lett.* **72**, 2433 (1998).

[29] M. Taskinen, M. Sopanen, H. Lipsanen, J. Tulkki, T. Toumi, and J. Ahopelto, *Surf. Sci.* **376**, 60 (1997).

[30] M. Borgström, J. Johansson, L. Landin, and W. Seifert, *Appl. Surface. Sci.* **165**, 241 (2000).

[31] K. Ozasa, Y. Aoyagi, Y. J. Park, and L. Samuelson, *Appl. Phys. Lett.* **71**, 797 (1997).

[32] T. Y. Wang, E. H. Reihlen, H. R. Jen, and G. B. Stringfellow, *J. Appl. Phys.* **66**, 5376 (1989).

[33] Y. Sakuma, K. Taketomo, S. Hirose, T. Usuki, and N. Yokoyama, *Physica E* **26**, 81 (2005).

[34] C. Paranthoen, C. Platz, G. Moreau, N. Bertru, O. Dehaese, A. Le Corre, P. Miska, J. Even, H. Folliot, C. Labbé, G. Patriarche, J. C. Simon, and S. Loualiche, *J. Crystal Growth* **251**, 230 (2003).

[35] R. Schwertberger, D. Gold, J. P. Reithmaier, and A. Forchel, *J. Crystal Growth* **251**, 248 (2003).

[36] Q. Gong, R. Nötzel, P. J. van Veldhoven, T. J. Eijkemans, and J. H. Wolter, *Appl. Phys. Lett.* **84**, 275 (2004).

[37] T. Anan, S. Sugou, K. Nishi, and T. Ischihashi, *Appl. Phys. Lett.* **63**, 1047 (1993).

[38] Q. Gong, R. Nötzel, P. J. van Veldhoven, T. J. Eijkemans, and J. H. Wolter, *Appl. Phys. Lett.* **85**, 1404 (2004).

[39] S. Anantathanasarn, R. Nötzel, P. J. van Veldhoven, T. J. Eijkemans, and J. H. Wolter, *J. Appl. Phys.* **98**, 013503 (2005).

[40] J. M. Ulloa, S. Anantathanasarn, P. J. van Veldhoven, P. M. Koenraad, and R. Nötzel, *Appl. Phys. Lett.* **92**, 083103 (2008).

[41] T. H. Chiu, M. D. Williams, T. K. Woodward, J. E. Cunningham, J. E. Zucker, T. Sizer, F. G. Storz, J. F. Ferguson, and W. T. Tsang, *J. Crystal Growth* **124**, 165 (1992).

[42] J. L. Benchimol, G. Le Roux, H. Thibierge, C. Daguet, F. Alanxandre, and F. Brillouet, *J. Crystal Growth* **107**, 978 (1991).

CHAPTER 4

One-Dimensional Linear Ordered InAs/ InP Quantum Dot Arrays

ABSTRACT

The formation of linear InAs quantum dot (QD) arrays based on self-organized anisotropic strain engineering of an InGaAsP/InP (100) superlattice (SL) template in chemical beam epitaxy (CBE) is demonstrated and the optimized growth window is determined. InAs QD formation, thin InGaAsP capping, annealing, InGaAsP overgrowth, and stacking in SL template formation produces wire-like InAs structures along [001] due to anisotropic surface migration, and lateral and vertical strain correlation. InAs QD ordering is governed by the corresponding lateral strain field modulation on the SL template surface. Careful optimization of InGaAsP cap layer thickness, annealing temperature, InAs amount and growth rate, and number of SL periods results in straight and well-separated InAs QD arrays. The InAs QD arrays exhibit excellent photoluminescence (PL) emission up to room temperature which is tuned into the 1.55-µm telecom wavelength region through the insertion of ultra-thin GaAs interlayers. Temperature dependent PL measurements and the linear polarization behavior indicate lateral electronic coupling of the QDs in the arrays.[1]

---

[1] These results have been published as: *Formation of linear InAs quantum dot arrays on InGaAsP/InP (100) by self-organized anisotropic strain engineering and their optical properties*, N. Sritirawisarn, F. W. M. van Otten, T. J. Eijkemans, and R. Nötzel, J. Appl. Phys. **102**, 053514 (2007).

4.1 Introduction

In this chapter, we study the concept of self-organized anisotropic strain engineering for the InAs/InGaAsP material system on InP (100) by chemical beam epitaxy (CBE) and optimize the growth conditions for formation of well-ordered, linear InAs QD arrays with photoluminescence (PL) emission in the technologically important 1.55 µm telecom wavelength region. InAs/InGaAsP superlattice (SL) template formation comprises InAs QD formation, thin InGaAsP capping, annealing, InGaAsP overgrowth, and stacking. This produces wire-like InAs structures due to anisotropic adatom surface migration during annealing, together with lateral and vertical strain correlation and strain gradient driven In adatom migration during stacking. The corresponding lateral strain field modulation on the SL template surface governs InAs QD ordering due to local strain recognition. The presence of linear QD arrays depends on the substrate miscut altering the adatom surface migration. The optimum substrate miscut is 2° towards (110) for which the InGaAsP cap layer thickness, annealing temperature, InAs amount and growth rate, and number of SL periods are optimized for the formation of straight and well-separated QD arrays along [001]. The PL emission of the optimized InAs QD arrays is tuned into the 1.55-µm-wavelength region through the insertion of an ultra-thin GaAs interlayer beneath the InAs QD arrays. Excellent PL emission from the QD arrays is observed up to room temperature (RT). In temperature dependent PL measurements the characteristic minimum of the PL full-width at half-maximum (FWHM) and the enhanced low-energy shift of the PL peak due to thermally activated carrier redistribution typical for randomly arranged QDs are hardly observed [1,2]. This indicates minimized carrier localization in the QD arrays due to lateral electronic coupling of the closely-spaced QDs in the arrays which is supported by the linear polarization of the PL along the arrays.

The experimental growth details and characterization techniques for the SL template and QD layer are given in section 4.2. The SL template development and InAs QD arrays formation and optimization of the growth conditions are systematically presented in section 4.3. The influence of substrate miscut is studied for formation of the QD arrays and well-separated and uniform arrays are developed by the adjustment of the thin cap layer thickness and annealing temperature, InAs amount and growth rate, and number of SL periods. The optimized SL template and the tuning of the InAs QD arrays PL emission wavelength into very important 1.55-µm region through the insertion of an ultrathin GaAs interlayer beneath the InAs layer are demonstrated. Section 4.4 discusses the optical properties of linear InAs QD arrays in temperature and polarization dependent measurements demonstrating electronic coupling of the QDs within the arrays. The chapter is summarized in section 4.5.

4.2 Experimental Details

The samples were grown by CBE using pressure controlled Trimethylindium (TMI), Triethylgallium (TEG), AsH_3, and PH_3 as precursors. The AsH_3 and PH_3 gases were thermally decomposed in a high temperature injector at 900 ˚C. The InP (100) substrates with different miscut summarized in Table I were mounted by In on Mo blocks. The sample structure commenced with a 200-nm InP buffer layer and 100-nm lattice-matched InGaAsP with band gap at 1.27 µm (Q1.27), which is a typical waveguide core material in InP-based optoelectronic devices. Each period of the SL template consisted of 2.1 - 3.2 monolayers (ML) InAs, 10 s growth interruption in As flux, a 0.3 - 1.0-nm thin Q1.27 cap layer, 2 min. annealing, and a 15.3-nm Q1.27 spacer layer. The number of SL periods was between 5 and 11. On top of the SL template a 2.1 – 3.2 ML InAs QD layer was grown either directly on the Q1.27 layer or on a 0.8 ML GaAs interlayer inserted beneath the QDs. For PL measurements the InAs QDs were capped by 100-nm Q1.27 and 50-nm InP. The growth temperature was 515 ˚C for all layers and the annealing temperature was between 530 and 550 ˚C. The growth rate of InAs was varied from 0.23 - 0.47 ML/s, calibrated by high-resolution x-ray diffraction (XRD).

The surface morphologies of uncapped samples were characterized by tapping-mode atomic force microscopy (AFM) in air. For the PL studies, a Nd:YAG (yttrium aluminum garnet) laser (532 nm) with excitation power density of 256 mW/cm^2 was used as excitation source. The samples were mounted in a He-flow cryostat with temperature control between 4.8 K and RT. The PL was dispersed by a single monochromator and recorded by a cooled InGaAs linear array detector.

Substrate	Miscut towards	Miscut angle
A	(110)	0.2˚
B	(111)*A*	0.5˚
C	(111)*B*	0.5˚
D	(110)	0.5˚
E	(111)*B*	2.0˚
F	(110)	2.0˚

Table 1 Denotion of the InP (100) substrates with various miscuts.

4.3 Formation of Linear QD Arrays

4.3.1 Substrate Miscut

The AFM images of 2.6 ML InAs grown on a 5 periods 2.1 ML InAs/ 15.6 nm Q1.27 SL template (0.23 ML/s InAs growth rate, 0.3 nm Q1.27 cap layer, 530 ˚C annealing temperature) on InP (100) substrates with different miscut are shown in Fig. 1. For low miscut < 0.5˚ and for miscut towards (111)A (step edges along [0-11]) dense quantum dashes (QDashes) elongated along [0-11] form, as shown in Fig. 1 (a) and (b). For miscut towards (111)B (step edges along [011]) QD arrays appear in a zig-zag arrangement, alternately oriented along [001] and [010], shown in Fig. 1 (c) and (e). Linear and well-separated QD arrays are produced on substrates miscut towards (110) (step edges along [001]) whose ordering improves with the miscut angle, shown in Fig. 1 (d) and (f).

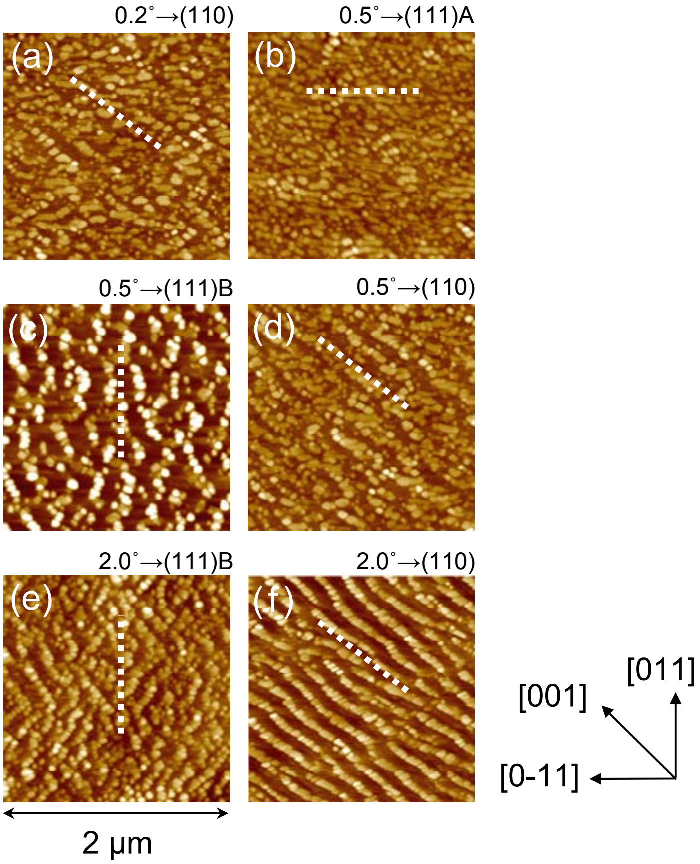

Figure 1 (a)-(f) AFM images of uncapped 2.6 ML InAs on the 5-periods 2.1 ML InAs/ 0.3 + 15.3 nm Q1.27 SL templates (InAs growth rate 0.23 ML/s, annealing temperature 530 ˚C) on InP (100) substrates with different miscut: (a) 0.2˚ toward (110), (b) 0.5˚ toward (111)A, (c) 0.5˚ toward (111)B, (d) 0.5˚ toward (110), (e) 2.0˚ toward (111)B, and (f) 2.0˚ toward (110). The scan field is 2.0 × 2.0 μm^2 and the height contrast is 20 nm. The dashed lines indicate the step edge directions.

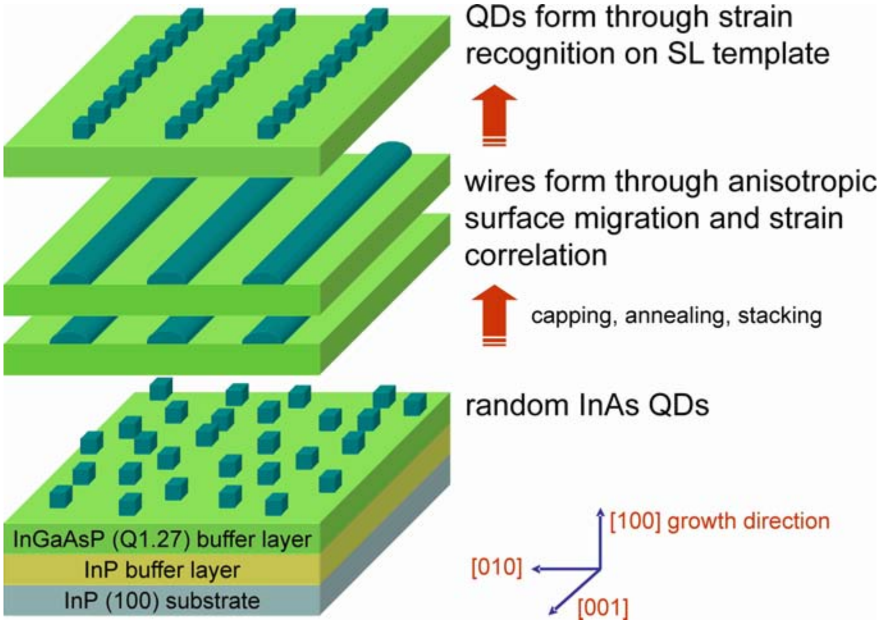

Figure 2 Schematic illustration of linear InAs QD arrays formed on InP (100) substrates

Obviously the preferential surface reconstruction and step driven adatom surface migration along [0-11] on substrates with low miscut or miscut towards (111)A hinders the formation of well-separated QD arrays, which is attributed to a too small surface migration length along [011]. As a result, dense QDashes elongated along [0-11] form during SL growth. Once the direction of adatom surface migration is altered by the presence of a sufficient density of steps along [011], QD arrays along [010] or [001], which are the elastically soft directions, form due to a large enough surface migration length perpendicular to the arrays. Linear and well-separated QD arrays along one of these directions, e.g. [001], are then formed for steps along [001]. The orientation of the QD arrays along the elastically soft directions implicates that it is determined by in-plane strain correlation governed by the cubic anisotropy of the elastic moduli [3,4]. This is different to the case of InAs/GaAs based linear QD arrays where the orientation is determined by the direction of adatom surface migration during annealing, which can be influenced by the presence of steps [5]. In the InAs/InP system the anisotropic adatom surface migration during annealing is essential only to smoothen the InAs QD arrays in each SL period towards uniform wire-like structures oriented along the elastically soft directions to minimize the strain energy. It is important to note that the ordering of the InAs QDs is purely governed by the vertical and lateral strain correlation during stacking rather than by morphological features related to steps. This is demonstrated by the unchanged orientation and lateral periodicity of the QD arrays as a function of substrate miscut, number of SL periods, and the smoothness of the SL template surface discussed below, with the lateral periodicity determined by the strain gradient driven In adatom surface migration perpendicular to the

QD arrays in successive layers, as previously discussed in chapter 2. The schematic illustration of linear InAs QD arrays formation is shown in Fig. 2.

The unchanged morphology of single QD layers on the differently miscut substrates, shown in Fig. 3, further confirms that steps have no influence on the QD formation and ordering themselves. The amount of InAs for QD formation is 3.0 ML deposited on a 100-nm Q1.27 buffer layer. For all substrate miscuts, the QD height is 6-9 nm, the base diameter 40-70 nm, and the QD density 3-5×10^{10} cm^{-2}. This is in contrast to other reports [6,7] where QDashes have been observed for substrates miscut towards [111]A. However, it agrees with our previous investigations on the formation of QDs or QDashes to be determined by the buffer layer morphology rather than the InAs growth conditions and substrate miscut, as described in the previous Chapter. QDs are formed on smooth buffer layers while rough buffer layers induce the formation of QDashes. For our growth conditions the buffer layer is smooth for all substrate miscuts and solely QDs form.

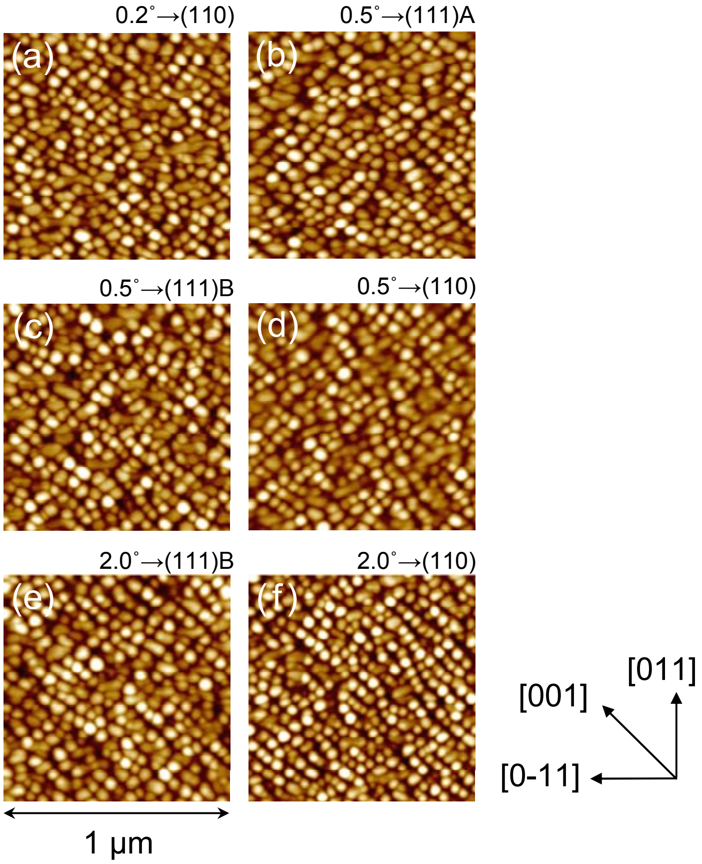

Figure 3 (a)-(f) AFM images of uncapped 3.0 ML InAs QDs on a 100-nm Q1.27 buffer layer on InP (100) substrates with different miscuts denoted in Table I. (a) Substrate A, (b) substrate B, (c) substrate C, (d) substrate D, (e) substrate E, and (f) substrate F. The scan field is 1.0 × 1.0 μm^2 and the height contrast is 10 nm.

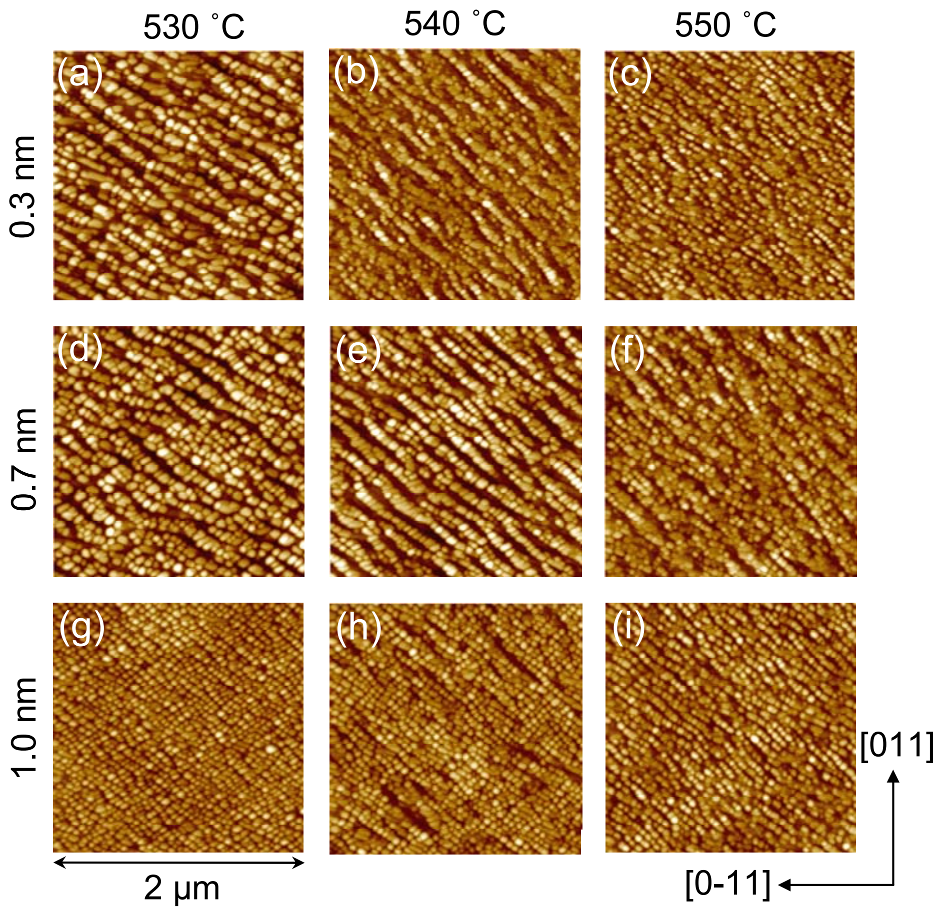

Figure 4 (a)-(i) AFM images of uncapped 3.2 ML InAs QD arrays on the 5-periods InAs/ Q1.27 SL templates (InAs amount 3.2 ML, InAs growth rate 0.47 ML/s, Q1.27 separation layer thickness 15.3 nm) with Q1.27 cap layer thicknesses of 0.3 - 1.0 nm and annealing temperatures of 530 - 550 ˚C. The scan field is 2.0 × 2.0 µm^2 and the height contrast is 20 nm.

4.3.2 Thin Cap Layer Thickness and Annealing Temperature

Optimization of the growth conditions for formation of linear and well-separated InAs QD arrays is performed on substrates miscut by 2˚ towards (110). In the series of samples shown in Fig. 3 the thickness of the thin Q1.27 cap layer above the InAs QDs is varied between 0.3 and 1.0 nm and the annealing temperature between 530 and 550 ˚C. The number of SL periods of 5, InAs amount of 3.2 ML, InAs growth rate of 0.47 ML/s, and Q1.27 spacer layer thickness of 15.3 nm are kept constant. Ordering of InAs QDs in linear arrays along [001] is clearly observed for 0.3 - 0.7 nm cap layer thickness together with annealing temperatures of 530 - 540 ˚C, as shown in Fig. 4 (a), (b), (d), and (e). Outside this growth window ordering is strongly degraded or absent. Similar to the case of InAs/GaAs, the combination of cap layer thickness and annealing temperature balances In desorption during annealing. This is essential for a smooth and straight connection of the wire-like structures requiring strain reduction, maintenance of sufficient In for vertical strain correlation, and sufficient lateral mass transport during annealing to smoothen the InAs QD arrays. For too thin cap layer and too high annealing temperature [Fig. 4 (c) and (f)], the In desorption is too high to maintain vertical strain correlation. On the other hand, for a too thick cap layer and too low growth temperature, In desorption is insufficient. The excess strain accumulation is too large and straight wire-like structures cannot form and a high density of kinks and branches is introduced in the QD arrays to relieve the strain. Moreover, smoothening of the QD arrays during annealing is suppressed and finally hindered, resulting in high-density stacked QDs [Fig. 4 (g) to (i)] which eventually develop a rough morphology for increasing excess strain accumulation during stacking, in particular when the QDs are fully capped or no annealing step is performed.

4.3.3 InAs Amount and Growth Rate

In the series of samples shown in Fig. 5 the InAs amount is decreased from 3.2 to 2.1 ML and the InAs growth rate from 0.47 to 0.23 ML/s. Other growth conditions are unchanged with an optimized Q1.27 cap layer thickness of 0.3 nm and annealing temperature of 530 ˚C. The number of SL periods is 5. With decrease of the InAs amount and growth rate the ordering of the QD arrays is improved, as shown in Fig. 5 (a) to (e). The reduction of the InAs amount mainly lowers the QD height and diameter to further reduce excess strain accumulation while the decreasing InAs growth rate improves the uniformity of the QD arrays which is attributed to enhancement of the In adatom surface migration length.

In the SL template, the critical thickness for InAs QD formation is less than that on bare InGaAsP surfaces and the InAs QDs are larger due to the strain correlated stacking. Therefore, reduction of the InAs amount in the SL template maintains a high QD density while excess strain accumulation is further suppressed to create straight QD arrays without bends and branches and to reduce the probability of multiple QD arrays formation and QD coalescence.

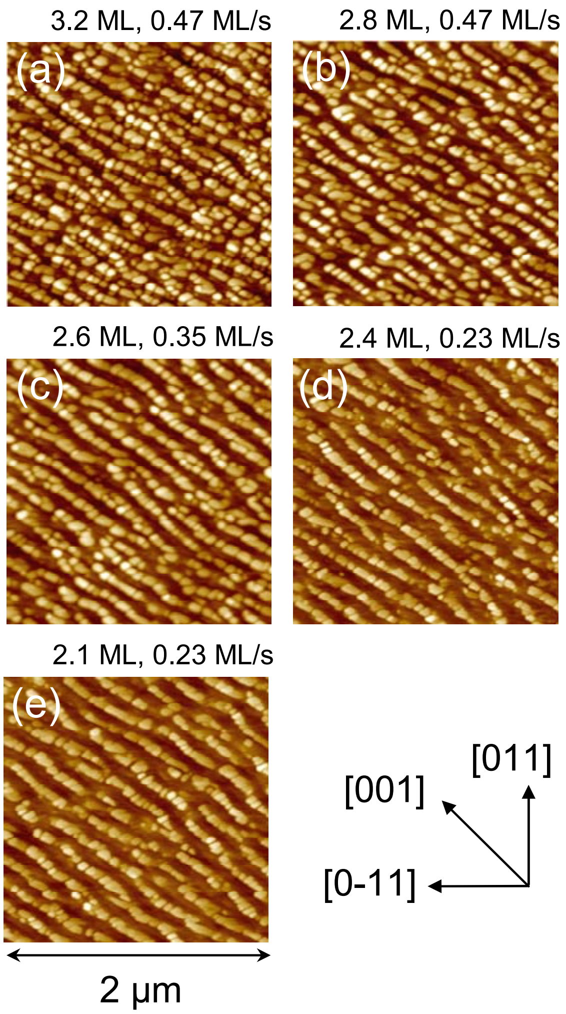

Figure 5 (a)-(e) AFM images of uncapped 2.1-3.2 ML InAs QD arrays on the 5-periods 2.1-3.2 ML InAs/ 0.3 + 15.3 nm Q1.27 SL template (annealing temperature 530 ˚C) with InAs amount and growth rate of (a) 3.2 ML and 0.47 ML/s, (b) 2.8 ML and 0.47 ML/s, (c) 2.6 ML and 0.35 ML/s, (d) 2.4 ML and 0.23 ML/s, and (e) 2.1 ML and 0.23 ML/s. The scan field is 2.0 × 2.0 μm^2 and the height contrast is 20 nm.

4.3.4 Number of SL Periods

In the series of samples shown in Fig. 6 the number of SL periods is changed between 5 and 11 to fully optimize QD ordering. Other growth conditions are unchanged with an optimized Q1.27 cap layer thickness of 0.3 nm, annealing temperature of 530 ˚C, 2.1 ML InAs amount, and 0.23 ML/s InAs growth rate. The amount of InAs for QD formation on the SL template surface is 2.6 ML which slightly increases the QD height. The average QD arrays height, diameter, and periodicity for QD grown on 5 SL periods is 7.31 ± 1.32 nm, 73.36 ± 11.06 nm, and 171.57 ± 14.55 nm [Fig. 6 (a)], for 7 SL periods is 8.95 ± 1.28 nm, 96.12 ± 12.20 nm, and 154.47 ± 21.31 nm [Fig. 6 (b)], for 9 SL periods is 10.21 ± 1.35 nm, 106.28 ± 10.09 nm, and 169.71 ± 14.03 nm [Fig. 6 (c)], and for 11 SL periods is 9.98 ± 1.66 nm, 104.00 ± 10.07 nm, and 185.17 ± 18.02 nm [Fig. 6 (d)], respectively

With increase of the number of SL periods from 5 to 7 (Fig. 6 (a) and (b)), the QD ordering improves further due to the evolution of the self-organizing process during stacking. Accompanied with the increasing strain accumulation the QDs become larger. No significant improvement is observed when the number of SL periods is increased from 9 to 11 revealing the stability of the SL template. However, the QDs within the arrays become more connected, as depicted in Fig. 6 (c) and (d), most probably due to a deeper lateral strain field modulation.

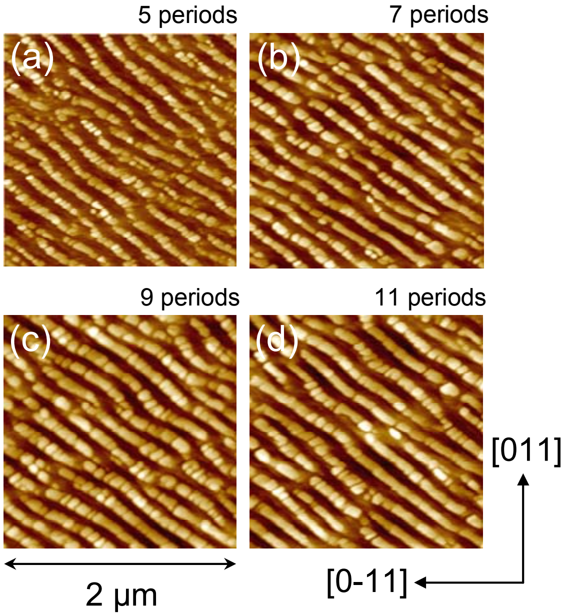

Figure 6 (a)-(d) AFM images of 2.6 ML InAs QD arrays on the 2.1 ML InAs/ 0.3 + 15.3 nm Q1.27 SL template (InAs growth rate 0.23 ML/s, annealing temperature 530 °C) with number of SL periods of (a) 5, (b) 7, (c) 9, and (d) 11. The scan field is 2.0 × 2.0 μm^2 and the height contrast is 20 nm.

4.3.5 SL Template Surface and GaAs Interlayer

The surface of the optimized SL template providing the highest degree of QD ordering is shown in Fig. 7 (a). The number of SL periods is 7. The surface of the SL template shows a very shallow height modulation with mounds elongated along [001] and a lateral periodicity of 130 – 180 nm, corresponding to the lateral periodicity of the QD arrays. This shallow height modulation is superimposed on the typical height modulation extending over micrometer length scales, shown in Fig. 7 (b). Hence, though the SL template surface does not perfectly planarize, the small height modulation of only 0.7 – 1.0 nm, corresponding to 3.0 – 4.0 ML, excludes QD ordering due to preferential nucleation at multilayer high step edges formed due to step bunching. This is further confirmed by the unchanged lateral periodicity of the QD arrays as function of the number of SL periods, i.e., layer thickness and substrate miscut, discussed above, which both would affect the lateral periodicity of multilayer high steps.

For QD arrays with PL emitting in the 1.55 μm wavelength region a 0.8 ML GaAs interlayer is inserted beneath the QDs on the SL template surface. The GaAs interlayer does not affect the QD ordering, as shown in Fig. 7 (c). The role of the GaAs interlayer is to suppress As/P exchange during InAs growth, described earlier in the previous Chapter, to reduce the QD height from 7 – 11 nm to 4 – 5 nm and, therefore, the emission wavelength from far above 1.6 μm at RT into the 1.55 μm region [9,10].

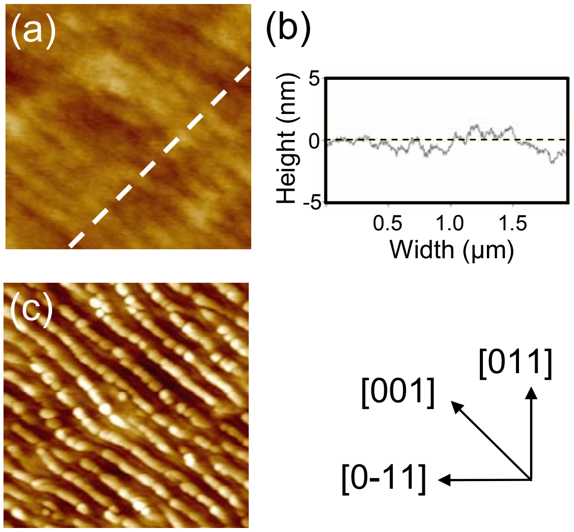

Figure 7 (a) AFM image of the 7 periods 2.1 ML InAs/ 0.3 + 15.3 nm Q1.27 optimized SL template surface (InAs growth rate 0.23 ML/s, annealing temperature 530 ˚C). (b) AFM line scan along [010] of the SL template surface, as indicated in (a). (c) AFM image of the uncapped 2.6 ML InAs QD arrays on the optimized SL template with 0.8 nm GaAs interlayer inserted beneath the QD arrays. The scan field is 2.0 × 2.0 μm^2 and the height contrast is 10 nm.

4.4 Optical Properties of Linear QD Arrays

4.4.1 Temperature Dependence

Fig. 8 shows the PL spectra taken at 4.8 K and RT of the capped InAs QD arrays on the optimized SL template with GaAs interlayer and of the SL template without QDs on top for reference. The PL spectrum measured at 4.8 K reveals a PL peak of the QD arrays at 1475 nm and of the SL template at 1379 nm. The PL peak of the QD arrays at RT is red-shifted to 1548 nm with a shoulder at the short wavelength side stemming from the SL template which reveals a PL peak at 1478 nm. The PL efficiency drops by about three orders of magnitude between 4.8 K and RT. The differences in PL intensity as well as the linewidth between the QD arrays and SL template sample are due to the different cap layer since the QD arrays are capped with Q and InP while SL template is uncapped.

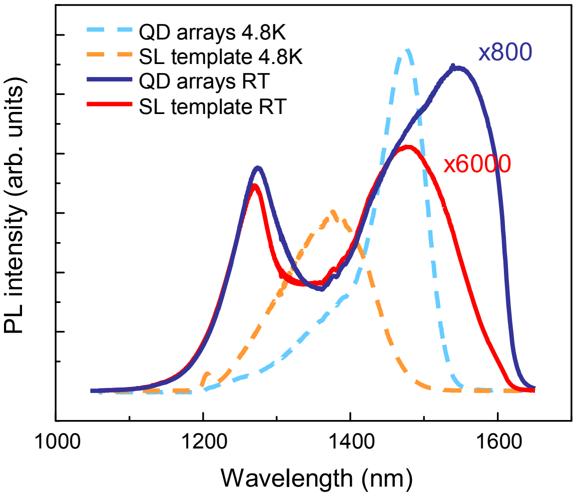

Figure 8 PL spectra of the capped 2.6 ML InAs QD arrays on the optimized SL template and bare SL template without QD arrays taken at 4.8 K and room temperature

The temperature dependences of the PL peak energy and FWHM of the InAs QD arrays is plotted in Fig. 9 (a) and those of a single InAs QD layer grown on a bare 100-nm Q1.27 layer in Fig. 9 (b) for comparison. InAs amount and growth rate of 2.6 ML and 0.23 ML/s are the same for both cases. The QD arrays reveal a PL peak energy which follows closely the bandgap energy dependence and a FWHM which monotonically increases with temperature. On the other hand, the PL peak energy of the single QD layer reveals an increased low-energy shift exhibiting strong “S” shape-like dependence in the temperature range of 100 – 200 K which is accompanied by a pronounced minimum of the FWHM. This behavior is typical for inhomogeneous QD ensembles due to thermally activated carrier redistribution in this temperature range preferentially from smaller (higher energy) to larger (lower energy) QDs and the equilibration of the carrier distribution at higher temperatures [1,2]. The much less evident thermally activated carrier redistribution in the QD arrays is a first indication of lateral electronic coupling of the closely-spaced QDs within the arrays allowing carrier redistribution independent on the temperature by providing a quasi-continuous density of states such as in quantum wires. A small degree of carrier localization accounts for the small deviation of the PL peak energy and the small plateau in the FWHM around 150 K.

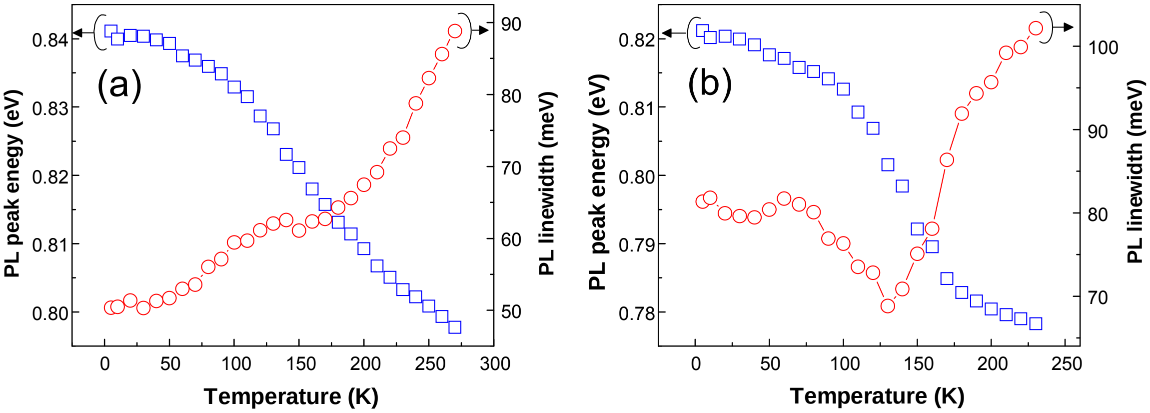

Figure 9 (a) Temperature dependences of the PL peak energy and PL linewidth of the capped 2.6 ML InAs QD arrays with 0.8 ML GaAs interlayer on the optimized SL template and (b) of the capped 2.6 ML single InAs QD layer on 100 nm Q1.27 for a reference.

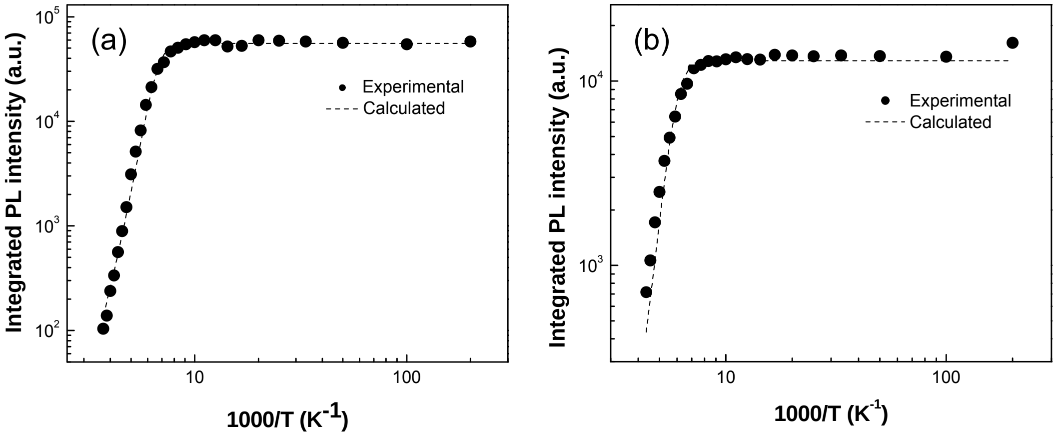

Figure 10 (a) Temperature dependence of the integrated PL intensity of the capped 2.6 ML InAs QD arrays with 0.8 ML GaAs interlayer on the optimized SL template, and (b) of the capped 2.6 ML single InAs QD layer on 100-nm Q1.27. The dashed lines are exponential fits with thermal activation energy of (a) 183 meV and (b) 197 meV.

The integrated PL intensity of both the QD arrays and single QD layer, shown in Fig. 10 (a) and (b), is roughly constant up to 130 K, and exponentially decreases at higher temperature due to thermal quenching. The activation energy of the PL quenching is derived by fitting the integrated PL intensity to:

$$I_{PL} = C/(1+A\exp(-E_a/(k_B T))),$$

where k_B is the Boltzmann constant, T is the temperature, and A and C are the fitting parameters. The activation energy is 183 meV for the QD arrays and 197 meV for the single QD layer. This is consistent with the energy difference of the QD ground state energy and the Q1.27 barrier bandgap energy, which is 188 meV for the QD arrays and 203 meV for the single QD layer. Hence, the thermal quenching of the PL intensity is due to thermally activated escape of carriers from the QDs into the Q1.27 barrier. This reveals the absence of non-radiative recombination centers in the QDs contributing to the thermal quenching, evidencing the excellent optical and structural quality of the InAs QD arrays similar to single layers of QDs.

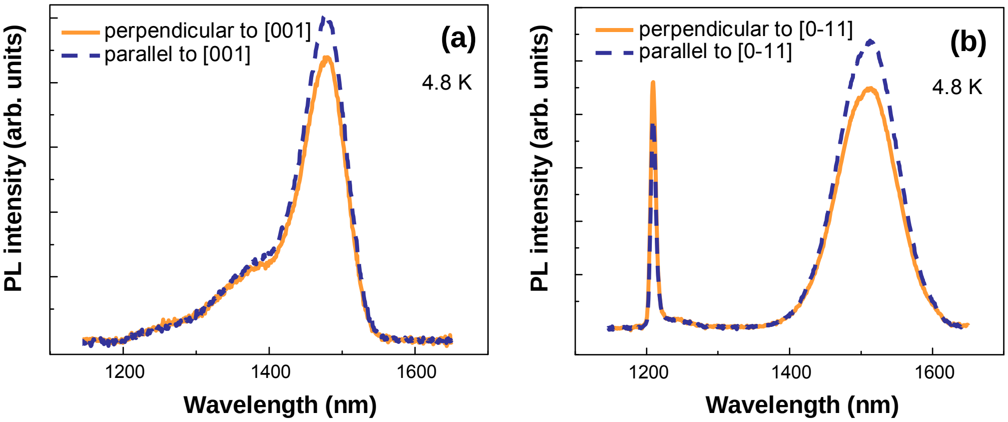

Figure 11 Linear polarization dependent PL spectra taken at 4.8 K of (a) the capped 2.6 ML InAs QD arrays with 0.8 ML GaAs interlayer on the optimized SL template, and (b) of the capped 2.6 ML single InAs QD layer on 100-nm Q1.27. The PL is polarized along [001] in (a) and along [01-1] in (b).

4.4.2 Polarization Dependence

The linear polarization-dependent PL spectra taken from the sample surface of the QD arrays and single QD layer are shown in Fig. 11 (a) and (b). The PL of the QD arrays is polarized along [001], i.e., along the array direction, with a degree of linear polarization $P = (I_{//}-I_{\perp})/(I_{//}+I_{\perp})$ at the PL peak position of 6.46. $I_{//}$ and $I_{\perp}$ denote the PL intensities with polarization parallel and perpendicular to [001]. On the other hand, the PL of the single QD layer is polarized along [0-11] with a degree of linear polarization at the PL peak position of 8.97. This is typical for isolated, randomly arranged QDs which often exhibit a slight elongation along [0-11], which is the direction of long adatom surface diffusion length related to the surface reconstruction. The rotated linear polarization of the QD arrays is attributed to the rotation of the long axis of the QDs in the array direction and is a further indication of lateral electronic coupling of the QDs in the arrays.

4.5 Summary

We have realized linear InAs quantum dot (QD) arrays based on self-organized anisotropic strain engineering of an InAs/InGaAsP superlattice (SL) template on InP (100) in chemical beam epitaxy (CBE) and determined the optimized growth conditions for ordering. During SL template formation, InAs QD growth, thin InGaAsP capping, annealing, InGaAsP overgrowth, and stacking produces wire-like InAs structures due to anisotropic surface migration and lateral and vertical strain correlation. InAs QD ordering is governed by the lateral strain field modulation which builds up during SL template formation. The presence of linear QD arrays depends on the substrate miscut altering the adatom surface migration. The optimum substrate miscut is 2° towards (110) for which the InGaAsP cap layer thickness, annealing temperature, InAs amount and growth rate, and number of SL periods are optimized for the formation of straight and well-separated arrays along [001]. The InAs QD arrays exhibit excellent photoluminescence (PL) emission up to room temperature which is tuned into the 1.55-μm telecom wavelength region through the insertion of ultra-thin GaAs interlayers. Temperature dependent PL measurements indicate lateral electronic coupling of the QDs in the arrays which is supported by the linear polarization of the PL along the arrays.

Bibliography

[1] T. Mano, R. Nötzel, Q. Gong, T. van Lippen, G. J. Hamhuis, T. J. Eijkemans, and J. H. Wolter, *Jpn. J. Appl. Phys.* **44**, 6829 (2005).

[2] Y. I. Mazur, B. L. Liang, Zh. M. Wang, G. G. Tarasov, D. Guzun, and G. J. Salamo, *J. Appl. Phys.* **101**, 014301 (2007).

[3] V. A. Shchukin, N. N. Ledentsov, P. S. Kop'ev, and D. Bimberg, *Phys. Rev. Lett.* **75**, 2968 (1995).

[4] V. A. Shchukin and D. Bimberg, *Rev. Mod. Phys.* **71**, 1125 (1999).

[5] T. Mano, R. Nötzel, D. Zhou, G. J. Hamhuis, T. J. Eijkemans, and J. H. Wolter, *J. Appl. Phys.* **97**, 014304 (2005).

[6] A. Stintz, T. J. Rotter, and K. J. Malloy, *J. Crystal Growth* **255**, 266 (2003).

[7] O. Bierwagen and W. T. Masselink, *Appl. Phys. Lett.* **86**, 113110 (2005).

CHAPTER 5

Two-Dimensional Periodic Square Lattice of InAs/ InP Quantum Dot Arrays

ABSTRACT

The formation of two-dimensional InAs quantum dot (QD) arrays by self-organized anisotropic strain engineering of InAs/InGaAsP superlattice (SL) templates on InP (311)B substrates by chemical-beam epitaxy (CBE) is demonstrated. The SL template and InAs QD growth conditions are studied in detail for optimized QD ordering. Excellent photoluminescence emission up to room temperature is achieved from buried QD arrays. The emission wavelength is tuned from above 1.9 µm to the 1.55 µm telecom wavelength region through the insertion of ultrathin GaAs interlayers beneath the QD arrays.[1]

---

[1] These results have been published as: *Formation of two-dimensional InAs quantum dot arrays by self-organized anisotropic strain engineering on InP (311)B substrates*, N. Sritirawisarn, F. W. M. van Otten, P. E. D. Soto Rodriguez, J. L. E. Wera, and R. Nötzel, J. Crystal Growth **312**, 164 (2010).

5.1 Introduction

In the previous chapters we have introduced self-organized anisotropic strain engineering of strained superlattice (SL) templates for the lateral ordering of one-dimensional (1-D) linear InAs QD arrays on planar (100) oriented InP substrates by chemical-beam epitaxy (CBE). To extend the concept, in this Chapter, we demonstrate the formation of periodic two-dimensional (2-D) InAs QD arrays on InP (311)B substrates by self-organized anisotropic strain engineering of InAs/InGaAsP SL templates in CBE. SL template formation comprises InAs QD formation, thin InGaAsP capping, post-growth annealing, InGaAsP overgrowth, and stacking. Due to distinct anisotropic adatom surface migration during annealing and vertical and lateral strain correlations during stacking, the SL template self-organizes into a 2-D ordered strain modulated mesalike network on a mesoscopic length scale. InAs QDs preferentially nucleate on top of the network nodes due to local strain recognition. The SL template and InAs QD growth parameters, such as InAs amount, InAs growth rate, InGaAsP cap layer thickness, annealing temperature, and number of SL periods are studied in detail for optimized QD ordering. Excellent photoluminescence (PL) emission up to room temperature (RT) is achieved from buried QD arrays. The PL emission is tuned from above 1.9 µm to the 1.55-µm wavelength region, either at low temperature or RT, through the insertion of ultrathin GaAs interlayers with increasing coverage beneath the InAs QD arrays. These highly uniform QD arrays, thus, provide the basis for the development of future quantum functional devices operating at telecom wavelengths.

Section 5.2 describes the experimental and characterization details. The main results are presented in section 5.3 regarding the optimization of uniform 2-D InAs/InP QD arrays. The PL and wavelength emission tuning are discussed in section 5.4. Finally, section 5.5 summarizes the chapter.

5.2 Experimental Details

The samples were grown by CBE using pressure controlled trimethylindium (TMI), triethylgallium (TEG), AsH_3, and PH_3 as precursors. The AsH_3 and PH_3 gases were thermally decomposed in a high temperature injector at 900 ˚C. The semi-insulating InP (311)B substrates were mounted by In on Mo blocks. The sample structure commenced with a 200 nm InP buffer layer and 100 nm lattice-matched InGaAsP with RT band gap at 1.18 µm (Q1.18). The V/III ratio was 2.7 for InP and 2.9 for Q1.18 growth. Each period of the SL template grown then consisted of 2.1 monolayers (ML) InAs, 10 s growth interruption under As flux, a 0.2 – 0.4 nm thin Q1.18 cap layer, 2 min annealing at 514-520 ˚C, and a 5.5 nm Q1.18 separation layer. The number of SL periods was between 3 and 11 in different samples. On top of the SL template a 0 – 2 ML GaAs interlayer and a 3.2 ML InAs QD layer were grown for atomic force microscopy (AFM) measurements. The growth temperature was kept constant at 505 ˚C throughout the entire structure. The growth and annealing temperatures were determined by a pyrometer. They were stable and reproducible within 1 ˚C, which was additionally confirmed and monitored by the stability and reproducibility of the composition of the quaternary layers from sample to sample and very recently by employing the kSA BandiT system measuring the temperature dependent absorption edge of the substrate. The InAs growth rate was varied from 0.09 ML/s to 0.73 ML/s, calibrated by high-resolution x-ray diffraction (XRD). For PL measurements the InAs QDs were buried by 100 nm Q1.18 and 50 nm InP. The PL was excited by the 532 nm line of a neodymium-doped yttrium aluminum garnet (Nd:YAG) laser with power density of 256 mW/cm^2. The samples were mounted in a He-flow cryostat with temperature control between 4.8 K and RT. The PL was dispersed by a single monochromator and recorded by a liquid nitrogen cooled InGaAs linear array detector or a single channel InSb detector.

5.3 Formation of 2-D InAs QD Arrays

5.3.1 Optimized Growth Conditions

For a better understanding we will first discuss the optimized 2-D InAs QD arrays before, in the following paragraphs, we detail the growth conditions to arrive at these QD arrays and their optical properties. Figure 1 (a) shows the AFM image of the optimized QD arrays on the SL template with 2.1 ML InAs amount, 0.18 ML/s InAs growth rate, 10 s growth interruption under As flux, 0.3 nm Q1.18 cap layer thickness, 2 min annealing at 514 ˚C, 5.5 nm Q1.18 separation layer thickness, and number of SL periods of 9. The amount of InAs for QD formation on the SL template is 3.2 ML. Clear ordering of large InAs QDs in a 2-D network aligned along ±45˚ off [-233] is observed. The QDs have diameters and heights of 98.59 ± 7.65 nm and 20.45 ± 2.33 nm, respectively. The lateral periodicity of the QD arrays in the directions ±45˚ off [-233] is 200.59 ± 35.70 nm which is in agreement with the value extracted from the 2-D fast-Fourier transform analysis of 202 nm, shown in Fig. 1 (b). Nucleation of the large QDs on the SL template nodes is confirmed in Fig. 1 (c) showing the AFM image of the bare SL template surface with shallow mounds of the same periodicity as that of the large QDs and heights of 5.95 ± 1.24 nm. Clear faceting of the QDs is shown in the zoomed-in AFM image in the inset of Fig. 1 (a). The faceting is similar to that observed for InAs QDs on GaAs (311)B substrates, reflecting the symmetry of the (311)B surface [1]. In between the large QDs, dense small QDs with a more round shape having diameters and heights of 48.48 ± 4.64 nm and 8.43 ± 1.55 nm, respectively, are found.

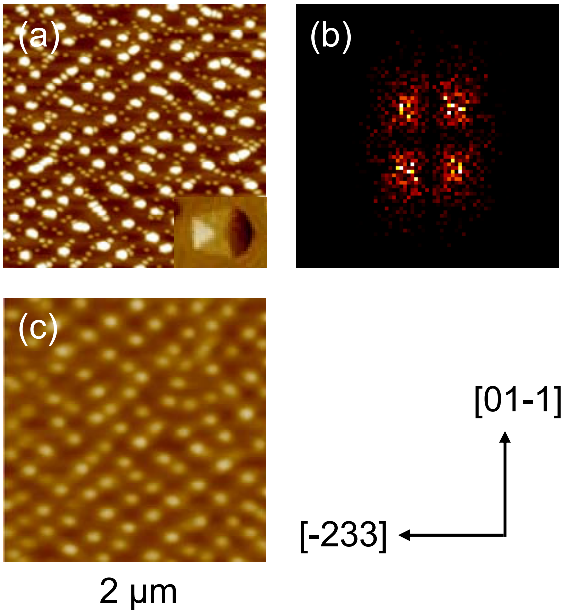

Figure 1 (a) AFM image of uncapped 3.2 ML InAs QD arrays on the optimized nine-periods InAs/Q1.18 SL template (2.1 ML InAs amount, 0.18 ML/s InAs growth rate, 0.3 nm Q1.18 cap layer thickness. 514 ˚C annealing temperature, 5.5 nm Q1.18 separation layer thickness) on InP (311)B substrate. Inset: zoomed-in AFM image of an individual InAs QD. (b) Two-dimensional fast-Fourier transform analysis of (a). (c) AFM image of the optimized nine-periods InAs/Q1.18 SL template surface. The scan fields are 2.0 × 2.0 μm^2 and the height contrast is 30 nm for (a) and (c).

The formation of the ordered large QDs is obviously due to local strain recognition on top of the SL template nodes while the formation of the small QDs in between is more likely due to strain-driven growth instability similar to the case of InGaAs QDs on InGaAs/GaAs SL templates on GaAs (311)B. For the relatively small and comparable lattice mismatch of InAs/InP (311)B or InGaAs/GaAs (311)B strain-driven growth instability leads to a continuous InAs or InGaAs layer with nanoscale surface modulations growing continuously in height with thickness in contrast to QD nucleation in the S-K growth mode observed for InAs/GaAs (311)B with larger mismatch, as discussed previously in section 2.6.2.

5.3.2 Thin Cap Layer Thickness and Annealing Temperature

In the series of samples shown in Fig. 2, the thickness of the thin Q1.18 cap layer in the SL template is varied between 0.2 and 0.4 nm and the annealing temperature between 514 and 520 ˚C. The InAs amount of 2.1 ML, 0.18 ML/s InAs growth rate, 5.5 nm Q1.18 separation layer thickness, and number of SL periods of 9 are kept constant. The amount of InAs for QD formation on the SL template surface is 3.2 ML.

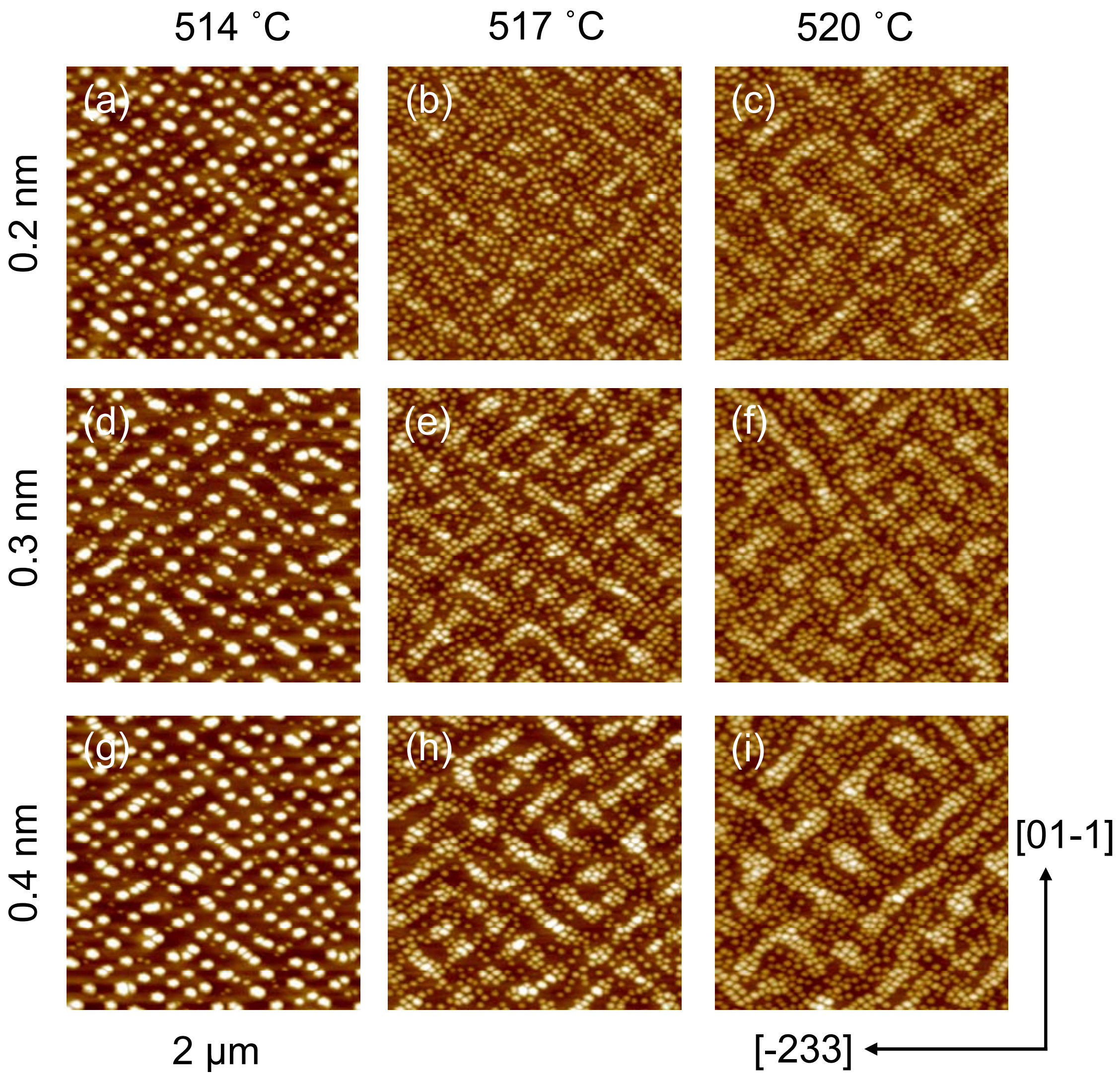

Figure 2 (a)-(i) AFM images of uncapped 3.2 ML InAs QD arrays on nine-periods InAs/Q1.18 SL templates (2.1 ML InAs amount, 0.18 ML/s InAs growth rate, 5.5 nm Q1.18 separation layer thickness) on InP (311)B substrates with Q1.18 cap layer thickness of 0.2 to 0.4 nm and annealing temperature of 514 to 520 ˚C. The scan fields are 2.0 × 2.0 µm^2 and the height contrast is 30 nm.

Clear ordering of the InAs QDs in a 2-D network is observed for 0.2 to 0.4 nm cap layer thickness with an annealing temperature of 514 ˚C, as illustrated in Figs. 2 (a), (d), and (g). Outside this growth window the ordering gradually disappears leaving a modulated layer of small QDs. The optimized condition for 2-D QD ordering is shown in Fig. 2 (d) with 0.3 nm Q1.18 cap layer thickness and 514 ˚C annealing temperature. The cap layer thickness and annealing temperature balance In desorption during annealing for optimized ordering in similar manner as for the formation of 1-D InAs/InP QD arrays on InP (100) substrates, discussed in Chapter 4.

For too low annealing temperature and too thick cap layer In desorption is insufficient resulting in excess strain accumulation during stacking which leads to a high density of relatively large QDs with less degree of ordering which is even worsened due to suppressed lateral mass transport during annealing. On the other hand, for too high annealing temperature and too thin cap layer, In desorption is too large to maintain vertical strain correlation. The QD ordering gradually vanished with increase of the annealing temperature from the optimum 514 ˚C [Figs. 2 (a), (d), and (g)] to 517 ˚C [Figs. 2 (b), (e), and (h)] and 520 ˚C [Figs. 2 (c), (f), and (i)]. The influence of the cap layer thickness on In desorption, however, is not as strong as that of the annealing temperature. Very little difference in ordering is observed for annealing at 514 ˚C when the cap layer thickness is varied from 0.2 to 0.4 nm as shown in Figs. 2 (a), (d), and (g) and the QD ordering only slightly degrades for annealing at 517 ˚C [Figs. 2 (b), (e), and (h)] and 520 ˚C [Figs. 2 (c), (f), and (i)] with reduction of cap layer thickness from 0.4 to 0.2 nm.

5.3.3 Number of SL Periods

In the series of samples shown in Fig. 3, the number of SL periods is varied between 3 and 11. The other optimized growth conditions are unchanged with 2.1 ML InAs amount, 0.18 ML/s InAs growth rate, 0.3 nm Q1.18 cap layer thickness, 514 ˚C annealing temperature, and 5.5 nm Q1.18 separation layer thickness. The amount of InAs for QD formation on the SL template is 3.2 ML. The average dot height and diameter for QD arrays grown on 3 SL periods is 16.81 ± 1.30 nm and 93.37 ± 8.92 nm [Fig. 3 (a)], for 5 SL periods is 17.57 nm ± 1.95 nm and 90.05 ± 6.32 nm [Fig. 3 (b)], for 7 SL periods is 19.95 ± 2.68 nm and 92.35 ± 8.85 nm, for 9 SL periods (reference sample) is 20.45 ± 2.33 nm and 98.59 ± 7.65 nm, and for 11 SL is 16.39 ± 2.65 nm and 95.21 ± 9.60 nm, respectively

With increase of the number of SL periods from 3 to 9 [Figs. 3 (a) to (d)], the QD ordering improves significantly. Upon stacking, the nanoscale 2-D InAs surface modulation for the first SL period evolved into the distinct mesoscopic mesalike arrangement when the number of SL periods is increased due to anisotropic surface migration during annealing and strain-correlation during stacking. Accompanied with the increasing strain accumulation, the QDs following the mesalike arrangement become larger with small QDs in between, as seen for the optimized 9 periods SL template in Fig. 3 (d). However, when the number of SL periods is increased from 9 to 11 the QD ordering degrades with a higher density of large QDs, shown in Fig. 3 (e), which is attributed to excess strain accumulation causing overlap of the lateral strain field modulations.

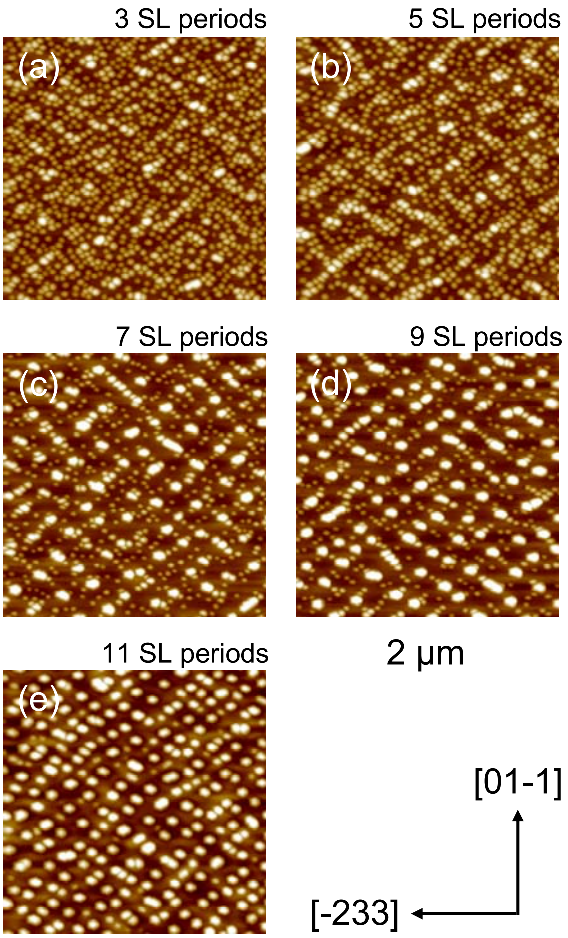

Figure 3 (a)-(e) AFM images of uncapped 3.2 ML InAs QD arrays on InAs/Q1.18 SL templates (2.1 ML InAs amount, 0.18 ML/s InAs growth rate, 0.3 nm Q1.18 cap layer thickness, 514 ˚C annealing temperature, 5.5 nm Q1.18 separation layer thickness) on InP (311)B substrates with number of SL periods of 3 to 11. The scan fields are 2.0 × 2.0 μm^2 and the height contrast is 30 nm.

5.3.4 InAs Growth Rate

In the series of samples shown in Fig. 4, the InAs growth rate is changed from 0.73 to 0.09 ML/s. The other growth conditions are unchanged with an optimized amount of InAs of 2.1 ML, 0.3 nm Q1.18 cap layer thickness, 514 ˚C annealing temperature, and number of SL periods of 9. The amount of InAs for QD formation on the SL template is 3.2 ML. It is noted that the InAs growth rate is changed also for the top InAs QD layer.

For relatively high InAs growth rate between 0.73 and 0.36 ML/s QD ordering is hardly observed. A high density of relatively large QDs forms, as shown in Figs. 4 (a) to (c), resembling the QD formation on the 11 periods SL template shown in Fig. 3 (e). This is again related to excess strain accumulation for reduced In desorption hindering the QD ordering. When the InAs growth rate is reduced 2-D QD ordering occurs, seen in Fig. 4 (d) for the optimized growth rate of 0.18 ML/s. Further decrease of the InAs growth rate to 0.09 ML/s results in a modulated layer of small QDs, depicted in Fig. 4 (e), similar to that shown in Fig. 2 for 517 and 520 ˚C annealing temperature due to too large In desorption.

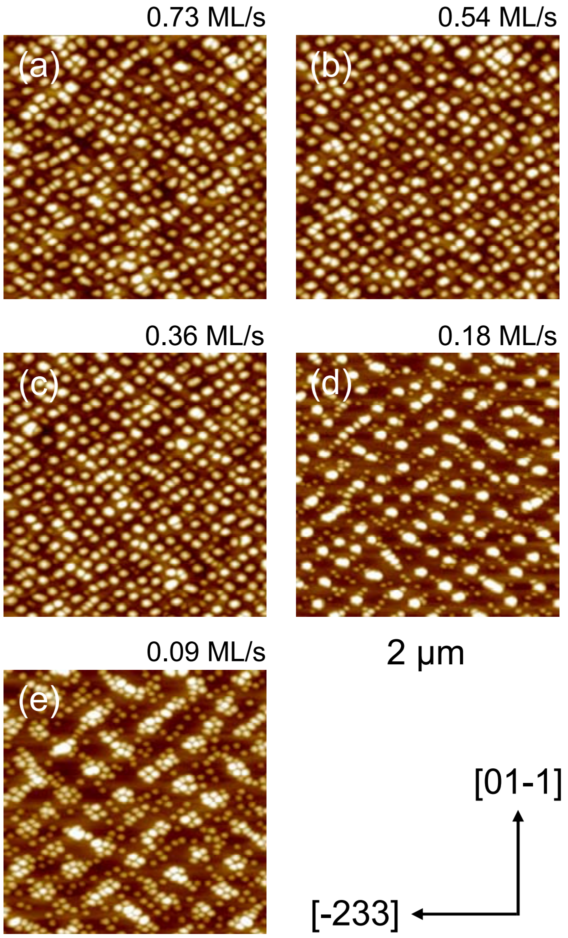

Figure 4 (a)-(e) AFM images of uncapped 3.2 ML InAs QD arrays on nine-periods InAs/Q1.18 SL templates (2.1 ML InAs amount, 0.3 nm Q1.18 cap layer thickness, 514 ˚C annealing temperature, 5.5 nm Q1.18 separation layer thickness) on InP (311)B substrates with InAs growth rate of 0.73 to 0.09 ML/s. The scan fields are 2.0 × 2.0 μm^2 and the height contrast is 30 nm.

5.4 Optical Properties of 2-D InAs QD Arrays

Figure 5 shows the PL spectra taken at 4.8 K and RT of the capped InAs QD arrays on the optimized SL template and of the SL template without QDs on top for reference. At 4.8 K, the PL peak of the QD arrays is at 1783 nm and that of the SL template is at 1377 nm. The PL peak of the small QDs is observed at 1487 nm and that of the Q1.18 barrier at 1127 nm with weak intensity. The PL peak of the InAs QD arrays at RT is red shifted to 1905 nm with a shoulder at the short-wavelength side stemming from the small QDs and the SL template, the latter revealing a PL peak at 1533 nm at RT. It is noted that the PL peak energy varies at most 5-10 nm across the wafer surface reflecting good homogeneity of the QD arrays over macroscopic areas.

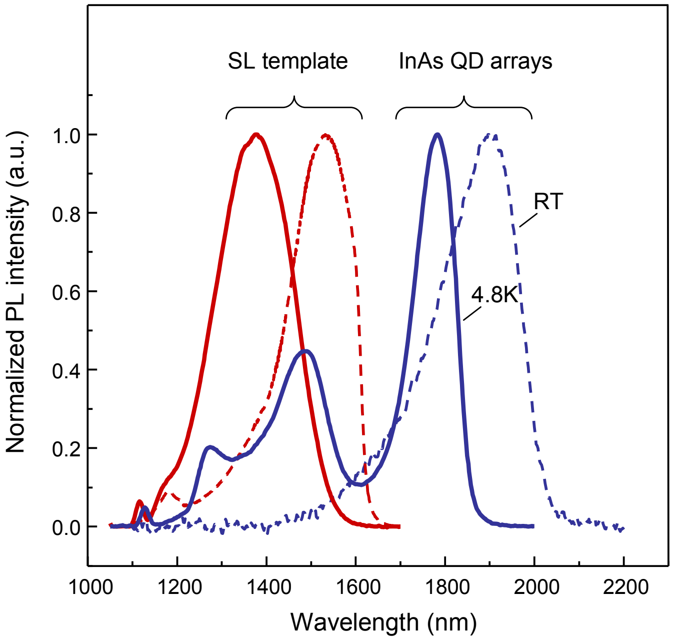

Figure 5 PL spectra of capped 3.2 ML InAs QD arrays on the optimized nine-periods InAs/Q1.18 SL template on InP (311)B substrate taken at 4.8 K (blue solid line) and RT (blue dashed line) and of the optimized nine-periods InAs/Q1.18 SL template on InP (311)B substrate taken at 4.8 K (red solid line) and RT (red dashed line).

To tune the emission from the QD arrays into the 1.55 μm wavelength region, a GaAs interlayer is inserted beneath the QDs. The GaAs interlayer suppresses As/P exchange during InAs growth to reduce the QD height and, hence, emission wavelength, described in Chapter 3. The AFM images of the InAs QD arrays with 1.0 and 2.0 ML GaAs interlayers are shown in Figs. 6 (a) and (b). The QD height is decreased to 8.29 ± 1.47 nm for 1.0 ML GaAs interlayer and to 6.40 ± 1.16 nm for 2.0 ML GaAs interlayer. For the reduced QD height, faceting is not observed and the QDs are more round shaped. The GaAs interlayer does not affect the QD ordering, however, it suppresses the formation of the small QDs in between the large QDs most probably also due to the reduction of As/P exchange during InAs growth.

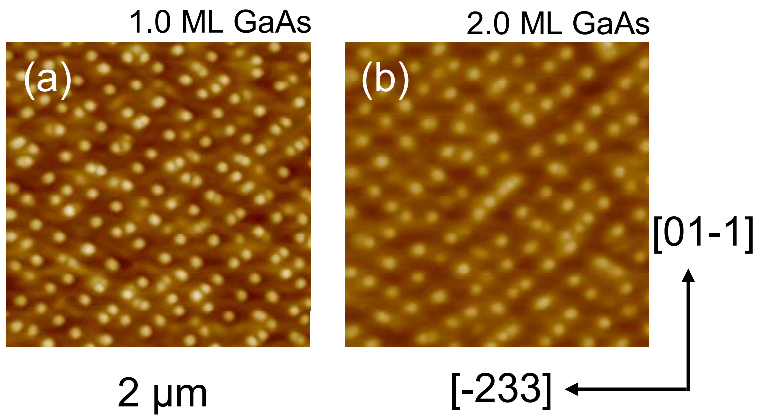

Figure 6 AFM images of uncapped 3.2 ML InAs QD arrays on the optimized nine-periods InAs/Q1.18 SL templates on InP (311)B substrates with coverage of the GaAs interlayer inserted beneath the InAs QD arrays of (a) 1.0 and (b) 2.0 ML. The scan fields are 2.0 × 2.0 μm^2 and the height contrast is 30 nm.

Figure 7 shows the low temperature and RT PL spectra of the InAs QD arrays with 1.0 and 2.0 ML GaAs interlayers. The RT PL peak is at 1672 nm for 1.0 ML and at 1581 nm for 2.0 ML GaAs interlayers while at 4.8 K the PL peak is at 1555 nm and 1504 nm for 1.0 ML and 2.0 ML GaAs interlayers, respectively. Hence, the emission wavelength is tuned into the 1.55 µm region at RT for a 2.0 ML GaAs interlayer and at low temperature for a 1.0 ML GaAs interlayer. The inset in Fig. 7 shows the dependence of the RT PL peak wavelength on the GaAs interlayer coverage. No PL from small QDs is observed in agreement with the morphological investigations. The small PL peaks at low temperature at shorter wavelengths are from the SL template. The PL efficiency drops by about one order of magnitude (for InAs QD arrays without GaAs interlayer) and two orders of magnitude (for InAs QD arrays with 1.0 and 2.0 ML GaAs interlayers) between 4.8 K and RT, typical for thermal activation of carriers out of the QDs into the Q1.18 barriers.

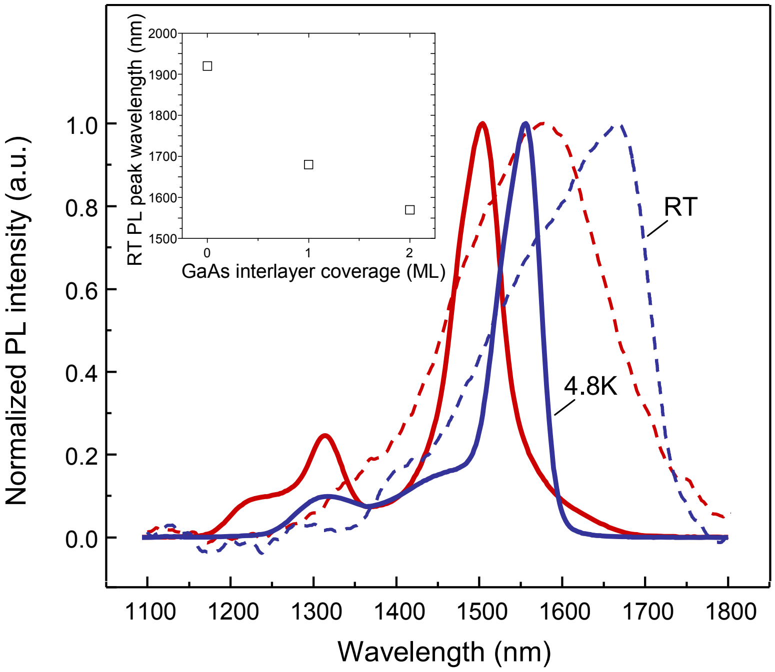

Figure 7 PL spectra of capped 3.2 ML InAs QD arrays on the optimized nine-periods InAs/Q1.18 SL templates on InP (311)B substrates with 1.0 ML GaAs interlayer inserted beneath the InAs QD arrays taken at 4.8 K (blue solid line) and RT (blue dashed line) and with 2.0 ML GaAs interlayer inserted beneath the InAs QD arrays taken at 4.8 K (red solid line) and RT (red dashed line). Inset: RT PL peak wavelength as a function of the GaAs interlayer coverage.

5.5 Summary

In conclusion, we have realized laterally ordered two-dimensional InAs quantum dot (QD) arrays by self-organized anisotropic strain engineering of InAs/InGaAsP superlattice (SL) templates on InP (311)B substrates by chemical-beam epitaxy (CBE). The SL template, comprising InAs QD growth, thin InGaAsP capping, annealing, InGaAsP overgrowth, and stacking self-organizes into a two-dimensionally ordered strain-modulated mesalike network on a mesoscopic length scale due to anisotropic surface migration and strain correlated growth. InAs QDs order on top of the network nodes due to local strain recognition. The SL template and QD growth conditions, such as InAs amount, InAs growth rate, thin InGaAsP cap layer thickness, annealing temperature, and number of SL periods have been varied for optimized InAs QD ordering. The InAs QD arrays exhibited excellent photoluminescence (PL) emission up to room temperature (RT). Tuning of the PL emission into the 1.55 μm telecom wavelength region was achieved, both at low temperature (4.8 K) and RT through the insertion of ultrathin GaAs interlayers with increasing coverage. Such highly ordered QD arrays are the basis for the realization of novel quantum functional devices operating at telecom wavelengths.

Bibliography

[1] T. Suzuki, Y. Temko, and K. Jacobi, *Appl. Phys. Lett.* **80**, 4744 (2002).

CHAPTER 6

Evolution of Ordered 1-D and 2-D InAs/InP Quantum Dot Arrays on Patterned Substrates

ABSTRACT

The formation of ordered InAs/InP quantum dot (QD) arrays is demonstrated on patterned InP (100) and (311)B substrates by the concept of self-organized anisotropic strain engineering in chemical-beam epitaxy (CBE). On shallow- and deep stripe-patterned InP (100) substrates, depending on the stripe orientation, the linear one-dimensional InAs QD arrays are rotated away from their natural direction due to the presence of vicinal stepped sidewall planes modifying the self-organization process, coexisting with QD free steep side facets on the deep-patterned substrates. On shallow- and deep-patterned InP (311)B substrates only QD free side facets form with flat top and bottom areas, not affecting the natural ordering of the two-dimensional InAs QD arrays. On the deep-patterned substrates a row of dense QDs forms on top along the side facets due their slow-growing behavior.[1]

---

[1] These results have been published as: *Evolution of ordered one-dimensional and two-dimensional InAs/InP quantum dot arrays on patterned InP (100) and (311)B substrates by self-organized anisotropic strain engineering*, N. Sritirawisarn, J. L. E. Wera, F. W. M. van Otten, and R. Nötzel, accepted for publication in J. Crystal Growth (2010).

6.1 Introduction

The concept of self-organized anisotropic strain engineering for QD ordering has been extended for formation of more complex architectures of lateral QD arrays, such as bends and branches of linear QD arrays and zigzag arrangements by combining it with step engineering on artificially patterned GaAs (100) and (311)B substrates [1,2], as discussed earlier in Chapter 2. In this Chapter, we study the combination of self-organized anisotropic strain engineering with step engineering on shallow- and deep-patterned InP (100) and (311)B substrates. The key features of the influence of steps with step edges in different directions, determined by the pattern geometry, on the modification of the natural QD ordering are discussed for formation of complex QD arrays and networks needed for future quantum functional devices.

The sample preparation for shallow- and deep-patterned InP (100) and (311)B substrates by conventional photolithography and wet chemical etching is described in section 6.2 and the details of growth and characterization techniques are presented in section 6.3. The main results and discussions are given in section 6.4. Section 6.5 summarizes the chapter.

6.2 Sample Preparation

The following list the steps for the mesa-patterned substrate preparation before loading into the chemical-beam epitaxy (CBE) chamber. The schematic illustration of the preparation steps is summarized in Fig. 1.

1. The substrate is cleaned in an oxygen plasma at 300 W for 10 minutes and etched in diluted $1H_3PO_4 : 10H_2O$ for 2 minutes to remove the oxide layer. The sample is rinsed in ultra-pure water and blown dry with Nitrogen.
2. 50 nm SiN_x layer is deposited by Plasma Enhanced Chemical Vapour Deposition (PECVD) at 300 ˚C.
3. The sample is spin-coated with positive photoresist HPR504 followed by soft bake at 100 ˚C for 2:30 minutes. A conventional photolithographic mask-aligner is used to transfer the patterns from the glass mask onto the sample.
4. After post-exposure bake at 115 ˚C and developing. The sample is hard baked at 120 ˚C for 2 minutes.
5. SiN_x is etched back using Reactive-ion etching (RIE). The left-over photoresist is removed by oxygen plasma at 300 W for 30 minutes.
6. The sample is wet-chemical etched in the $3H_2SO_4$: $1H_2O_2$: $1H_2O$ solution at 25 ˚C to different depths with etching rate of 16.7 ± 0.5 nm/minute for the InP (100) substrate and of 28.7 ± 0.5 nm/minute for the InP (311)B substrate.

7. The SiN_x mask is removed by diluted HF (10%) for 2 minutes.
8. Before loading into the CBE chamber the sample is cleaned with oxygen plasma and the oxide layer is etched in diluted $1H_3PO_4$: $10H_2O$ and rinsed in ultra-pure water for 3 times to ensure the substrate cleanness which excellent morphology is confirmed by AFM measurement.

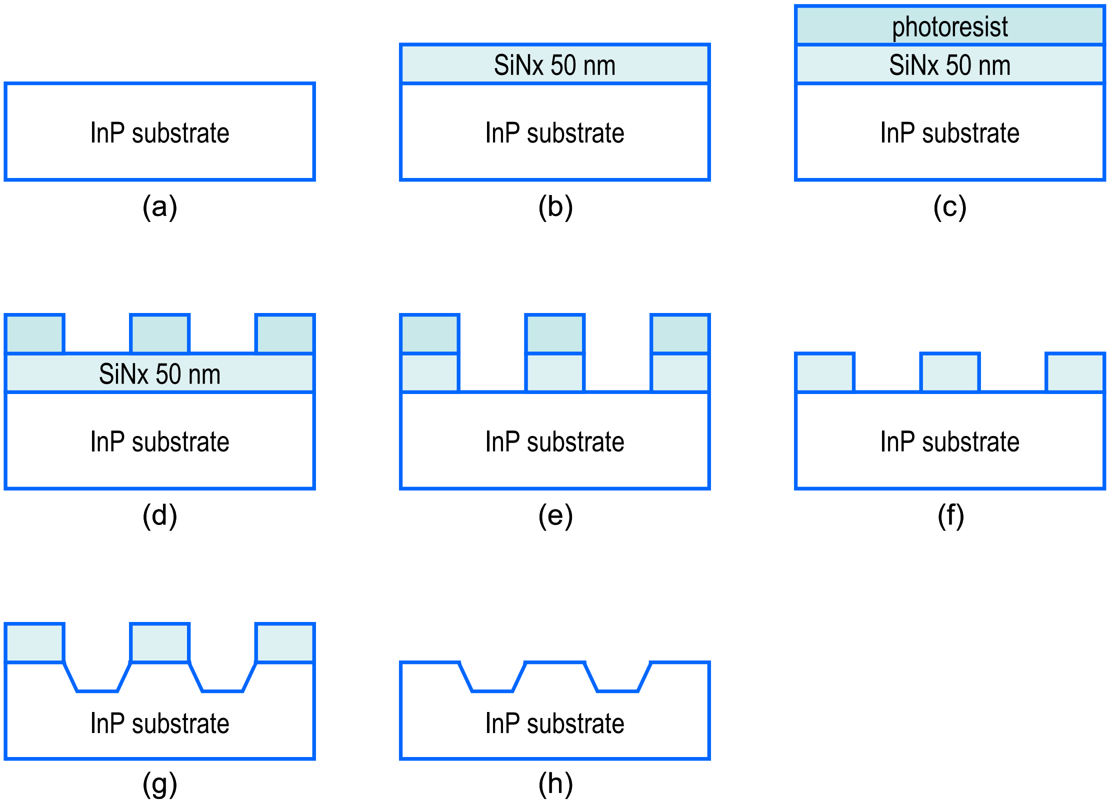

Figure 1 Schematic illustration of steps for sample preparation processes: (a) substrate cleaning, (b) deposition of SiN_x mask, (c) spin-coating of photoresist, (d) standard photolithography and photoresist development, (e) SiN_x etching, (f) photoresist removal, (g) wet-chemical etching of InP substrate, and (h) SiN_x mask removal and substrate cleaning.

6.3 Experimental Details

The samples were grown by chemical-beam epitaxy (CBE) on planar and artificially patterned InP (100) and (311)B substrates. The stripe-, zigzag-, and circular hole-patterned substrates were prepared by optical lithography and wet chemical etching in the H_2SO_4:H_2O_2:H_2O (3:1:1) solution, described in the previous section. For InP (100) substrates with miscut 2° off toward (110), we concentrate on periodic mesa stripes with widths and separations of 4 µm oriented along the four low-index [010], [001], [011], and [0-11] azimuths. The etched mesa depths were 50 and 200 nm. For InP (311)B substrates, we present periodic mesa stripes with widths and separations of 2 µm oriented along [0-11], periodic zigzag patterns with 10 µm widths and sidewalls alternately rotated by ±60° off [0-11], and circular hole patterns with 4 µm diameter. The etched mesa depths were 15 and 200 nm. These patterns were chosen to most clearly show the influence on the QD ordering for shallow- and deep-etched substrates. The schematic overview is given in Fig. 2 (a-c).

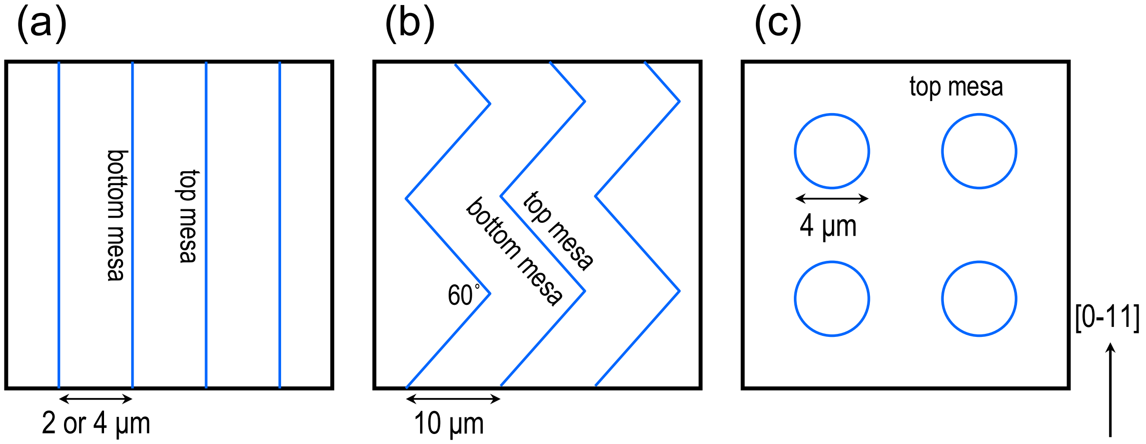

Figure 2 Top view scheme of (a) [0-11] stripe-patterned InP (100) and (311)B substrates with stripe width and separation of 2 or 4 µm, (b) zigzag-patterned InP (311)B substrates with 10 µm width and angle of ±60° off [0-11], and (c) circular hole-patterned InP (311)B substrates with 4 µm diameter. The mesa depth is 50 and 200 nm for patterned InP (100) substrates, and 15 and 200 nm for patterned InP (311)B substrates.

For clarity, we briefly recall the essential steps for SL template formation and QD ordering shown in Fig. 3:

1. Growth of randomly distributed InAs QDs on smooth InGaAsP buffer layer followed by 10 s annealing under As flux.
2. Growth of a thin InGaAsP cap layer.
3. Annealing at higher temperature. Adatom migration leads to deformation of the QDs. On InP (100) the QDs flatten and elongate along the elastically soft [001] or [010] directions [6,7] where [001] is selected by the substrate miscut 2° towards (110) generating steps in the same direction. The miscut is, hence, essential for well defined template formation. On InP (311)B the QDs flatten with symmetrical lateral size increase again along the elastically soft directions ±45° off [-233] [3,4].
4. Growth of an InGaAsP separation layer.
5. Repetition of steps (1)-(4) forming the SL template. The QDs nucleate on top of each other due to strain correlation. The lateral ordering and uniformity improve. On InP (100) a wire-like InAs structure oriented

along [001] evolves. On InP (311)B a spot-like 2-D InAs mesa structure oriented along ±45˚ off [-233] evolves.

6. Growth of InAs QDs on top of the SL template. The QDs order in periodic linear 1-D arrays oriented along [001] on InP (100) and in a periodic 2-D lattice oriented along ±45˚ off [-233] on InP (311)B due to local strain recognition. The QD emission wavelength is tuned into the 1.55-µm region through the insertion of an ultrathin GaAs interlayer beneath the InAs QDs [5].

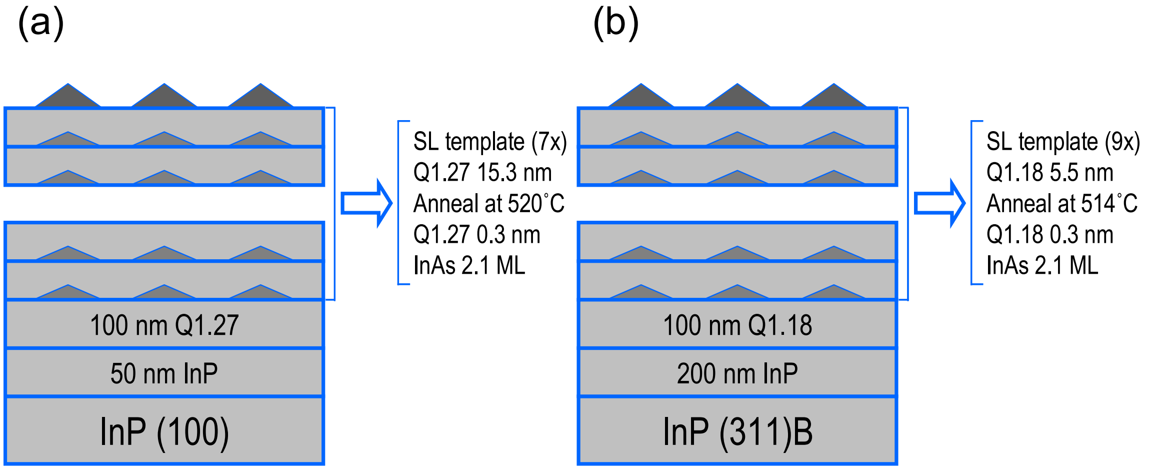

Figure 3 Sample structure of (a) 1-D InAs QD arrays on InP (100) substrate and (b) 2-D InAs QD arrays on InP (311)B substrate.

For patterned InP (100) substrates, the growth commenced with 50 nm thick InP and 100 nm thick lattice-matched InGaAsP with room temperature (RT) bandgap at 1.27 µm (Q1.27), followed by a seven-periods InAs/InGaAsP SL template. Each of the SL periods comprised 2.1 monolayers (ML) InAs, 10 s growth interruption under As flux, thin capping by 0.3-nm Q1.27, annealing for 2 min under As flux, and growth of a 15.3-nm Q1.27 separation layer. On top of the SL template, 3.2 ML InAs was deposited for QD formation. The growth temperature was kept constant at 505 ˚C and the annealing temperature was 520 ˚C. The growth rate of InAs was 0.23 ML/s.

For patterned InP (311)B substrates, the growth commenced with 200 nm thick InP and 100 nm thick lattice-matched InGaAsP with RT bandgap at 1.18 µm (Q1.18). Each of the nine periods of the following InAs/InGaAsP SL template consisted of 2.1 ML InAs, 10 s growth interruption under As flux, thin capping by 0.3-nm Q1.18, annealing for 2 min under As flux, and growth of a 5.5-nm Q1.18 separation layer. On top of the SL template, a 3.2 ML InAs QD layer was grown. The growth temperature was 505 ˚C throughout the entire structure and the annealing temperature was 514 ˚C. The growth rate of InAs was 0.18. ML/s. The details of growth parameter is summarized in Fig. 3 for both (100) and (311)B substrates. These are the optimized growth parameters for buffer layer formation, SL template evolution, and QD ordering on patterned InP (100) and (311)B substrates. All samples were characterized by a tapping mode atomic-force microscopy (AFM) in air.

6.4 Results and Discussion

6.4.1 Planar InP (100) Substrates for Reference

Figure 4 (a) shows the AFM image of the linear 1-D InAs QD arrays on the optimized InAs/InGaAsP SL template on planar InP (100) for reference, as discussed in Chapter 4. The QD arrays are aligned along the elastically soft [001] direction, selected by the substrate miscut. The QD arrays have an average lateral periodicity of 188 nm in the perpendicular [010] direction which is extracted from the 2-D fast Fourier transform analysis shown in Fig. 4 (b).

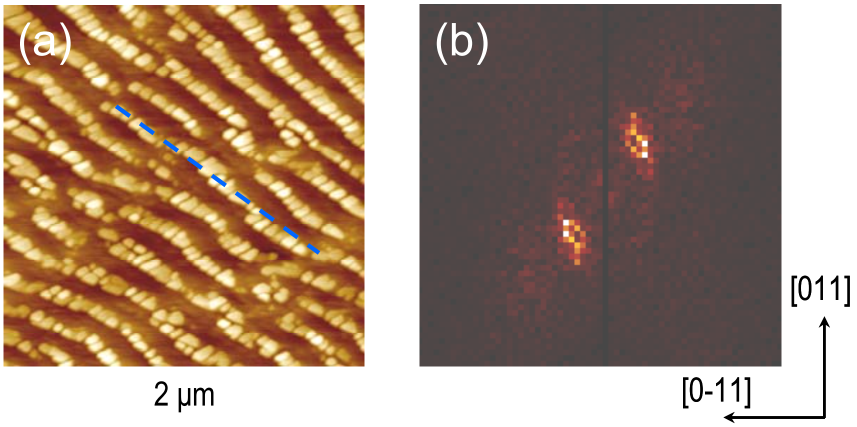

Figure 4 (a) AFM image of uncapped 1-D 3.2 ML InAs QD arrays on the optimized seven-periods InAs/Q1.27 SL template on InP (100) substrate. The scan field is 2.0 × 2.0 μm^2 and the height contrast is 20 nm. The dashed line is a guide for the eye along the direction of ordering. (b) Two-dimensional fast-Fourier transform analysis of (a).

6.4.2 Patterned InP (100) Substrates

Figure 5 shows the InAs QD arrays grown on the optimized InAs/InGaAsP SL template on the shallow-patterned InP (100) substrates with mesa stripes along (a) [010], (b) [001], (c) [011], and (d) [0-11]. During InP/InGaAsP buffer layer growth, vicinal sidewall planes (inclination of a few degrees) develop for all stripes. This is typical for the growth on shallow-patterned substrates where stepped sidewalls with step edges in the sidewall direction, rather than facets develop.

For the vicinal sidewall planes towards (00-1) of the [010]-oriented stripes with relatively large inclination, shown in area 1 in Fig. 5 (a), the linear QD arrays are rotated away from [001]. This is attributed to the medium step density on the sidewall planes with step edges along [010] which modify the direction of adatom migration during annealing in SL template formation. For the sidewall planes towards (001) with smaller inclination the arrays direction is maintained along [001], shown in area 2 in Fig. 5 (a). On the bottom part of the sidewall planes towards (001) with the largest inclination and highest step density with step edges along [010] the arrays are rotated by 90° along [010], which is the other elastically soft direction now selected by the steps on the sidewall planes, shown in area 3 in Fig. 5 (a). On the vicinal sidewall planes of the [001]-oriented stripes, shown in Fig. 5 (b), steps with step edges in this direction do not change the direction of the QD arrays due to the substrate miscut. The behavior on [011] and [0-11]-oriented stripes is very complex due to the superposition of steps along [001] (due to the substrate miscut) and [011]/[0-11] (due to the stripes). A zigzag arrangement alternately along [001] and [010], again the two equivalent elastically soft directions, is observed on the vicinal sidewall planes towards (0-11) of [011]-oriented stripes [Fig. 5 (c)]. This is similar to that on vicinal substrates with miscut 2° towards (111)B, discussed in Chapter 4, having steps with step edges in the same direction as the sidewall planes. There is an indication of 90° arrays rotation on the vicinal sidewall planes towards (011) of [0-11]-stripes [Fig. 5 (d)] which, at present, is not well understood.

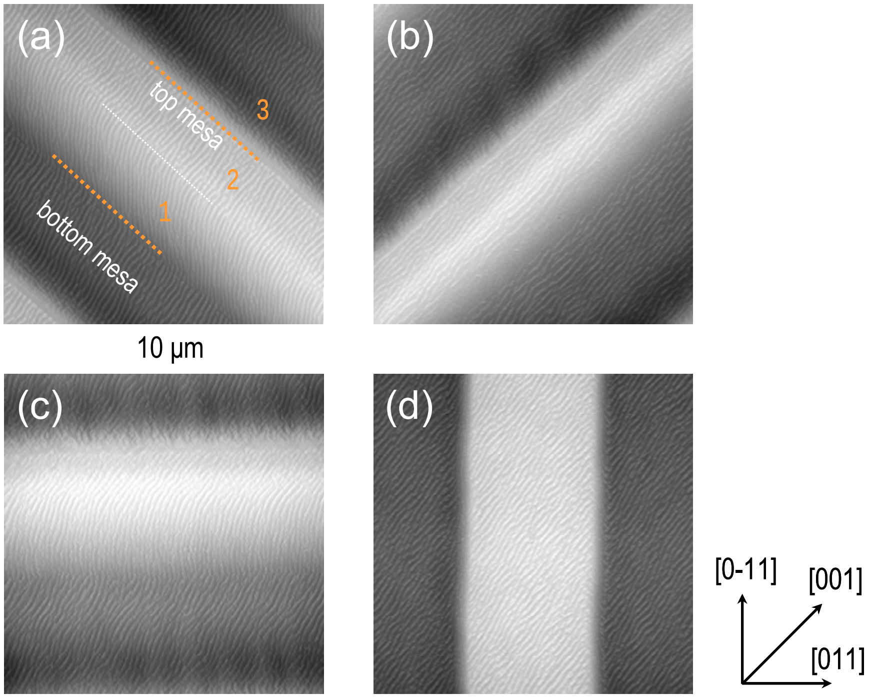

Figure 5 Deflection mode AFM images of uncapped 1-D 3.2 ML InAs QD arrays on the optimized seven-periods InAs/Q1.27 SL template on 50-nm-deep (a) [010], (b) [001], (c) [011], and (d) [0-11] stripe-patterned InP (100) substrate with 4 µm separation and width. The scan field is 10.0 × 10.0 µm^2 for all images. The dashed lines in (a) are a guide for the eye following the mesa stripe. The numbers indicate areas of different QD ordering on the sidewalls.

The InAs QD arrays grown on the optimized InAs/InGaAsP SL template on the deep-patterned InP (100) substrates with mesa stripes along [010], [001], [011], and [0-11] are shown in Fig. 6 (a-d). Again, vicinal sidewall planes are developed during buffer layer growth, which coexist with steep (inclination more than 10 degrees) side facets. The steep side facets are QD free reflecting their slow-growing behavior while the QD arrays formation on the vicinal sidewall planes is essentially the same as that on the sidewall planes of the shallow-patterned mesa stripes.

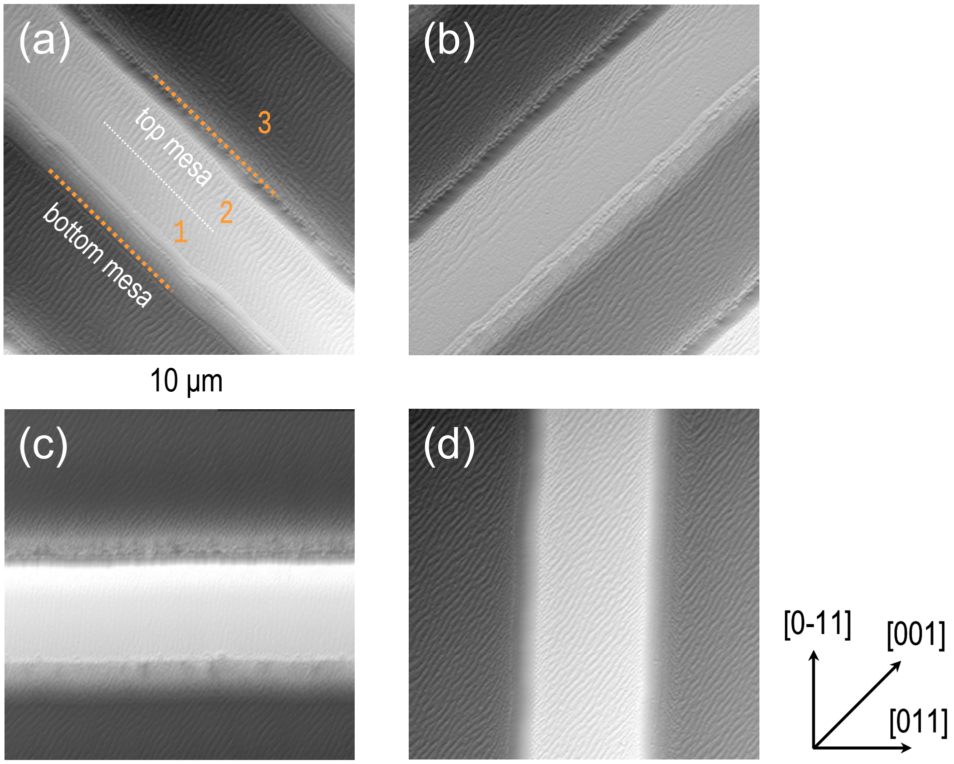

Figure 6 Deflection mode AFM images of uncapped 1-D 3.2 ML InAs QD arrays on the optimized seven-periods InAs/Q1.27 SL template on 200-nm-deep (a) [010], (b) [001], (c) [011], and (c) [0-11] stripe-patterned InP (100) substrate with 4 µm separation and width. The scan field is 10.0 × 10.0 µm^2 for all images. The dashed lines in (a) are a guide for the eye following the mesa stripe. The numbers indicate areas of different QD ordering on the sidewalls.

6.4.3 Planar InP (311)B Substrates for Reference

Figure 7 (a) shows the AFM image of the 2-D arrays of InAs QDs on the optimized InAs/InGaAsP SL template on singular InP (311)B for reference, as discussed in Chapter 5. In between these large QDs, dense small QDs form which are not further considered here. The QDs are aligned in a 2-D network along ±45° off [-233]. The QDs average lateral periodicity along these directions is 202 nm which is extracted from the 2-D fast Fourier transform analysis shown in Fig. 7 (b).

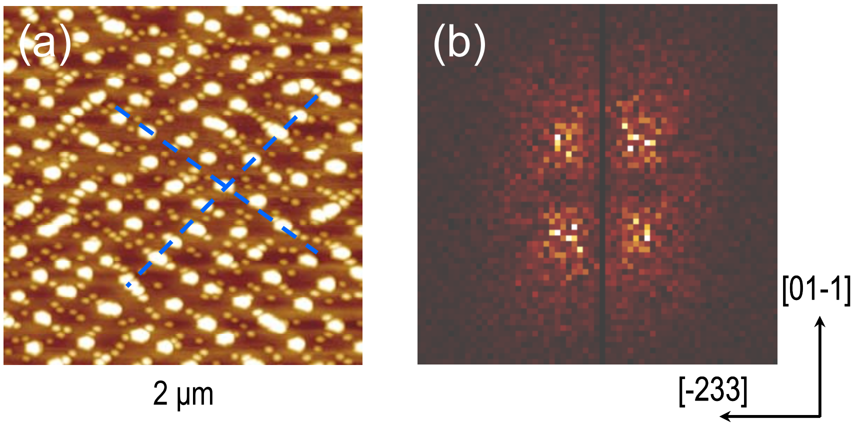

Figure 7 (a) AFM image of uncapped 2-D 3.2 ML InAs QD arrays on the optimized nine-periods InAs/Q1.18 SL template on InP (311)B substrate. The scan field is 2.0 × 2.0 μm^2 and the height contrast is 30 nm. The dashed lines are a guide for the eye along the directions of ordering. (b) Two-dimensional fast-Fourier transform analysis of (a).

6.4.4 Patterned InP (311)B Substrates

Figure 8 shows the InAs QD arrays grown on the optimized InAs/InGaAsP SL template on the shallow-patterned InP (311)B substrates and Fig. 9 shows those on the deep-patterned InP (311)B substrates with (a) [0-11]-stripe pattern, (b) zigzag pattern with mesa top acute angle pointing towards [-233], (c) zigzag pattern with mesa top acute angle pointing towards [2-3-3], and (c) circular hole pattern. For both shallow- and deep patterns only QD free mesa side facets form. For the shallow patterns this is in contrast to shallow-patterned GaAs (311)B substrates where the vicinal sidewall with additional steps developed with small inclination perturbing the periodic 2-D QD arrays into zig-zag arrangement, as previously mentioned in Section 2.6.2, and generally to shallow-patterned InP (311)B substrates, developing vicinal stepped sidewall planes. Therefore, for both shallow- and deep-patterned InP (311)B substrates, the mesa top and bottom areas are flat and the natural ordering of the 2-D QD arrays is not affected.

On the deep-patterned InP (311)B substrates a row of dense QDs forms on top along the side facets due to their slow-growing behavior, similar to deep-patterned GaAs (311)B substrates, with preferential migration of In away from the side facets to the mesa top and bottom [2,6]. Non-equivalent mesa sidewalls formation indicates the growth rate anisotropy between the sidewall plane towards (111) and (100). This effect is too small on the shallow InP (311)B patterns.

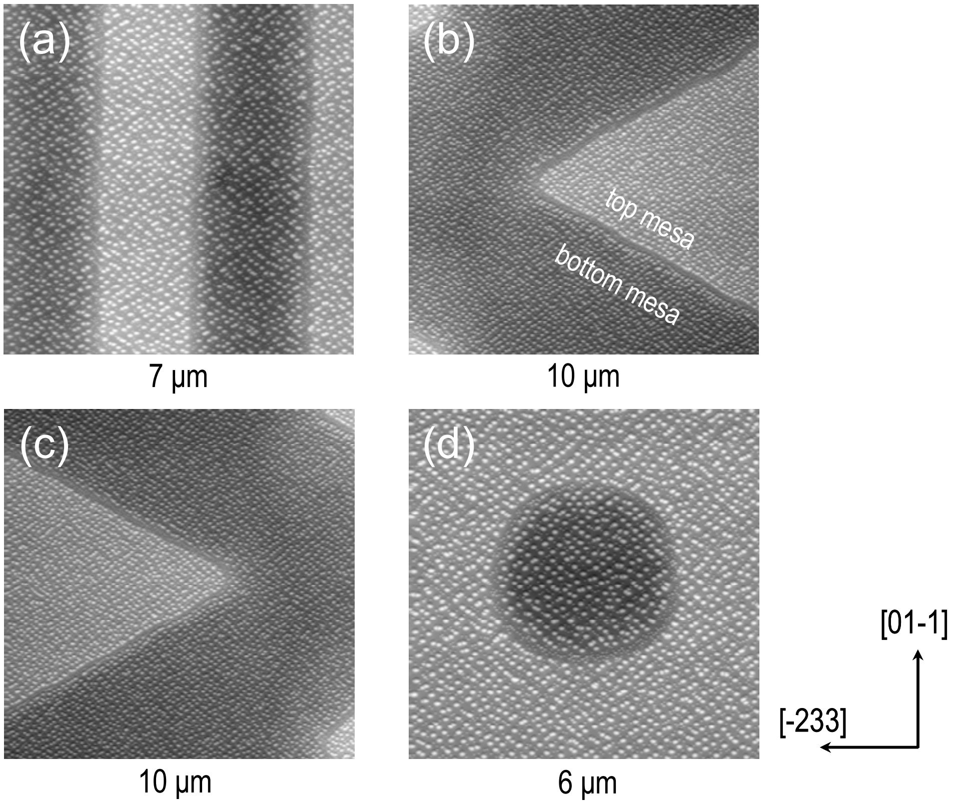

Figure 8 Deflection mode AFM images of uncapped 2-D 3.2 ML InAs QD arrays on the optimized nine-periods InAs/Q1.18 SL template on 15-nm-deep (a) 2-µm-width [0-11] stripe-patterned, (b) and (c) 10-µm-width zigzag-patterned with mesa top acute angle pointing towards [-233] and [2-3-3], and (d) 4-µm-diameter circular hole-patterned InP (311)B substrate. The scan field is 7.0 × 7.0 µm^2 for (a), 10.0 × 10.0 µm^2 for (b) and (c), and 6.0 × 6.0 µm^2 for (d).

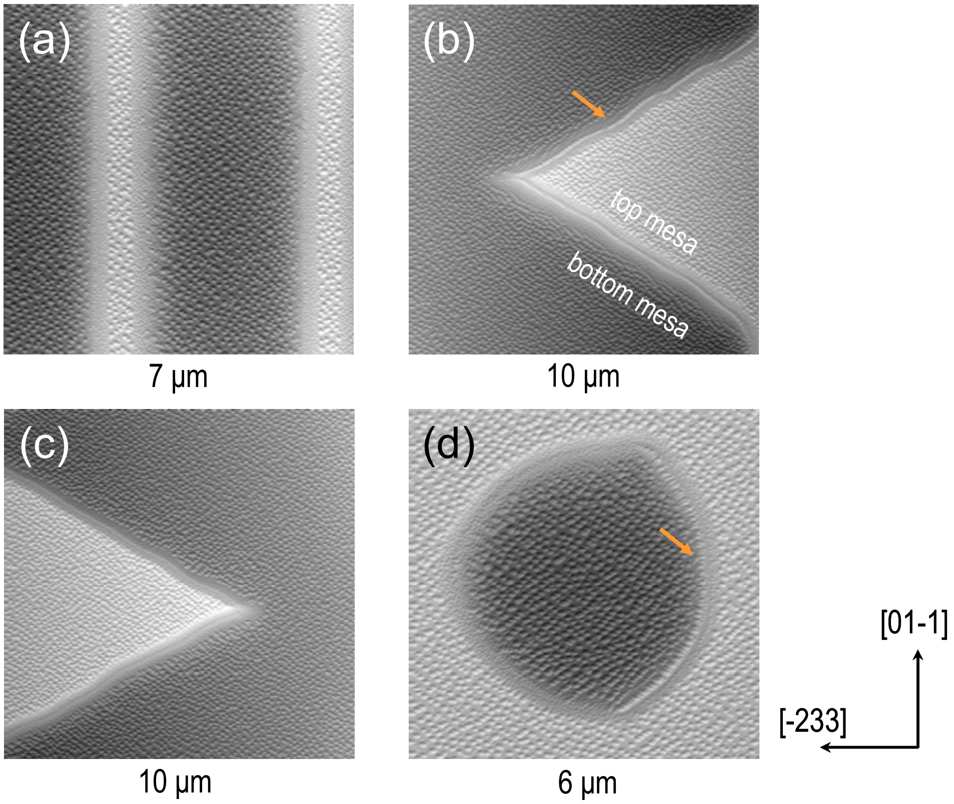

Figure 9 Deflection mode AFM images of uncapped 2-D 3.2 ML InAs QD arrays on the optimized nine-periods InAs/Q1.18 SL template on 200-nm-deep (a) 2-μm-width [0-11] stripe-patterned, (b) and (c) 10-μm-width zigzag-patterned with mesa top acute angle pointing towards [-233] and [2-3-3], and (d) 4-μm-diameter circular hole-patterned InP (311)B substrate. The scan field is 7.0 × 7.0 μm^2 for (a), 10.0 × 10.0 μm^2 for (b) and (c), and 6.0 × 6.0 μm^2 for (d). The arrows in (b,d) indicate the rows of dense QDs on top along the mesa sidewalls.

6.5 Summary

We have studied the formation of ordered InAs QD arrays by self-organized anisotropic strain engineering of InAs/InGaAsP SL templates in CBE on patterned InP (100) and (311)B substrates. On shallow- and deep stripe-patterned InP (100) substrates, depending on the stripe orientation, the linear 1-D InAs QD arrays are rotated away from their natural [001] direction, selected by the substrate miscut, due to the presence of vicinal stepped sidewall planes modifying the self-organization process, which coexist with QD free steep side facets on the deep-patterned substrates. On shallow- and deep-patterned InP (311)B substrates only QD free side facets are observed with flat top and bottom areas not affecting the formation of the natural 2-D InAs QD arrays. On the deep-patterned substrates a row of dense QDs forms on top along the side facets due their slow-growing behavior. Hence, in particular on InP (100) substrates, pattern generated steps modify the self-organized SL template formation to produce complex

InAs QD arrays and networks needed for next generation quantum functional devices.

Bibliography

[1] T. Mano, R. Nötzel, D. Zhou, G. J. Hamhuis, T. J. Eijkemans, and J. H. Wolter, *J. Appl. Phys.* **97**, 014304 (2005).

[2] E. Selçuk, G. J. Hamhuis, and R. Nötzel, *J. Appl. Phys.* **102**, 094301 (2007).

[3] H. Z. Xu, K. Akahane, H. Z. Song, Y. Okada, and M. Kawabe, *Appl. Surface. Sci.* **185**, 92 (2001).

[4] P. M. Lytvyn, V. V. Strelchuk, O. F. Kolomys, I. V. Prokopenko, M. Ya. Valakh, Yu. I. Mazur, Zh. M. Wang, G. J. Salamo, and M. Hanke, *Appl. Phys. Lett.* **91**, 173118 (2007).

[5] Q. Gong, R. Nötzel, P. J. van Veldhoven, T. J. Eijkemans, and J. H. Wolter, *Appl. Phys. Lett.* **84**, 275 (2004).

[6] R. Nötzel, M. Ramsteiner, J. Menniger, A. Trampert, H.-P. Schönherr, L. Däweritz, and K. H. Ploog, *J. Appl. Phys.* **80**, 4108 (1996).

CHAPTER 7

Wavelength Controlled Multilayer-Stacked Linear InAs Quantum Dot Arrays: A Self-Ordered Quantum Dot Crystal

ABSTRACT

Multilayer-stacked linear InAs quantum dot (QD) arrays are created on InAs/InGaAsP superlattice (SL) templates formed by self-organized anisotropic strain engineering on InP (100) substrates in chemical beam epitaxy (CBE). Stacking of the QD arrays with identical emission wavelength in the 1.55 µm region at room temperature is achieved through the insertion of ultra-thin GaAs interlayers beneath the QDs with increasing interlayer thickness in successive layers. The increment of the GaAs interlayer thickness compensates the QD size/wavelength increase during strain correlated stacking. This is the demonstration of a three-dimensionally self-ordered QD crystal with fully controlled structural and optical properties.[1]

---

[1] These results have been published as: *Wavelength controlled multilayer-stacked linear InAs quantum dot arrays on InGaAsP/InP (100) by self-organized anisotropic strain engineering: A self-ordered quantum dot crystal*, N. Sritirawisarn, F. W. M. van Otten, T. J. Eijkemans, and R. Nötzel, Appl. Phys. Lett. **93**, 131906 (2008).

7.1 Introduction

According to the results in Chapter 4, based on anisotropic adatom surface migration and lateral and vertical strain correlations, wire-like InAs nanostructures are created during growth of an InAs/InGaAsP superlattice (SL) which acts as template for the formation of linear InAs QD arrays due to local strain field recognition. This self-organization process has been proven to produce ordered QD arrays with excellent optical properties up to room temperature (RT) whose emission wavelength was tuned into the technologically important 1.55 µm telecom wavelength region through the insertion of ultra-thin GaAs interlayers beneath the QDs.

In this Chapter, we present the formation of multilayer-stacked linear InAs QD arrays on the InAs/InGaAsP SL template on InP (100) demonstrating a fully self-ordered three-dimensional QD crystal. Identical emission wavelength of the stacked QD arrays is achieved by increasing the thickness of the GaAs interlayer in successive layers. The increment of the GaAs interlayer thickness compensates the QD size/wavelength increase encountered in strain correlated stacking for relatively thin separation layers [1-3], discussed earlier in Chapter 2 (Section 2.2). The stacked QD arrays exhibit strong photoluminescence (PL) emission in the 1.55 µm wavelength region up to RT.

The structure details and characterization techniques are given in section 7.2. The results of the AFM and PL measurements of the samples are shown in Section 7.3. The conclusion is summarized in section 7.4.

7.2 Experimental Details

The samples were grown by CBE on semi-insulating InP (100) substrates with 2° miscut toward (110). Pressure controlled trimethylindium (TMI), triethylgallium (TEG), AsH_3, and PH_3 were used as precursor. The AsH_3 and PH_3 gases were thermally decomposed in a high temperature injector at 900 °C. After growth of a 200 nm InP buffer layer and 100 nm lattice-matched InGaAsP with band gap of 1.25 µm (Q1.25), the SL template was grown consisting of 2.1 ML InAs, 10 s growth interruption under As flux, 0.3 nm Q1.26 cap layer, 2 min annealing, 15.3 nm Q1.25 separation layer, and repeated for 7 periods. On top of the SL template a 2.6 ML InAs QD layer was grown with 0.6 ML GaAs interlayer inserted beneath. The multilayer-stacked 2.6 ML InAs QD arrays were separated by 16 nm Q1.25. The increment of the GaAs interlayer thickness in successive 2.6 ML InAs QD layers was 0.12 ML or 0 ML for comparison. For PL measurements the last QD layer was capped by 100 nm Q1.25 and 50 nm InP. The growth temperature was 505 °C for all layers and the annealing temperature was 520 °C. The growth rate of InAs was 0.24 ML/s. The surface morphology of the uncapped samples was characterized by tapping mode atomic force microscopy (AFM) in air. For the PL studies, the samples were capped by 100 nm Q1.25 and 50 nm InP and excited by a Nd:YAG laser (532 nm) with excitation power density of 256 mW/cm². The PL was dispersed by a single monochromator and recorded by a cooled InSb detector.

7.3 Results and Discussion

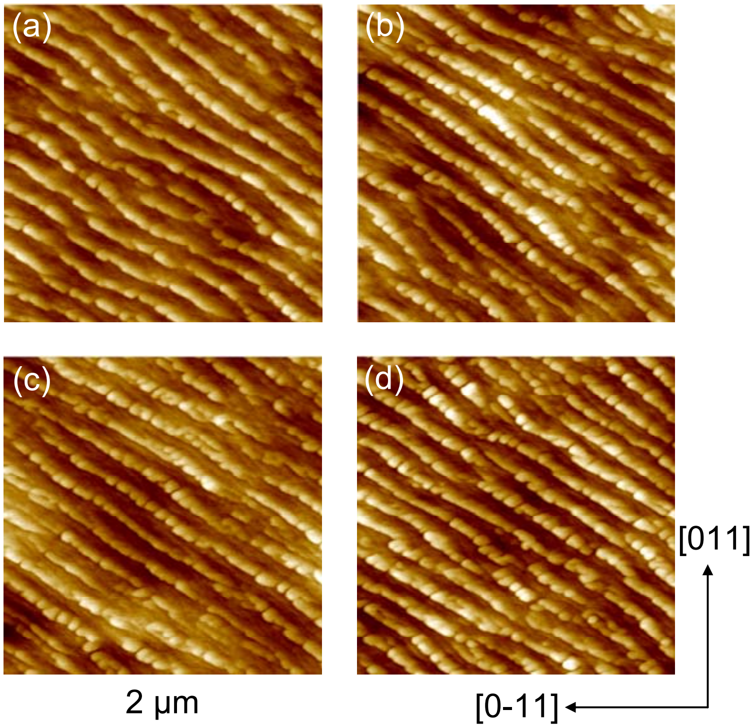

Figure 1 (a) AFM image of uncapped single-layer 2.6 ML InAs QD arrays on the seven periods 2.1 ML InAs/0.3 + 15.3 nm InGaAsP SL template on InP (100) substrate with 0.6 ML GaAs interlayer beneath the QDs. (b) and (c) AFM images of uncapped two-fold-stacked and three-fold-stacked 2.6 ML InAs QD arrays with 0.12 ML increment of the GaAs interlayer thickness in successive layers. (d) AFM image of uncapped three-fold-stacked 2.6 ML InAs QD arrays without increment of the GaAs interlayer thickness. The scan field is 2.0×2.0 µm^2 and the height contrast is 10 nm.

Figure 1(a) to (c) show the AFM images of the uncapped single-layer QD arrays, described in detail in Ref. 9, the uncapped two-fold-stacked, and the uncapped three-fold-stacked QD arrays with increment of the GaAs interlayer thickness. For comparison, the AFM image of the uncapped three-fold-stacked QD arrays without increment of the GaAs interlayer thickness is shown in Fig. 1(d). The QD arrays are aligned along the elastically soft [001] direction to minimize the strain energy [4,5], which is selected by the miscut of the substrate with steps in the same direction, as discussed in Chapter 4. InAs amount and growth rate, cap layer thickness, annealing temperature, and number of SL template periods are optimized for self-organized ordering due to anisotropic adatom surface migration during annealing and lateral and vertical strain correlations during stacking. Strain correlated stacking of the QD arrays separated by 16 nm Q1.25 manifests itself by the maintenance of linear ordering. With increment of the GaAs interlayer thickness, the height of the top two-fold-stacked QD arrays (3.5±0.5 nm height, with 0.72 ML GaAs interlayer) and that of the three-fold-stacked QD arrays (3.2±0.5 nm height, with 0.84 ML GaAs interlayer) is comparable to that of the single-layer QD arrays (3.3±0.5 nm height, with 0.6 ML GaAs interlayer). The QD diameters remain almost unchanged with increase of the number of stacked layers (single-layer 87.6±8.0 nm, two-fold-stacked 87.6±10.1 nm, three-fold-stacked 87.1±9.7 nm), as plotted in Fig. 2.

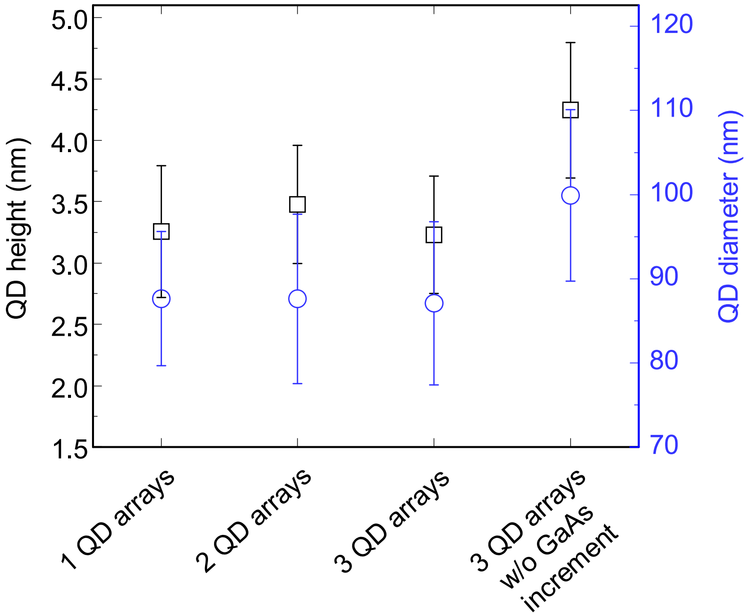

Figure 2 Average height (black squares) and diameter (blue circles) of the QDs within the arrays as a function of the number of stacked layers.

The role of the GaAs interlayer is to suppress As/P exchange encountered during the deposition of InAs on InGaAsP. This reduces the QD height as a function of interlayer thickness and therefore the emission wavelength from far above 1.6 µm at RT into the 1.55 µm telecom wavelength region [6], discussed in Chapter 3. For the stacked QD arrays the increase of the GaAs interlayer thickness in successive layers compensates the well-known QD height and diameter increase [1-3], to maintain the QD height and diameter throughout the entire structure. This is underlined by the pronounced increase of the QD height (4.2±0.6 nm) and diameter (99.9±10.2 nm) for the top three-fold-stacked QD arrays without increment of the GaAs interlayer thickness, see Figs. 1 (d) and 2.

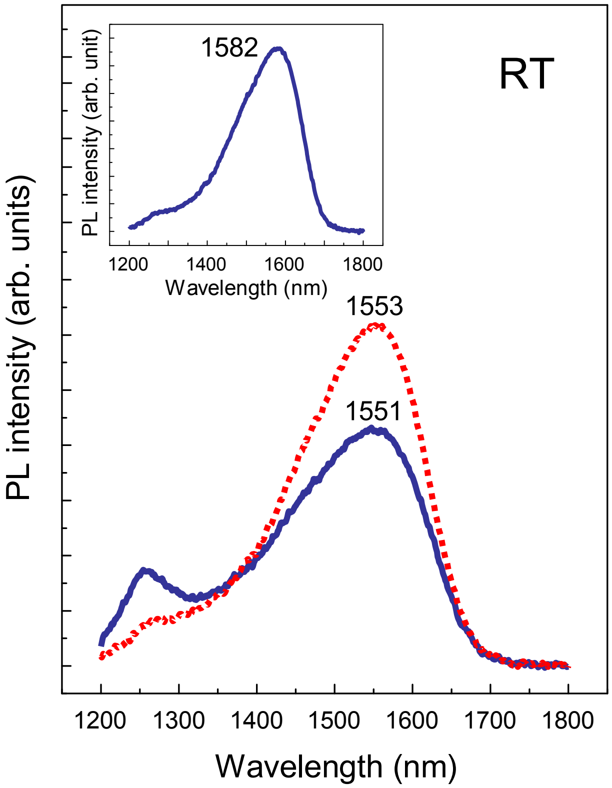

Figure 3 PL spectra taken at RT of capped single-layer (solid line) and three-fold-stacked (dashed line) 2.6 ML InAs QD arrays with 0.12 ML increment of the GaAs interlayer thickness in successive layers. Inset: PL spectrum of capped three-fold-stacked 2.6 ML InAs QD arrays without increment of the GaAs interlayer thickness.

The PL measurements taken at RT of the capped multilayer-stacked QD arrays shown in Fig. 3 corroborate the structural properties. The PL peak wavelength of the three-fold-stacked QD arrays (1553 nm) is almost identical compared to that of the single-layer QD arrays (1551 nm). The PL efficiency of the three-fold-stacked QD arrays increases by 44% compared to that of single-layer QD arrays indicating good crystal quality of the multilayer-stacked structure. Without increment of the GaAs interlayer thickness, the PL peak wavelength redshifts to 1582 nm due to the gradual increase of the QD size upon stacking, see inset in Fig. 3.

7.4 Summary

In summary, the formation of multilayer-stacked linear InAs quantum dot (QD) arrays on InAs/InGaAsP superlattice (SL) templates formed by self-organized anisotropic strain engineering on InP (100) substrates in chemical beam epitaxy (CBE) has been achieved. Identical emission wavelength of the stacked QD arrays in the 1.55 μm telecom region at room temperature has been accomplished through the insertion of ultra-thin GaAs interlayers beneath the QDs with increasing thickness in successive layers, demonstrating a three-dimensionally self-ordered QD crystal.

Bibliography

[1] Q. Xie, A. Madhukar, P. Chen, and N. P. Kobayashi, *Phys. Rev. Lett.* **75**, 2542 (1995).

[2] X.-D. Wang, N. Liu, C. K. Shih, S. Govindajaru, and Jr. A. L. Holmes, *Appl. Phys. Lett.* **85**, 1356 (2004).

[3] O. Flebbe, H. Eisele, T. Kalka, F. Heinrichsdorff, A. Krost, D. Bimberg, and M. Dähne-Prietsch, *J. Vac. Sci. Technol. B.* **17** (4), 1639 (1999).

[4] V. A. Shchukin, N. N. Ledentsov, P. S. Kop'ev, and D. Bimberg, *Phys. Rev. Lett.* **75**, 2968 (1995).

[5] V. A. Shchukin and D. Bimberg, *Rev. Mod. Phys.* **71**, 1125 (1999).

[6] Q. Gong, R. Nötzel, P. J. van Veldhoven, T. J. Eijkemans, and J. H. Wolter, *Appl. Phys. Lett.* **84**, 275 (2004).

CONCLUSIONS AND RECOMMENDATIONS FOR FUTURE WORK

Ordered InAs/InP quantum dot arrays at telecom wavelength

This dissertation demonstrates the growth and optical characterization of ordered InAs/InP quantum dot (QD) arrays grown by chemical-beam epitaxy (CBE). The creation of InAs/InP QD arrays is governed by self-organized anisotropic strain engineering of InAs/InGaAsP superlattice (SL) templates leading to the formation of linear ordered one-dimensional (1-D) InAs QD arrays on InP (100) substrates and a periodic square lattice of two-dimensional (2-D) InAs QD arrays on InP (311)B substrates. The photoluminescence (PL) emission of the InAs QD arrays reveals excellent optical quality up to room temperature (RT). The emission wavelength is tuned into the technological important 1.55-μm region for telecom applications through the insertion of ultrathin GaAs interlayers beneath the QDs. Electronic coupling in linear InAs QD arrays on InP (100) is revealed by temperature-dependent PL and polarization-dependent PL measurements. Identical emission wavelength of multilayer-stacked linear QD arrays is achieved by increasing the GaAs interlayer thickness in successive layers.

Self-assembled semiconductor QDs have led to numerous device applications ranging from nanophotonics, nanoelectronics to quantum information processing due to their three-dimensional carrier confinement. Owing to the modern crystal growth fabrication technologies, e.g. molecular-beam epitaxy (MBE), metal-organic vapor phase epitaxy (MOVPE), and CBE, QDs and related quantum structures can be prepared precisely at the atomic scale leading to the ultimate control of the QD shape, size, composition, and emission wavelength. In addition, control of the QD nucleation sites and QD ordering is the prerequisite for exploitation of new functionalities for novel quantum devices. The most common technique to position the QDs is by using artificially patterned substrates where the pattern geometry is defined by electron-beam lithography. The main disadvantages are, however, the degradation of the structural and optical properties due to lithographic imperfections and etching defects. To tackle this obstacle, a novel technique for the lateral alignment of QDs was realized based on self-organized anisotropic strain engineering creating ordered strain-modulated SL template structures. In this study the concept is further developed and transferred from the previously investigated GaAs-based system by MBE to the InP-based system by CBE where the QD emission wavelength is more suitable for telecom device applications.

For the InAs/InP system, usually the formation of various nanostructures such as elongated QDs, called “quantum dashes” (QDashes) or even quantum wires (QWRs) is observed at practically identical growth conditions. Most probably this is due to the low lattice mismatch between InAs and InP of 3 % as compared to InAs and GaAs of 7 % and the strong As/P exchange reaction. In this study, we identify the surface morphology of the buffer layer as key parameter for the formation of InAs QDs or QDashes on lattice-matched InGaAsP on InP (100) substrates. Growth conditions leading to the formation of QDashes are always accompanied by a rough buffer layer morphology. Although other growth parameters such as higher growth temperature, larger As flux, and compressive buffer layer strain favor the formation of QDs, once, the buffer layer has a rough morphology, QDashes are formed during InAs growth. On the contrary, well-shaped and symmetric QDs are reproducibly formed on smooth buffer layers. Hence, we conclude that not the growth conditions during InAs depositions, but rather the related surface morphology of the buffer layer determines the formation of either QDs or QDashes, which both exhibit high optical quality.

On smooth buffer layers, laterally ordered linear 1-D InAs QD arrays and a periodic square lattice of 2-D InAs QD arrays are formed by self-organized anisotropic strain engineering of InAs/InGaAsP SL templates on InP (100) and (311)B substrates, respectively. The SL template formation comprises InAs QD growth, thin InGaAsP capping, annealing at higher temperature, InGaAsP overgrowth, and stacking. This produces wirelike InAs nanostructures along [001] on InP (100) and spot-like InAs nanostructures oriented along ±45° off [-233] on InP (311)B substrates due to anisotropic adatom surface migration during annealing and lateral/vertical strain correlation during stacking. The orientation of the linear InAs QD arrays is determined by the elastically soft directions of the InP crystal and the substrate miscut. InAs QD ordering is governed by local recognition of the lateral strain field modulations on the SL template surfaces. The growth parameters for obtaining straight, well-ordered, and uniform QD arrays are optimized, such as InGaAsP cap layer thickness, annealing temperature, InAs amount and growth rate, and number of SL periods. The InAs QD arrays reveal strong PL emission up to RT. This is the advantage of self-organized QD ordering compared to methods based on artificial substrate patterning which often degrade the optical quality. The emission of InAs QD arrays is tuned into the important 1.55-μm telecommunication wavelength region by the insertion of ultrathin, 0.8 – 2.0 monolayers (ML), GaAs interlayers beneath the QDs which suppress As/P exchange during InAs QD formation. For the linear InAs QD arrays on InP (100) substrates, lateral electronic coupling of the QDs along the chains is observed as indicated by temperature dependent PL measurements and the linear PL polarization.

The concept of self-organized anisotropic strain engineering for QD ordering has been extended for formation of more complex architectures of lateral QD arrays by combining it with step engineering on artificially patterned InP (100) and (311)B substrates. On shallow- and deep stripe-patterned InP (100) substrates, depending on the stripe orientation, the linear 1-D InAs QD arrays are rotated away from their natural direction due to the presence of vicinal stepped sidewall planes modifying the self-organization process, coexisting with QD free steep side facets on deep-patterned substrates. On shallow- and deep-patterned InP (311)B substrates only QD free side facets form with flat top and bottom areas, not affecting the natural ordering of the 2-D InAs QD arrays. On the deep-patterned substrates a row of dense QDs forms on top along the side facets due to their slow-growing behavior.

In the last chapter, multilayer-stacked linear InAs QD arrays on InAs/InGaAsP SL templates on InP (100) substrates are realized. Identical emission wavelength of the stacked QD arrays in the 1.55-µm region at RT is achieved by increasing the thickness of the GaAs interlayer beneath the QDs in successive layers. The sub-ML increment of the GaAs interlayer thickness compensates the QD size/wavelength increase during vertical strain correlated stacking. This is the demonstration of a three-dimensionally self-ordered QD crystal with fully controlled structural and optical properties.

Finally, further investigations of the physical and optical properties of the 1-D and 2-D InAs/InP QD arrays are envisioned for future research. Cross-sectional scanning tunneling microscopy (X-STM) or cross-sectional transmission electron microscopy (X-TEM) is useful to obtain more information about material intermixing, geometry of the capped QD layers in the SL template structure to provide deeper insight into the growth mechanism and give input for possible theoretical models. Advanced optical measurement techniques, e.g., (time-resolved) single QD PL spectroscopy or magneto PL spectroscopy could further indicate the electronic coupling in the 1-D QD arrays. Moreover, selective-area epitaxy could lead to the formation of localized QD arrays on microscopic mesa patterns with complex arrangements. The growth rate enhancement in selective-area epitaxy by CBE on dielectric masked substrates, e.g., Silicon Nitride (Si_3N_4) or Silicon Dioxide (SiO_2), is negligible compared to that in MOCVD due to desorption of group-III molecules (TMI, TEG) on masked areas. This allows the growth parameters to be controlled similar to those for unmasked planar substrates. The localized QD arrays could be useful for future applications such as quantum information processing and quantum computing.

LIST OF PUBLICATIONS

1. N. Sritirawisarn, J. L. E. Wera, F. W. M. van Otten, and R. Nötzel, *Evolution of ordered one-dimensional and two-dimensional InAs/InP quantum dot arrays on patterned InP (100) and (311)B substrates by self-organized anisotropic strain engineering.*, accepted for publication in Journal of Crystal Growth (2010).

2. N. Sritirawisarn, F. W. M. van Otten, P. E. D. Soto Rodriguez, J. L. E. Wera, and R. Nötzel, *Formation of two-dimensional InAs quantum dot arrays by self-organized anisotropic strain engineering on InP (311)B substrates.*, Journal of Crystal Growth **312**, 164 (2010).

3. N. Sritirawisarn and R. Nötzel, *InAs/InP Quantum Dots, Dashes, and Ordered Arrays.*, Japanese Journal of Applied Physics **48**, 04C121 (2009).

4. N. Sritirawisarn, F. W. M. van Otten, T. J. Eijkemans, and R. Nötzel, *Formation of linear InAs/InGaAsP/InP (100) quantum dot arrays by self-organized anisotropic strain engineering in chemical beam epitaxy.*, Journal of Crystal Growth **311**, 1822 (2009).

5. N. Sritirawisarn, F. W. M. van Otten, T. J. Eijkemans, and R. Nötzel, *Formation of stacked linear InAs quantum dot arrays on InGaAsP/InP(100) by self-organized anisotropic strain engineering.*, Physica Status Solidi B **246 (4)**, 858 (2009).

6. N. Sritirawisarn, F. W. M. van Otten, T. J. Eijkemans, and R. Nötzel, *Wavelength controlled multilayer-stacked linear InAs quantum dot arrays on InGaAsP/InP (100) by self-organized anisotropic strain engineering: A self-ordered quantum dot crystal.*, Applied Physics Letters **93**, 131906 (2008).

7. R. Nötzel, N. Sritirawisarn, E. Selcuk, and S. Anantathanasarn, *Lateral Ordering, Position, and Number Control of Self-Organized Quantum Dots: The Key to Future Functional Nanophotonic Devices.*, IEEE Journal of Selected Topics in Quantum Electronics, **14 (4)**, 1140 (2008).

8. N. Sritirawisarn, F. W. M. van Otten, T. J. Eijkemans, and R. Nötzel, *Formation of linear InAs quantum dot arrays on InGaAsP/ InP (100) by self-organized anisotropic strain engineering and their optical properties.*, Journal of Applied Physics **102**, 053514 (2007).

9. N. Sritirawisarn, F. W. M. van Otten, T. J. Eijkemans, and R. Nötzel, *Surface morphology induced InAs quantum dot or dash formation on InGaAsP/InP (100).*, Journal of Crystal Growth **305**, 63 (2007).

International Conference Proceedings

1. N. Sritirawisarn, F. W. M. van Otten, and R. Nötzel, *Ordered 1-D and 2-D InAs/InP quantum dot arrays at telecom wavelength.*, 6th International Conference on Semiconductor Quantum Dots, Nottingham (United Kingdom), April 26-30, 2010.

2. R. Nötzel, N. Sritirawisarn, E. Selcuk, H. Wang, and J. Yuan, *Lateral ordering, position, and number control: tackling today's challenges in quantum dot materials research.*, 2009 Collaborative Conference on Interacting Nanostructures, San Diego (USA), November 9-13, 2009. (Invited)

3. R. Nötzel, N. Sritirawisarn, E. Selçuk, H. Wang, and J. Yuan, *Quantum dots for future nanophotonic devices: lateral ordering, position, and number control.*, 2009 IEEE Photonics Society Annual meeting, Antalya (Turkey), October 4-8, 2009. (Invited)

4. R. Nötzel, N. Sritirawisarn, E. Selcuk, H. Wang, and J. Yuan, *Tackling today's challenges in quantum dot materials research: lateral ordering, position, and number control.*, SemiconNano 2009, Anan (Japan), August 9-14, 2009. (Invited)

5. N. Sritirawisarn and R. Nötzel, *InAs/InP Quantum Dots, Dashes, and Ordered Arrays.*, 2008 International Conference on Solid State Devices and Materials, Ibaraki (Japan), September 23-26, 2008. (Invited)

6. N. Sritirawisarn, F. W. M. van Otten, T. J. Eijkemans, and R. Nötzel, *Formation of linear InAs/InGaAsP/InP (100) quantum dot arrays by self-organized anisotropic strain engineering in chemical beam epitaxy.*, 15th International Conference on Molecular Beam Epitaxy, Vancouver (Canada), August 3-8, 2008.

7. N. Sritirawisarn, F. W. M. van Otten, T. J. Eijkemans, and R. Nötzel, *Formation of stacked linear InAs quantum dot arrays on InGaAsP/InP(100) by self-organized anisotropic strain engineering.*, 5th International Conference on Semiconductor Quantum Dots, Gyeongju (Korea), May 11-16, 2008.

8. N. Sritirawisarn, F. W. M. van Otten, T. J. Eijkemans, and R. Nötzel, *Role of surface morphology for InAs quantum dot or dash formation on*

InGaAsP/InP (100), 19th International Conference on Indium Phosphide and Related Materials, Matsue (Japan), May 14-18, 2007.

9. N. Sritirawisarn, F.W.M. van Otten, and R. Notzel, *InAs quantum dash or dot formation on InGaAsP/InP (100): The buffer layer morphology is crucial*, 14th European Molecular Beam Epitaxy Workshop, Sierra Nevada (Spain), March 5-7, 2007.

ACKNOWLEDGEMENTS

It is such a great pleasure for me to write this acknowledgement part. No doubt, this thesis could not be done without lot of helps from many people in the past 4 years.

Firstly, I would like to express my deep gratitude to my daily supervisor Dr. Richard Nötzel. I always appreciate the discussions we have had throughout 4 years of working in the normal office room to the staircase or pathway to the cafeteria. Thank you for being free all the time. His expertise of not only in the epitaxial growth but also in-depth optical characterization definitely contributed a lot to the work in this thesis. *Thank you very much Richard.*

My sincere thankfulness also goes to prof.dr. Paul Koenraad, my promoter. Throughout his guidance on the assessment talks and other occasions, the PhD studies during 4 years went smoothly as planned. I enjoy lots of time he was sharing his exciting experiences during lunch or coffee break. Thank you also for reading the thesis and giving the critical remarks.

I would like to thank the committee members: prof.dr. William Ted Masselink (my co-promoter), prof.dr. Mark Hopkinson, prof.dr. Christoph Lienau, and Dr. Erwin Kessels for spending your time on reading and giving the remarks on my thesis. I greatly appreciate the very critical and useful comments which improve the quality of my thesis pretty well.

I thank also other academic staff members in the group: prof.dr. Andrea Fiore, Dr. Rob van de Heijden, Dr. Jos Haverkort, Dr. Erik Bakkers, and of course Dr. Andrei Silov. I would like to thank Andrei in special for being a good mentor, friend, even snooker partner. It was very enjoyable time to play with you. Within almost a year of playing, I think we come to the conclusion that the upper table is far more difficult than the bottom one no matter what how good you are. Besides of that, I like your jokes a lot.

I would like to thank Margriet van Doorne and Annebee Langenhuizen for the administrative stuffs. My special sincere goes for Margriet for being more than a secretary. I appreciate your helps for not only the paper works but also the personal problems. I love your Sinterklass party, group activity, and your presence at the football field as our cheerleader.

It was very nice to work with a lot of talented and skillful technicians here in the group. First credit, of course, goes to Frank van Otten for CBE assistances. I think we worked together very well to run the machine and indeed I appreciate your actively responses whenever the CBE is down. I still remember very well when we dissembled the load-lock part and couldn't find the way to put them back again. I like playing indoor soccer with you also but I tell you what… your long shot will never work. Good luck to your works and your family. I thank Rene van Veldhoven and Rian Hamhuis for many valuable discussions about the growth. I thank Tom Eijkemans for PL, AFM, and XRD assistances from very beginning and Frans van Setten for the computer stuff. I also would like to thank Peter Nouwens for help me on the sample maskings, Jos van Ruijven, and Martine van Vlokhoven for a lot of contributions to the technical works. My sincere also goes for the technicians from OED group: Tijbbe, Barry and Erik Jan, for guiding and teaching me a lot of processing machines in the cleanroom.

I greatly enjoyed the 2 months I spent during the internship project at National Institute for Materials Science (NIMS) in Tsukuba, Japan. For this I would like to thank Mano-san, Noda-san, Jo-san, Sakoda-san, and a lot of people over there for very warm welcome and farewell party. It was truly very nice experiences. I hope to see you guys later again.

It was very nice for me to meet Dr. Sanguan Anantathanasarn (P'Nguan), the Thai postdoc in the group by that time. He was so kind to me from the very first day I arrived to the group. I appreciate the every Wednesday night snooker session we had for almost 2 years. I like our scientific discussions and thank you for your guidance to direct my PhD study. I must say that I learn a lot from him. Thank you for being my good brother and I hope to see you again very soon.

I thank my (past) office roommates: Twan, Chris, Paul, Ekber, Adam, and Jia for very nice discussions scientifically and personally. Special words go for Adam and Jia to have a lot of successes throughout the rest of your PhD study.

My special thanks also go for Paul Soto Rodriguez, the internship student, and Jan Wera, the master student. Your contributions to the experimental works helped me a lot to obtain several beautiful results. Thank you very much and good luck to your career.

From the past 4 years, I have met a lot of colleagues from many places. As the group is very big today, it is quite hard to acknowledge every single person I know. However, I would like to mention some of my good friends in special: Niek for the PL measurements and a lot of funs we had together, Junji for being a very good friend, it's good to know that you like Thai food a lot, José, Cem, Dilna, Guido, Dayong, Harm, Nicolas, David, Erik, Robbie, Tom, Alex, Hao, Jens, Murat, Ineke, Samuel, Joris, Juanita, Joost, Salman, Hina, Elmuez, and the rest of the (past) group members though the name is not mentioned here.

I would like to thank Twan, José, Niek, Joost, and Samuel once again for organizing our beloved wine tasting event. I hope you guys continue collecting bottles in my office. Special thanks go to the H.G.F. semisoccer and PeeSen team for providing a lot of funs and relaxing moments throughout 4 years. I thank Toine, William, Gary (Li), Daniel, Erwin, Thijs, and K (P'Nguan) for a great summer football session. It was very nice to meet all of you. I wish you guys a lot of successes.

Of course in the past 4 years away from home, I would like to thank Thai fellows in Eindhoven and in The Netherlands for the good times we spent together. This makes me feel like here is my second home. For this I thank P'Nguan, P'Pam, P'Tu, P'Nat, P'Ham, P'Pipe, P'Tip (and Mikeal), N'Ton, N'Yeast, and N'Kit. I thank N'Maprang, my cousin, in special. I wish you all the very best for your study here.

I would like to thank one special person, Kudaporn, for being my inspiration. I appreciate your encouragements and supports throughout my difficult time here. *Thank you.*

At last, I would like to express my great gratitude to my family, especially my parents, for their endless supports and understandings. I thank my sister for keep bringing the stuffs from home to me. I thank my brother for a lot of supports from him. Almost six years away from home, it makes me know how much I *love* them. *Thank you very much.*

CURRICULUM VITAE

Nut Sritirawisarn, born 21th July 1982 in Bangkok, Thailand

2006-2010:

Ph.D. project, Photonics and Semiconductor Nanophysics, Eindhoven University of Technology, Eindhoven, The Netherlands, *Ordered InAs/InP quantum dot arrays at telecom wavelength.*, promoter prof.dr. P.M. Koenraad and Prof. W.T. Masselink PhD, copromoter Dr. R. Nötzel

Internship project study (August-October, 2009), National Institute for Materials Science, Ibaraki, Japan, supervisor Dr. T. Mano

2004-2006:

MSc. (Materials Physics and Nanotechnology), Linköping University, Linköping, Sweden

MSc. project, *Epitaxial growth of 3C-SiC on hexagonal substrates.*, supervisor Dr. M. Syväjärvi and prof.dr. R. Yakimova

2000-2004:

BSc. (Physics, 2nd class honor), Chulalongkorn University, Bangkok, Thailand